

**A PARAMETRIC ANALYSIS  
OF THE QUASI-STATIC PENETRATION  
OF COMPOSITE MATERIALS**

by

Anthony Francis Manzella

A thesis submitted to the Faculty of the University of Delaware in partial fulfillment of the requirements for the degree of Master of Civil Engineering

Fall 2010

Copyright 2010 Anthony Francis Manzella  
All Rights Reserved

**A PARAMETRIC ANALYSIS  
OF THE QUASI-STATIC PENETRATION  
OF COMPOSITE MATERIALS**

by

Anthony Francis Manzella

Approved: \_\_\_\_\_  
John W. Gillespie Jr., Ph.D.  
Professor in charge of thesis on behalf of the Advisory Committee

Approved: \_\_\_\_\_  
Harry Shenton III, Ph.D.  
Chair of the Department of Civil and Environmental Engineering

Approved: \_\_\_\_\_  
Michael J. Chajes, Ph.D.  
Dean of the College of Engineering

Approved: \_\_\_\_\_  
Charles G. Riordan, Ph.D.  
Vice Provost for Graduate and Professional Education

## ACKNOWLEDGMENTS

Dedicated to my wonderful fiancée, Mandy Romano

*“No road is long with good company”*

I wish to thank Dr. Jack Gillespie, Jr., for providing guidance on the experimentation and analysis and for ensuring that the results were rigorously and methodically verified. The high standard of work you expected will undoubtedly aid me in my future endeavors.

I thank Dr. Bazle Gama for providing his expertise in quasi-static testing and finite element modeling as well as many hours of helpful discussion. I also wish to thank Chris Arvanitelis, who performed the initial experimentation on the thin-sectioned specimens.

I thank all the researchers and lab staff at the Center for Composite Materials who provided invaluable advice on the efficient manufacturing, machining, and testing of specimens. I also thank the great professional staff at CCM for helping with schedules, requisitions, and presentations.

I thank my fellow graduate students, both at CCM and in the Civil Engineering department for their advice and, more importantly, camaraderie.

And lastly I thank my family, which has been supportive throughout the course of my education, and my friends, who have provided a welcome respite from the stresses of research. *S.D.G.*

## TABLE OF CONTENTS

LIST OF TABLES.....	vii
LIST OF FIGURES .....	viii
ABSTRACT .....	xiii
Chapter	
1 INTRODUCTION .....	1
1.1 Background.....	1
1.1.1 Quasi-Static Penetration Method.....	2
1.1.2 Assumptions .....	4
1.2 Goal of Research .....	6
1.3 Review of the Literature .....	8
1.3.1 Studies of Quasi-Static Penetration.....	8
1.3.2 Parametric Studies of Penetration .....	10
1.3.3 Studies of Confined Compression Behavior .....	12
1.4 Outline of Thesis .....	15
2 MATERIALS AND METHODOLOGIES.....	17
2.1 Materials.....	17
2.2 Test Fixtures .....	20
2.3 Experimental Testing.....	24
2.4 Finite Element Model .....	27
2.5 Analytical Model .....	30
2.6 Chapter Summary .....	37
3 EXPERIMENTAL FAILURE BEHAVIOR .....	39
3.1 Failure Mode.....	39
3.1.1 Off-Axis Fracture Angles .....	44

3.1.2	Defining “Thin” and “Thick” Specimens.....	46
3.2	Applied Stress at Failure.....	47
3.3	Stresses on the Fracture Plane.....	54
3.4	Chapter Summary.....	58
4	MINIMUM SPECIMEN WIDTH.....	60
4.1	Background.....	60
4.2	Analytical Calculation.....	61
4.2.1	Effect of Varying Moduli on $L_{crit}$ .....	67
4.2.2	Off-Axis Verification of $L_{crit}$ .....	70
4.3	Numerical Validation.....	71
4.4	Experimental Comparisons.....	79
4.5	Chapter Summary.....	82
5	GEOMETRIC SCALING PARAMETERS.....	84
5.1	Problem Parameters.....	84
5.2	Analytical Form.....	85
5.3	A Geometric Scaling Parameter.....	87
5.4	Numerical Validation.....	88
5.5	Experimental Comparisons.....	90
5.6	Chapter Summary.....	93
6	STRESS STATE AT FAILURE.....	94
6.1	Internal Stress Distribution.....	94
6.1.1	Comments on Fiber Shear Strength.....	103
6.2	Comparison of Failure Criteria.....	107
6.2.1	Maximum Stress Criterion.....	108
6.2.2	Tsai-Hill Criterion.....	110
6.2.3	Tsai-Wu Criterion.....	112
6.2.4	Hydrostatic Crush Criterion.....	113
6.2.5	Maximum Deviator Stress Criterion.....	114
6.3	Mohr-Coulomb Criterion.....	116

6.3.1	Calibrating the Mohr-Coulomb Envelope .....	119
6.4	Point of Failure Initiation .....	124
6.5	Scaling of the Applied Stress at Failure .....	127
6.6	Chapter Summary .....	128
7	CONCLUSIONS .....	130
7.1	Summary.....	130
7.2	Directions for Future Work .....	133
	REFERENCES .....	137

## LIST OF TABLES

Table 2.1 – Material properties for S-2/SC15 composite (from Xiao, Gama, & Gillespie, 2007, p 191) .....	21
Table 3.1 – Experimental test matrix with fracture angle values, $\theta$ (in degrees) .....	42
Table 3.2 – Statistical analysis of fracture angle .....	44
Table 3.3 – Comparison of average fracture angles on different sectioning planes .....	45
Table 3.4 – Experimental test matrix with applied stress values, $\sigma_{app}$ (in MPa) .....	49
Table 4.1 – Correlation of equations (4.3) and (4.4) with data in Figures 4.4-4.7 .....	67
Table 4.2 – Comparison of material properties in the $0^\circ/90^\circ$ and $45^\circ$ orientations.....	71
Table 4.3 – Experimental test matrix with critical width values, $L_{crit}$ (in mm) .....	80
Table 5.1 – Experimental test matrix with geometric ratios of $D_p/H_C$ .....	92
Table 6.1 – Normalized average stresses at punch periphery in the fiber direction.....	101

## LIST OF FIGURES

Figure 1.1 – Representative QS-Envelope (7.62-mm punch, 7.11-mm sample).....	5
Figure 1.2 – Schematics of damage mechanisms under confined compression (from Woodward et al., 1994, p 339).....	13
Figure 2.1 – Schematics of VARTM infusion setup .....	18
Figure 2.2 – Schematic of Punch-Shear test fixture .....	22
Figure 2.3 – Schematic of Mini Punch-Shear test fixture .....	23
Figure 2.4 – Force-displacement corrections (7.62-mm punch, 7.11-mm sample).....	25
Figure 2.5 – Compliance curve for experimental setup.....	25
Figure 2.6 – Typical sectioned specimen (11.09-mm punch, 5.08-mm sample).....	27
Figure 2.7 – Finite element model schematic (12.70-mm punch, 6.99-mm sample) .....	29
Figure 2.8 – Mesh comparison for $\sigma_z$ (6.35-mm punch, 6.99-mm sample).....	29
Figure 2.9 – Mesh comparison for $\tau_{xz}$ (6.35-mm punch, 6.99-mm sample).....	31
Figure 2.10 – Mesh effect on maximum stress (6.35-mm punch, 6.99-mm sample) .....	31
Figure 2.11 – Schematic of assumptions and parameters in analytical model .....	32
Figure 2.12 – Comparison of stress distributions for analytical model and different numerical loading assumptions (12.70-mm punch, 6.99- mm sample) .....	35
Figure 2.13 – Convergence of solution for normal stresses ( $\sigma_z$ ) as a function of number of terms ( $M$ ) for various specimen widths ( $L$ ).....	38
Figure 2.14 – Calibration of relationship between $M$ and $L$ .....	38

Figure 3.1 – Confined compression failure (11.09-mm punch, 5.08-mm sample) .....	40
Figure 3.2 – Measuring fracture angles (11.09-mm punch, 5.08-mm sample) .....	41
Figure 3.3 – Fracture angle as a function of punch diameter .....	43
Figure 3.4 – Fracture angle as a function of specimen thickness .....	43
Figure 3.5 – Comparison of fracture angles on different sectioning planes (10.16-mm punch, 7.11-mm sample) .....	45
Figure 3.6 – Schematic of idealized fracture plug formations.....	46
Figure 3.7 – Force-displacement curve (7.62-mm punch, 7.11-mm sample).....	48
Figure 3.8 – Applied stress at failure as a function of punch diameter .....	50
Figure 3.9 – Applied stress at failure as a function of specimen thickness .....	50
Figure 3.10 – Force reactions on a “column” of material beneath the punch.....	52
Figure 3.11 – Comparison of normal and shear reactions (12.70-mm punch).....	53
Figure 3.12 – Normalized confinement vs. specimen thickness (12.70-mm punch).....	53
Figure 3.13 – Schematic of transformation of stresses into fracture plane.....	55
Figure 3.14 – Comparison of transformed stresses on the fracture plane for a “thin” and a “thick” specimen .....	57
Figure 4.1 – Schematic of definition of critical width, $L_{crit}$ .....	62
Figure 4.2 – Stress distributions for varying thickness (12.70-mm punch).....	63
Figure 4.3 – Stress distributions for varying diameter (12.70-mm sample).....	63
Figure 4.4 – Critical width as a function of thickness (12.70-mm punch).....	64
Figure 4.5 – Critical width as a function of diameter (12.70-mm sample) .....	64
Figure 4.6 – Critical width as a function of thickness (25.40-mm punch).....	65
Figure 4.7 – Critical width as a function of diameter (25.40-mm sample) .....	65

Figure 4.8 – Effect of varying moduli on the stress distribution normal to the support (12.70-mm punch, 12.70-mm sample) .....	69
Figure 4.9 – Off-axis critical width as a function of thickness (12.70-mm punch).....	72
Figure 4.10 – Off-axis critical width as a function of diameter (12.70-mm sample) .....	72
Figure 4.11 – Comparison of numerical stress distribution with analytical value of $L_{crit}$ (12.70-mm punch, 3.81-mm sample).....	74
Figure 4.12 – Comparison of numerical stress distribution with analytical value of $L_{crit}$ (12.70-mm punch, 13.97-mm sample).....	75
Figure 4.13 – Comparison of shear stress at punch periphery for varying widths, $L_C$ (12.70-mm punch, 6.99-mm sample) .....	76
Figure 4.14 – Comparison of normal stress at specimen surface for varying widths, $L_C$ (12.70-mm punch, 6.99-mm sample) .....	77
Figure 4.15 – Comparison of confining stress at punch periphery for varying widths, $L_C$ (12.70-mm punch, 6.99-mm sample) .....	78
Figure 4.16 – Effect of $L < L_{crit}$ on the experimental applied stress at failure.....	81
Figure 5.1 – Parameters in the confined compression problem.....	85
Figure 5.2 – Comparison of shear stress at periphery for $D_p/H_C = 0.909$ .....	89
Figure 5.3 – Comparison of normal stress on surface for $D_p/H_C = 0.909$ .....	89
Figure 5.4 – Comparison of shear stress for $D_p/H_C = 0.909$ with no chamfer .....	91
Figure 5.5 – Comparison of normal stress for $D_p/H_C = 0.909$ with no chamfer .....	91
Figure 6.1 – Comparison of “thin” and “thick” stress distributions.....	95
Figure 6.2 – Transverse stress in the $x$ -direction (12.70-mm punch) .....	97
Figure 6.3 – Transverse stress in the $y$ -direction (12.70-mm punch) .....	97
Figure 6.4 – Through-thickness stress in the $z$ -direction (12.70-mm punch).....	98
Figure 6.5 – Shear stress on the $xy$ -plane (12.70-mm punch) .....	98

Figure 6.6 – Shear stress on the $xz$ -plane (12.70-mm punch).....	99
Figure 6.7 – Shear stress on the $yz$ -plane (12.70-mm punch).....	99
Figure 6.8 – Average stress components $\alpha$ as a function of $D_P$ (6.99-mm sample) .....	102
Figure 6.9 – Average stress components $\alpha$ as a function of $H_C$ (12.70-mm punch).....	102
Figure 6.10 – Experimental values of average shear stress .....	105
Figure 6.11 – Numerical values of concentrated normalized shear stress.....	105
Figure 6.12 – Calculated values of experimental concentrated shear stress.....	106
Figure 6.13 – Maximum stress criterion as a function of $D_P$ (6.99-mm sample).....	109
Figure 6.14 – Maximum stress criterion as a function of $H_C$ (12.70-mm punch) .....	109
Figure 6.15 – Tsai-Hill and Tsai-Wu criteria as function of $D_P$ (6.99-mm sample) .....	111
Figure 6.16 – Tsai-Hill and Tsai-Wu criteria as function of $H_C$ (12.70-mm punch).....	111
Figure 6.17 – Crush and deviator criteria as a function of $D_P$ (6.99-mm sample) .....	115
Figure 6.18 – Crush and deviator criteria as a function of $H_C$ (12.70-mm punch).....	115
Figure 6.19 – Schematic of the development of a Mohr-Coulomb failure envelope.....	118
Figure 6.20 – Transformed shear stress distribution (12.70-mm punch) .....	120
Figure 6.21 – Transformed normal stress distribution (12.70-mm punch).....	120
Figure 6.22 – Calibration of the Mohr-Coulomb envelope .....	121
Figure 6.23 – Mohr-Coulomb criterion as a function of $D_P$ (6.99-mm sample) .....	123
Figure 6.24 – Mohr-Coulomb criterion as a function of $H_C$ (12.70-mm punch).....	123
Figure 6.25 – Damage propagation through a thin specimen (12.70-mm punch, 6.99-mm sample).....	125

Figure 6.26 – Damage propagation through a thick specimen (7.62-mm punch, 6.99-mm sample).....	126
Figure 7.1 – Representative load-displacement curve for a specimen without full support (7.62-mm punch, 7.11-mm sample, 15.24-mm span) .....	135

## **ABSTRACT**

Determining the behavior of composite materials under impact is an important aspect of composite design. Conducting full-scale ballistic tests gives the most realistic insights into impact and penetration behavior, but the expense of these tests makes quasi-static testing and scaled testing attractive alternatives. The present research expands on a previously developed method for determining the penetration behavior of a composite system from quasi-static punch shear testing. While the previous work considered a single punch diameter-composite thickness pair, the present work lays the foundation for using parametric analysis to generalize this methodology for a range of diameters and thicknesses. Experimental results for a variety of punch diameters and composite thicknesses are coupled with analytical solutions and numerical analyses to understand the scaling behavior of the punch-composite system under the specialized case of a confined compression loading. The failure mechanisms and necessary specimen dimensions are explored, leading to the development of scaling factors based on the parameters which define the experimental setup: composite thickness and punch diameter.

# Chapter 1

## INTRODUCTION

### 1.1 Background

Composite materials have seen widespread usage in aerospace and military applications in recent decades. These applications often expose the composite to high speed or “ballistic” impacts by flying debris or projectiles. While composites can be designed to resist high tensile and flexural loadings, they often remain susceptible to these transverse impacts which can create damage in the weaker matrix material. The engineering design and analysis of composites subjected to transverse impacts is further complicated by complex interactions between different damage modes. Composite materials may concurrently exhibit matrix cracking, delaminations, fiber crushing, and fiber tension-shear and compression-shear. In addition, damage from transverse impacts reduces the post-impact tensile and flexural capacity of the composite, making resistance to transverse impact a desirable property.

The complications involved in understanding the ballistic behavior of composites have motivated a large and growing body of research. Researchers have studied experimental methods and results, analytical formulations, and numerical models to enhance design for transverse impact. Abrate (1991, 1994) and Bartus and Vaidya (2007) have presented reviews of hundreds of references related to this field of research.

### 1.1.1 Quasi-Static Penetration Method

The present study builds on a quasi-static penetration model (QS-PM) previously developed by Gama and Gillespie (2008). This model provides an estimate of the ballistic behavior of a composite material from a series of quasi-static (QS) tests. The advantage of such a method is that quasi-static tests can be performed on a standard load frame, while ballistic testing requires high-speed loading capabilities and associated instrumentation. Additionally, quasi-static tests are more amenable to the collection of data such as force-displacement curves, specimen deflections, and the propagation of damage with penetration depth. These data would be difficult to measure during a ballistic test.

The ballistic resistance of a composite is quantified in the QS-PM through the ballistic limit velocity,  $V_{BL}$ . The ballistic limit of a given projectile-target pair is defined as the impact velocity at which the projectile will penetrate the composite with zero residual velocity. Such a parameter is an important measure of ballistic resistance, since any impact velocity less than  $V_{BL}$  would not be expected to cause full penetration of the composite.

The initial impact energy of the projectile at the ballistic limit,  $E_{BL}$ , can be defined as:

$$E_{BL} = \frac{1}{2} m_p V_{BL}^2 \quad (1.1)$$

where  $m_p$  is defined as the projectile mass. Conservation of energy states that at any time  $t$  during the penetration event:

$$E_{BL} = \bar{E}_P + \bar{E}_C + \bar{E}_{E/C} + \bar{E}_D \quad (1.2)$$

where  $E_P$  is the projectile kinetic energy,  $E_C$  is the composite kinetic energy,  $E_{E/C}$  is the elastic strain energy of the deformed composite, and  $E_D$  is the energy dissipated by damage to the composite, all at time  $t$ . For the special case of a projectile impacting at

the ballistic limit, there exists a time  $t$  at which the projectile velocity will be zero and the strain energy of the composite and the energy dissipated through damage will be at a maximum. It can also be assumed that the kinetic energy of the composite will be negligible at this time. Therefore, equation (1.2) simplifies to:

$$E_{BL} = \bar{\epsilon}_{E|C} + \bar{\epsilon}_D \quad (1.3)$$

If the strain energy and energy dissipation capabilities of the composite can be quantified the ballistic limit can be determined using equations (1.1) and (1.3). The purpose of the quasi-static penetration model is to estimate these two energies.

During a ballistic event damage will propagate transversely through the composite away from the projectile. This behavior can be mimicked by performing a series of quasi-static tests for a range of support spans. The energy dissipated to cause damage at a given span can be calculated from the integral of the force-displacement curve at that span. By combining the series of force-displacement curves on a single graph a “Quasi-Static Envelope” (QS-Envelope) can be created. The area under this curve provides an estimate of the energy the composite can dissipate through damage mechanisms.

Two specialized cases of the quasi-static test are also necessary for a proper analysis. First, the elastic strain energy of the composite can be determined by performing a quasi-static test at the support span for the ballistic test in question. By determining the elastic stiffness of the specimen and maximum elastic displacement, the strain energy  $E_{E|C}$  is calculated. Second, the “hydrostatic compressive” or “crush” strength of the composite can be determined from a quasi-static test performed on a fully supported specimen. This test recognizes that at the start of the ballistic event the projectile imparts a stress equal to the peak compressive strength of the composite

until complete destruction is achieved ahead of the projectile. This peak stress is determined from a confined compression test.

A representative QS-Envelope and its constitutive force-displacement curves are shown in Figure 1.1. Further explanation of the development of the QS-PM can be found in the paper by Gama and Gillespie (2008) and in a paper exploring wider application of the QS-PM by Manzella, Gama, and Gillespie (2009).

### **1.1.2 Assumptions**

Some assumptions were made before beginning the present work. These assumptions helped bound the scope of this study and allowed for certain analytical simplifications.

A single composite system (24 oz/yd<sup>2</sup> S-2 glass fabric infused with SC15 epoxy resin) was considered in the study. While a number of individually manufactured panels were required for experimental testing, it was assumed that the constitutive materials for all panels had equivalent mechanical properties: elastic moduli, Poisson ratios, and failure stresses and strains. This assumption was validated by the use of consistent manufacturing techniques and the exclusion of inferior materials (see Chapter 2). Unless otherwise noted, all analytical and numerical models of the experimental testing are assumed to have the same idealized material properties.

Strain-rate and inertial effects were assumed to be negligible. While some rate of displacement or loading is necessary for experimentation, one advantage of quasi-static testing is the use of a loading rate for which these effects are insignificant (ASTM International, 2004).

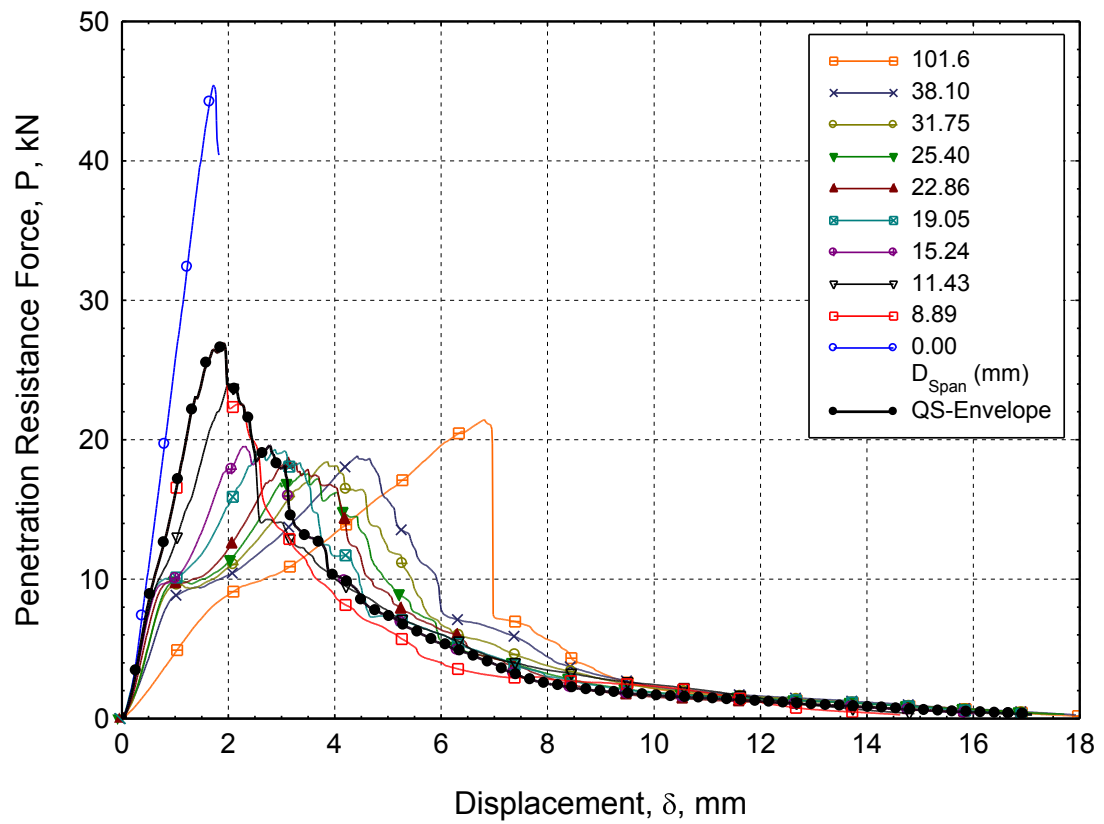


Figure 1.1 – Representative QS-Envelope (7.62-mm punch, 7.11-mm sample)

All test specimens were assumed to be wide enough so that edge effects are negligible. Moving radially away from the point of load application, the transverse confining stresses and through-thickness stresses will decrease. At some critical distance the inclusion of additional material around the edge of the test specimen will no longer contribute to the penetration resistance of the inner material. While testing extremely wide specimens is inefficient, testing specimens with insufficient width may affect the measured material behavior. Analytical expressions for this critical width will be developed in Chapter 4 to verify this assumption.

Finally, it was assumed that the methodology developed by Gama and Gillespie (2008) is valid for all projectile-target pairs. Preliminary research has suggested that the QS-PM is indeed valid for specimen dimensions besides those considered in the original research (Manzella, Gama, & Gillespie, 2009). However, an assessment of the accuracy and precision of the estimation of the ballistic limit is beyond the scope of the present study.

## **1.2 Goal of Research**

While quasi-static testing methodologies are simpler than ballistic methods, a thorough analysis of the impact behavior of a given composite material still requires extensive testing and a significant amount of sample material. Ideally, every possible projectile-target pair, a unique combination of projectile and target geometry and dimensions, must be considered to characterize the composite's behavior fully. However, if geometric or inertial scaling laws can be developed for a composite system, interpolation or limited extrapolation can reduce the number of tests needed to quantify the behavior of that system. Such a scaling law could be developed to predict the ballistic limit velocity output of the QS-PM for a given projectile-target pair from a

known projectile-target pair. However, the basis for this scaling law comes from the successful scaling of the individual force-displacement curves used in the QS-PM.

The goal of the present study is to develop and validate a process for creating geometric scaling laws for these component force-displacement curves. The present parametric analysis is limited to the confined compression case. The confined compression test was chosen as a simpler parametric analysis: only two parameters, specimen thickness and punch diameter, are important to the problem and a lesser degree of interaction between different failure modes is expected. In contrast, specimens tested without full support have three parameters (specimen thickness, support diameter, and punch diameter) and will exhibit some interplay between shear and bending failure modes.

The development of a parametric scaling for the force-displacement curves comes from a theoretical and experimental framework. Theoretical models of the experimental setup identify parameters of interest to the problem and suggest relationships between these parameters. Ideally, the problem parameters can be rearranged in such a way that scaling parameters can be derived. Alternately, if a large matrix of experimental data is obtained, the effects of each parameter can be isolated by fixing one problem parameter while allowing others to vary. The results should suggest relationships between the problem parameters and outputs of interest. Coupling experimental observations with theoretical expectations permits an exploration of the failure modes which dominate specimen behavior. While the formulation of a particular failure criterion should not vary with geometry, different geometries may favor different failure modes. By following the rationale outlined here a logical parametric scaling can be developed.

### **1.3 Review of the Literature**

As mentioned previously, a large body of work exists relating to the penetration of composite materials. Three areas of interest to the present study are considered here: the use of quasi-static methods for materials characterization, parametric studies of the penetration process, and confined compression experimentation.

#### **1.3.1 Studies of Quasi-Static Penetration**

While the present study employs a quasi-static method developed by Gama and Gillespie (2008) as described in Section 1.1.1, quasi-static experimentation has been used by other researchers.

A standardized method of quasi-static indentation of composite materials has been defined by ASTM International (2004). The quasi-static loading of a composite plate by a hemispherical indenter is used to determine the impact resistance of the composite. Two support conditions are defined: a simply-supported condition in which the composite rests on a rigid support with a central circular cavity of diameter 127-mm and a rigidly-backed condition in which the composite rests on a continuous rigid support at least 12.70-mm thick. Damage resistance is quantified by visual inspection, measurement of the resulting “dent depth” after indentation, and measurement of the peak load during testing. The primary application of the standard is to permit comparison of the damage resistance of different materials and provide a baseline damage state for further tolerance testing.

Lee and Sun (1993) developed a method for predicting ballistic behavior from quasi-static results. Ballistic tests were performed on graphite-fiber/epoxy prepreg composite panels of various thicknesses to define the ballistic limit and

determine the damage modes – delamination and shear plugging. These damage modes were observed to be similar to those which occurred under quasi-static loadings. The force-displacement curves obtained from quasi-static testing were correlated with the progression of damage. The static displacement thresholds for the various damage modes were then used to calibrate a finite element model of the ballistic impact. The model was found to give realistic values for the ballistic limit.

Sun and Potti (1996) refined this methodology. Again, quasi-static and ballistic tests were performed on graphite-fiber/epoxy composites for three specimen thicknesses. The same two damage modes were observed. Using a finite element model with Mindlin ring elements and damage softening through reduction in shear modulus, the quasi-static penetration was modeled. The rate of softening was calibrated from the quasi-static force-displacement curves, which were found to collapse to a single curve when normalized by specimen thickness. This quasi-static model was used to calibrate another ballistic model. The displacement failure criterion proposed previously (Lee and Sun, 1993) was found to provide the most accurate results, and was once again used in the finite element model.

In the same paper, the authors also investigated the usage of quasi-static penetration energy to predict ballistic behavior. It was recognized that the integral of the quasi-static force-displacement curve is a measure of the energy dissipated by damage to the composite. However, it was found that using a quasi-static measure of energy over-predicted the residual velocity, while performing the same calculation using a dynamic measurement of energy dissipation provided better results.

Other researchers have used quasi-static testing to characterize composite materials. Caprino et al. (2003) used quasi-static testing of carbon-fiber composites to

find the energy dissipated during penetration and calibrate an expression to predict indentation depth from the energy imparted by the indenter. Baucom and Zikry (2003) used quasi-static tests to examine differences in behavior between different fiber architectures.

### **1.3.2 Parametric Studies of Penetration**

As mentioned in Section 1.2, understanding the effects of the various parameters in a problem can reduce the required experimentation and provide insights into system behavior. Many researchers have performed parametric studies as a way of furthering the understanding of the penetration behavior of composites. A sampling of these studies is provided.

Bless et al. (1989) performed an early exploration into the ballistic behavior of S-2 glass laminates. They found that the ballistic limit tends to scale with the ratio of target thickness to projectile diameter. Noting that the key failure mechanisms appeared to be compressive flow and shear plugging, two expressions for the energy dissipated through each failure mode were developed. The ballistic limit was observed to trend as suggested by the shearing parameter, suggesting that shear-out was the dominant ballistic failure mode.

Swanson (1993) examined the potential for scaling small-scale laboratory penetration tests to full-scale parts. By considering the governing differential equations, it was hypothesized that a linear scaling regime would be appropriate for the measured response. Experimental results from an extensive number of ballistic and quasi-static tests suggested that force, displacement, and time all scaled linearly with an increase in the geometric scale of the test part. However, the scaling of damage, specifically delamination and fiber fracture, was found to be more

complicated. The author suggested that damage scaling may depend on energy-based fracture mechanics and hence depend on impact velocity, not specimen geometry. He concluded that understanding the nature of the failure mechanisms is crucial to developing viable scaling parameters.

Nemes et al. (1998) studied the penetration behavior of carbon-fiber/epoxy composites. A number of parameters were varied: the rate of loading, the thickness of the laminate, the lamina stacking sequence, and the thickness of the sublaminates. By analyzing the effect of each parameter separately, the authors concluded that the load-displacement behavior of the composite is strongly influenced by the rate of loading and thickness of the laminate. However, the loading behavior was similar for different stacking sequences, suggesting that models of the material could safely assume transverse isotropy in most cases.

Gellert et al. (2000) explored the effect of laminate thickness on the ballistic behavior of glass/vinylester composites. By observing the damaged regions in sectioned specimens, they concluded that the ballistic limit and energy dissipated by the composite are bi-linear with thickness. Expressions were derived for the work done by the projectile in the various failure modes, with the expectation that such expressions could be useful for later parametric scalings of ballistic behavior.

Zhou et al. (2001) performed quasi-static tests on carbon fiber/epoxy composites while varying four geometric parameters: indenter diameter, indenter geometry, support span, and support conditions. Certain parameters had more localized effects, influencing only indentation depth, while others had a more global effect, changing the force-displacement response. Four failure modes were observed, but were found to have no correlation with any single geometric parameter. Moreover,

it was seen that the failure modes were an agglomeration of many damage mechanisms. The authors concluded that all four parameters had non-negligible effects when scaling quasi-static behavior.

Naik and Doshi (2008) developed an analytical model to examine the parametric effects on the ballistic behavior of composites. Because of the usage of an analytical model, the parameters could be widely varied for comparison. Specifically, the authors studied the effect of projectile mass and diameter and target thickness on the ballistic response of the target, discussing a number of qualitative conclusions on the effects of these parameters. Naik et al. (2005) also used a similar analytical framework to explore parametric effects on the ballistic penetration of fabrics.

### **1.3.3 Studies of Confined Compression Behavior**

An early study of the failure of composite materials under compressive loadings was performed by Rosen (1965). Rosen hypothesized that the fibers in a unidirectional fiber-matrix composite would buckle under an axial compressive loading in one of two modes. In the first, the fibers buckle out of phase with each other, causing “extension” of the matrix material. In the second, the fibers buckle in phase with each other, causing “shearing” deformations of the matrix material. The “shearing” mode was found to be more prevalent, suggesting that the compressive strength of composite materials is strongly related to the shear strength of the matrix material.

Collings (1974) studied the compressive behavior of unidirectional carbon fiber composites. Initial testing was performed on a cube of material loaded normal to the fiber orientation, with the remaining four sides unconfined. Fracture occurred at a characteristic angle on planes parallel to the fibers. It was observed that fracture did not occur on the plane of maximum shear, suggesting that a compression-shear

interaction was leading to failure. Additional testing was performed on the same materials with additional rigid constraint provided normal to the fiber orientation. When confined in this manner, fracture occurred on planes running through the fibers, increasing the failure strength of the material significantly. It was also noted that the failure strength was similar to that measured from traditional longitudinal compression, suggesting a similar failure mode may occur in both tests.

Woodward et al. (1994) studied the confined compression behavior of four different composite fabric systems: glass-fiber, Kevlar, nylon, and polyethylene. Two different types of damage mechanisms were observed. Glass-fiber and nylon were found to be more “brittle”, fracturing to form a wedge of damaged material at the initial load drop. With continued loading, this wedge was crushed and extruded the material ahead of it. Kevlar and polyethylene were observed to be more “ductile”, with the fibers being strained until catastrophic tensile failure. Elastic rebound occurred, leading to continued fracturing. These damage mechanisms are shown schematically in Figure 1.2. Under higher strain rates, all materials behaved in a ductile manner except for glass-fiber, which crushed the fibers ahead of the projectile.

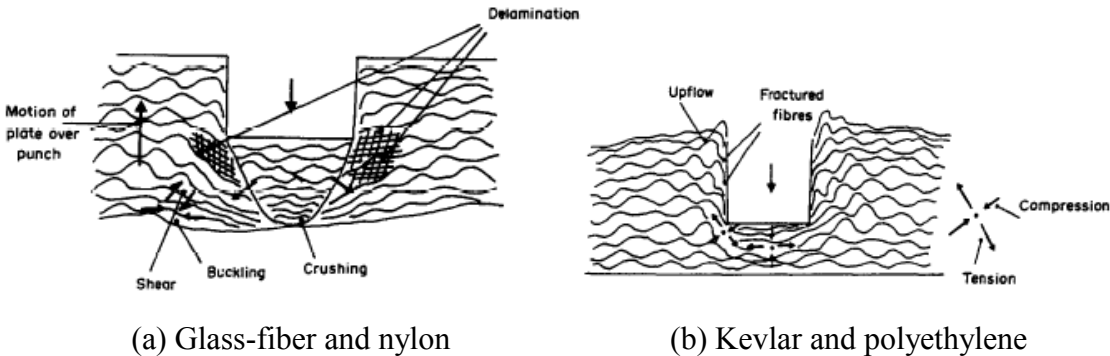


**Figure 1.2 – Schematics of damage mechanisms under confined compression (from Woodward et al., 1994, p 339)**

Oguni et al. (2000) performed unconfined and confined compression tests on unidirectional fiberglass/vinylester composites with loading parallel to the fiber direction. Confinement was provided by placing the composite specimen within a tight-fitting metal ring, giving a proportional confinement of  $\sigma_{conf}/\sigma_{app} \approx 0.3$ . Both the unconfined and confined specimens exhibited similar stiffness and peak load up to first damage. The unconfined specimen was observed to fail catastrophically at the peak load due to shear failure of the matrix material by fracturing parallel to the fibers. However, the confined specimen exhibited progressive failure due to fiber kinking without a complete loss of load.

Yen et al. (2004) studied the shear failure of fibers due to transverse loadings. A Mohr-Coulomb criterion was proposed to describe the shear failure of the fibers. The fiber shear strength and friction coefficient for S-2 glass/SC15 composites were determined using a fixture similar to that developed by Collings (1974). Fracture was observed to occur through the fibers at a characteristic angle. The material model was used to predict the quasi-static punch shear failure of the S-2 glass/SC15 composite in the finite element code LS-DYNA.

Potter et al. (2005) carried out biaxial compression tests on  $[\pm 45]_{12s}$  and  $[\pm 30]_{12s}$  graphite/epoxy composite specimens. Biaxial compression was provided in the fiber directions by two sets of loading crossheads, perpendicular to each other and programmed to provide a pre-determined level of proportional confinement. Increasing the level of confinement tended to increase delaminations and through-thickness inter-ply shear cracks while curtailing the growth of transverse shear cracks in the fiber orientations. However, transverse shear cracking was still observed in all specimens through both the matrix and fibers, depending on fiber orientation.

Classical laminate theory was applied to the experimental results to estimate the stresses within each lamina. It was found that for specimens where shear cracking was primarily in the matrix material a Mohr-Coulomb type interaction occurred for the shear and hydrostatic stresses at the matrix level, though no such interaction existed for stresses in the fibers for these specimens. However, for specimens that exhibited predominantly fiber shearing a Mohr-Coulomb type interaction occurred for the fiber stresses. Moreover, it was observed that the global shear and normal stress data could be described by a Mohr-Coulomb interaction, regardless of the type of fracture.

#### **1.4 Outline of Thesis**

In Chapter 2 the materials and methodologies employed in the present study are described. The manufacturing process used to make the composite panels is outlined. Experimental fixtures, testing methods, and data reduction strategies are explained. Numerical and analytical models of the confined compression problem are also introduced.

In Chapter 3 the failure behavior of the confined compression specimens is discussed. Visual observation of experimental specimens suggests that specimens fail along a characteristic fracture plane. The depth of fracturing suggests that two different damage regimes may exist in confined compression testing. The applied stress to initiate failure is seen to have a characteristic value regardless of geometry although the nature of the internal force reactions is sensitive to geometry. Stress transformations show that a compression-shear interaction occurs on this fracture plane, which may explain the behavior.

In Chapter 4 the constraints on the specimen dimensions are explored. The need for a minimum specimen width to ensure consistent results is discussed. The

analytical model is used to derive empirical expressions for this minimum specimen width. The expressions are validated with the numerical model in the fiber orientation and an off-axis orientation.

In Chapter 5 the key parameters defining the confined compression problem are presented, as well as the equations for the analytical form of the problem. Examination of the analytical form suggests linear scaling exists between the stress applied to the punch and the internal stress distributions. In addition, a geometric similarity parameter is derived and validated with the numerical model.

In Chapter 6 the scaling of the applied stress at first failure is studied. The numerical model is used to demonstrate changing stress behavior with geometry, in contradiction to the experimental observation. Common failure criteria are explored to find the stress interactions which reconcile the numerical stress distribution and experimental results. Deficiencies in the failure criteria suggest that a compressive stress interaction such as in the Mohr-Coulomb criterion can match the fracture mode and experimental results. The successful calibration of this criterion is used to predict the initiation and propagation of damage.

In Chapter 7 the results of the present study are summarized and overall conclusions about the parametric scaling of confined compression testing are drawn. The application of the current methodology to the parametric scaling of tests on specimens without a full support is discussed as a direction for future research.

## Chapter 2

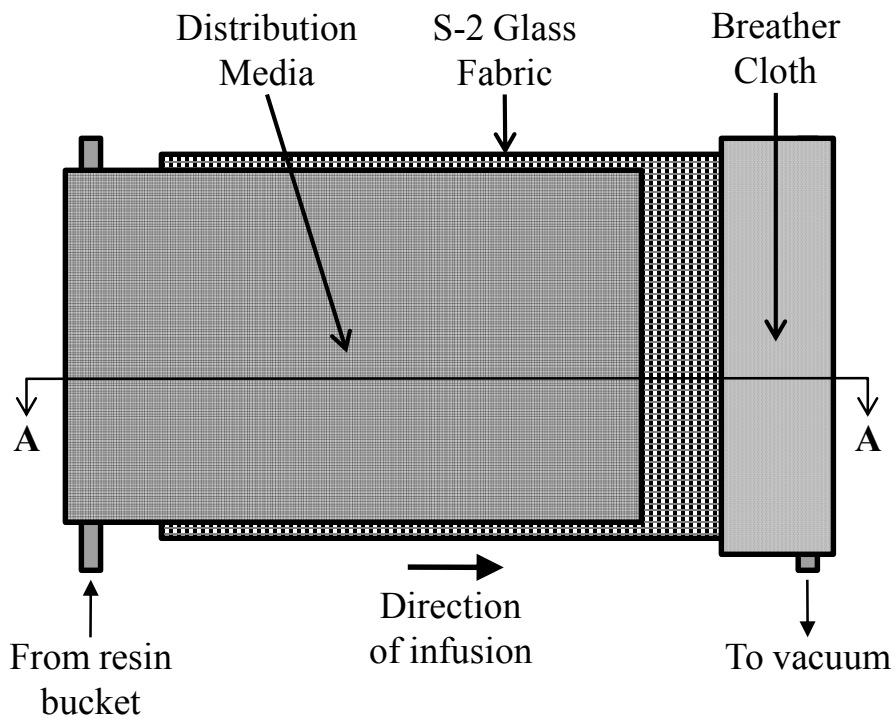
### MATERIALS AND METHODOLOGIES

#### 2.1 Materials

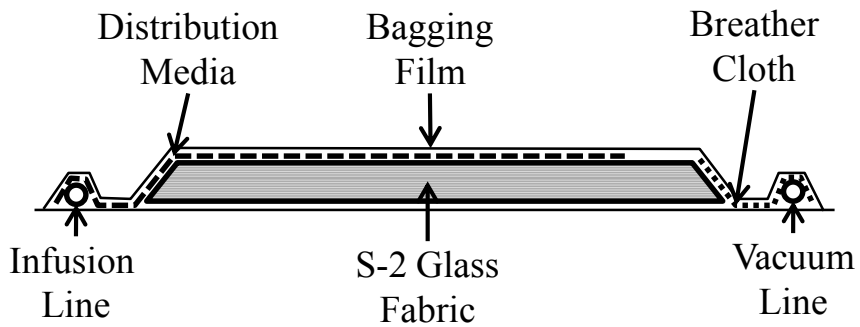
All experimental tests were performed on a composite layup of plain-weave 24oz/yd (814 g/m<sup>2</sup>) S-2 glass infused with Applied Poleramic's SC15 epoxy resin. The infusion was performed using the Vacuum Assisted Resin Transfer Molding (VARTM) process. Maintaining quality during the manufacturing process was necessary to justify the assumption of uniform material properties among experimental tests and between numerical, analytical, and experimental results.

Fabric was cut from rolls into plies of a desired size, normally a few inches larger than needed for cutting specimens to account for edge fraying. Any loose fabric tows were discarded and the plies were weighed. The fabric was then laid on a steel manufacturing table coated with removal agent, covered with one to two layers distribution media depending on panel thickness, and bagged. An infusion line and vacuum line were placed on opposite sides of the fabric with spiral tubing on the ends. Breather cloth was also added around the vacuum line. A schematic of the VARTM setup used is shown in Figure 2.1. Once properly bagged, vacuum was pulled on the panel and the infusion line was clamped. The bag was checked for leaks until a leakage rate of less than 0.1 in/Hg/min (2.54-mm/Hg/min) was achieved.

Based on the weight of fabric in the panel, the two parts of the SC15 epoxy were measured, assuming a conservative fiber volume fraction (FVF) of 45%



**a) Plan view of VARTM infusion setup**



**b) Section A-A view of VARTM infusion setup**

**Figure 2.1 – Schematics of VARTM infusion setup**

with an additional 1000g as a safety factor. The epoxy was thoroughly mixed and degassed. The infusion line was placed in the resin bucket and unclamped, beginning the infusion process. The infusion flow and remaining resin levels were monitored throughout the infusion process to ensure no air entered the part and flow remained uniform both across the plies and through the thickness. If necessary, a smaller bypass tube was placed on the vacuum line for larger panels to reduce the flow rate and to allow the resin to permeate the fabric. Once the fabric was completely infused, the infusion line was clamped and the part cured at ambient temperature under vacuum for at least 36 hours.

Following curing, the panel was removed from the table and post-cured in an oven at ambient pressure for 4 hours at 200° F (93° C). An hour ramp-up from room temperature and an hour ramp-down to room temperature were used. The panel was removed from the oven and weighed to determine the final panel weight and FVF. All manufactured panels had a FVF of approximately 51%. Panels were also visually inspected for voids. A void content of approximately 0.5% or less was measured using the applicable ASTM standard (ASTM International, 2003), suggesting good quality in the manufactured panels.

Fully cured panels were then sectioned into specimens of the desired size. Square specimens from thicker panels were sectioned using a diamond coated wet-saw. Circular specimens from thinner panels were sectioned using a diamond-coated core drill and surface-ground to the desired thickness. Following sectioning, specimens were again checked for voids.

Material properties for the fully cured composite are listed in Table 2.1. Properties are listed with respect to the material axes. The  $x$ -axis is oriented in the principal fiber direction, the  $y$ -axis is oriented in the secondary fiber direction, and the  $z$ -axis is oriented in the through-thickness. For plain-weave S-2 glass it is assumed that the properties in the  $x$ - and  $y$ -directions are interchangeable.

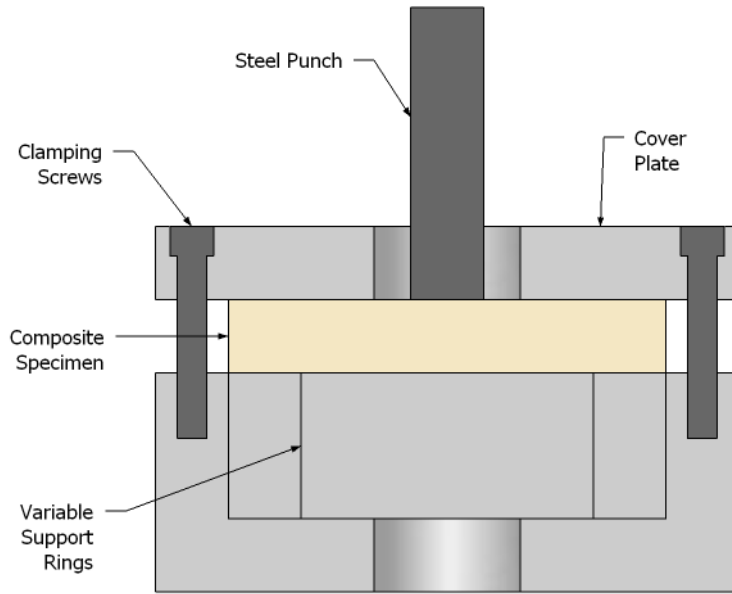
## 2.2 Test Fixtures

Two custom fixtures were used to perform the confined compression tests. Illustrations and photographs of both fixtures are presented in Figures 2.2 and 2.3. They employ the same basic design and are made from high-grade tool steel.

The punch shear test fixture (Figure 2.2) had a steel square base plate with dimensions of length $\times$ width $\times$ height of 4.0'' $\times$ 4.0'' $\times$ 1.5'' (101.6-mm $\times$ 101.6-mm $\times$ 38.1-mm). A central cavity 3.0'' (76.2-mm) in diameter and 1.0'' (25.4-mm) deep was cut into the base. Steel rings of varying diameter and a height of 1.0'' (25.4-mm) could be fit within this cavity to change the support span of the test specimen. For the experiments in the present work a full complement of rings was used such that the specimen was completely supported by a flush surface. After the specimen was centered on the base plate a steel cover plate with dimensions of 4.0'' $\times$ 4.0'' $\times$ 0.5'' (101.6-mm $\times$ 101.6-mm $\times$ 12.7-mm) was placed on top. The cover plate had a central hole with a diameter of 1.0'' (25.4-mm) to permit free movement of the punch. A square specimen 3.0'' (76.2-mm) in width was clamped in the fixture by at least 4 bolts between the cover and base plates. The bolts were hand-tightened to provide a clamping force on the specimen. It was assumed that this force provided vertical confinement and prevented excessive lateral movement of the specimen.

**Table 2.1 – Material properties for S-2/SC15 composite (from Xiao, Gama, & Gillespie, 2007, p 191)**

<b>Elastic Moduli</b>			<b>Shear Moduli</b>			<b>Poisson Ratios</b>			
$E_x$	$E_y$	$E_z$	$G_{xy}$	$G_{xz}$	$G_{yz}$	$\nu_{xy}$	$\nu_{xz}$	$\nu_{yz}$	
<i>GPa</i>	<i>GPa</i>	<i>GPa</i>	<i>GPa</i>	<i>GPa</i>	<i>GPa</i>	---	---	---	
27.5	27.5	11.8	2.90	2.14	2.14	0.11	0.18	0.18	
<b>Normal Failure Strengths<sup>1</sup></b>						<b>Shear Failure Strengths<sup>2</sup></b>			
$S_x$ (T)	$S_x$ (C)	$S_y$ (T)	$S_y$ (C)	$S_z$ (T)	$S_z$ (C)	$T_F$	$T_{xy-M}$	$T_{xz-M}$	$T_{yz-M}$
<i>MPa</i>	<i>MPa</i>	<i>MPa</i>	<i>MPa</i>	<i>MPa</i>	<i>MPa</i>	<i>MPa</i>	<i>MPa</i>	<i>MPa</i>	<i>MPa</i>
604	291	604	291	75	480 <sup>3</sup>	250	75	58	58
<sup>1</sup> – T = tensile failure, C = compressive failure <sup>2</sup> – F = fiber mode, M = matrix mode <sup>3</sup> – Unconfined compressive strength									

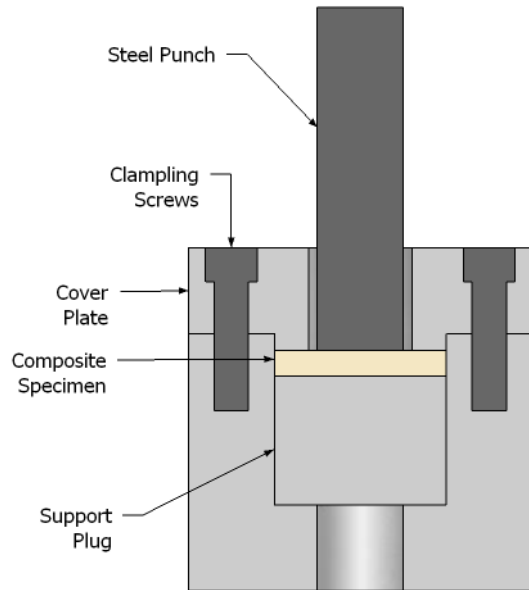


**a) Schematic of fixture**



**b) Fixture in machine**

**Figure 2.2 – Schematic of Punch-Shear test fixture**



**a) Schematic of fixture**



**b) Fixture in machine**

**Figure 2.3 – Schematic of Mini Punch-Shear test fixture**

The mini punch-shear test fixture (Figure 2.3) had a cylindrical steel base component 2.0” (50.8-mm) in diameter with a central cavity 1.0” (25.9-mm) in diameter and 1.0” (25.4-mm) deep. The central cavity provides a clearance of 0.010” (0.254-mm) around the edge of the specimen, which was circular with a diameter of 1.0” (25.4-mm). A steel support cylinder was placed in this cavity followed by the specimen, such that the specimen was almost flush with the top of the base component. A cover plate 2.0” (50.8-mm) in diameter and 0.5” (12.7-mm) thick, with a slight indentation in the central cavity, was placed on top of the specimen. As with the punch shear fixture, 8 bolts were hand-tightened to provide vertical confinement. Lateral confinement was provided by the fixture. A hole in the center of the cover plate allowed passage of the punch with a clearance of 0.010” (0.254-mm).

Punches were solid cylinders with a flat head. A chamfer of 0.01" (0.254-mm) existed around the perimeter of the punch head to prevent shear stress concentrations at the periphery. Punches were made of high-strength heat-treated maraging steel to prevent yielding or buckling in the punch. Punches for the punch-shear fixture were directly threaded into the loading machines, while punches for the mini punch-shear fixture were driven by a larger punch.

### **2.3 Experimental Testing**

All tests were performed on a screw-driven Instron 4484 load-frame under displacement control. The load-cell was rated for 33,720-lbf (150-kN), with the limiting load set to 28,000-lbf (124.5-kN). A driving rate of 0.05-in/min (1.27-mm/min) was used for tests with the punch-shear fixture, while a rate of 0.02-in/min (0.508-mm/min) was used for tests with the mini punch-shear fixture. Data were recorded using Instron's Bluehill 2 software at a rate of 2-Hz for tests with the punch-shear fixture and 10-Hz for tests with the mini punch-shear fixture. The machine load-head was carefully lowered until contact between the punch and specimen was achieved and then raised to the point of zero applied load. The estimated pre-load was less than 0.5% of the load at elastic yield. Load was applied until the elastic limit was reached, as characterized by a load drop (see Figure 2.4). Once the load drop was reached, the test was stopped, the load head was brought back, and the fixture and specimen were removed. The specimen was bagged for later sectioning and the recorded time, displacement, and load data were written to a Microsoft Excel file for further analysis. A representative force-displacement curve is shown in Figure 2.4 (blue curve). Data were converted from the English units used by the Instron Bluehill software to SI units.

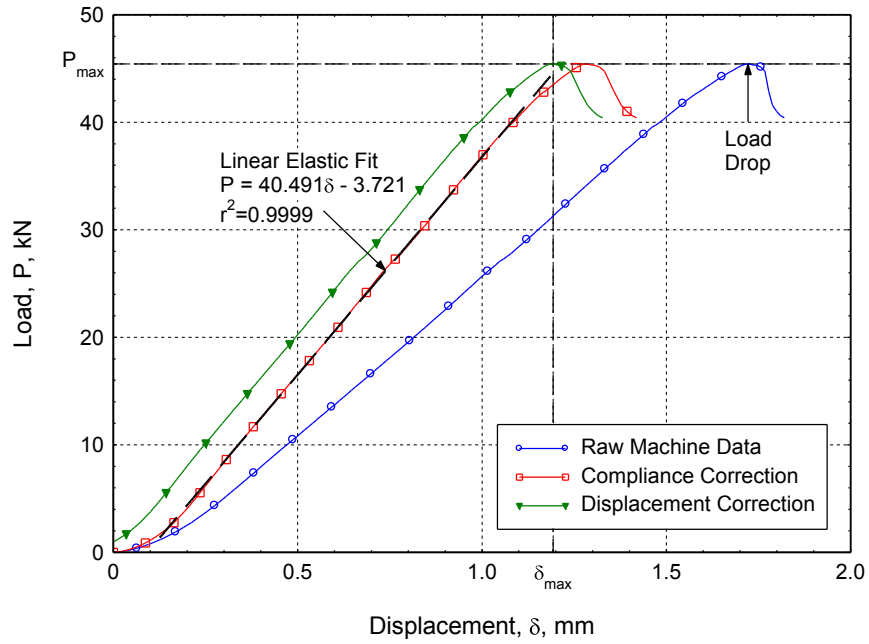


Figure 2.4 – Force-displacement corrections (7.62-mm punch, 7.11-mm sample)

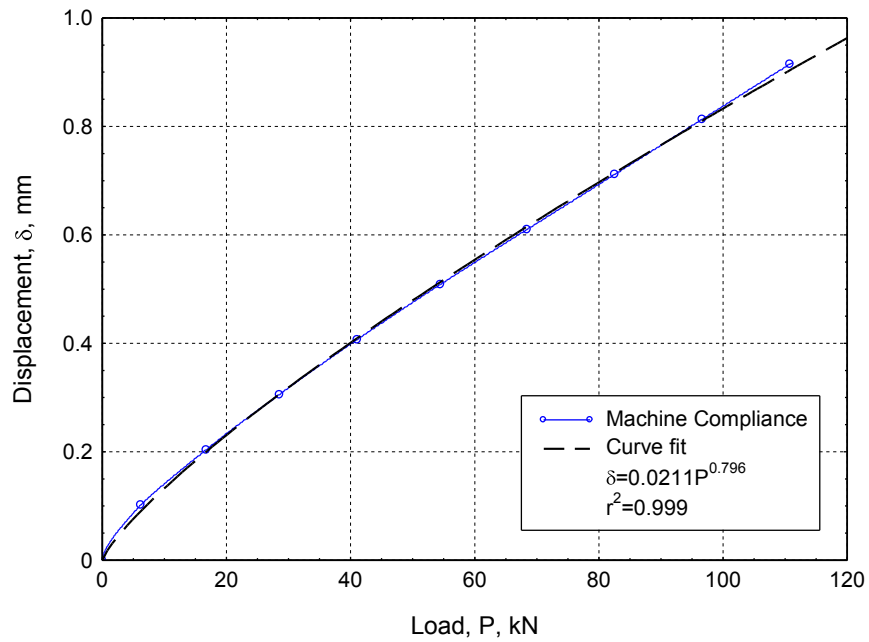


Figure 2.5 – Compliance curve for experimental setup

Two corrections were made to the force-displacement data. The compliance  $C$  of the machine and fixture was measured and fitted with a curve of the form  $C = aP^b$ , where  $P$  is the load and  $a$  and  $b$  are fitting parameters. The compliance data are shown in Figure 2.5. The compliance was removed by plotting  $P(\delta_1)$ , where  $\delta_1 = \delta - C$  (red curve in Figure 2.4). It was also recognized that a non-linear loading region occurs due to the initial settling of the fixture. Assuming the curve should exhibit linear elastic behavior until first failure, a curve of the form  $P = c\delta_1 + d$ , where  $P$  is the load,  $\delta_1$  is the compliance-corrected displacement, and  $c$  and  $d$  are fitting parameters, was fit to the linear-elastic portion of the curve. The settling effect was removed by plotting  $P(\delta_2)$ , where  $\delta_2 = \delta_1 + d/c$  (green curve in Figure 2.4). By correcting curves in this way, the displacements at peak load could be more accurately compared without the effects of compliance or different initial loading regimes. It is noted that the corrections affect the measurement of displacement, stiffness, and energy dissipation but have no influence on the measured loads.

Following data correction, the peak load at the load drop (see Figure 2.4) was recorded. The load drop is taken to represent the initiation of failure in the specimen. Since the measured parameter of interest is the applied stress at failure initiation, this peak load was divided by the area of the punch to determine the applied stress. Experimental applied stress results will be presented in Chapter 3.

Damage within the composite specimens was observed by sectioning the specimens. Specimens were sectioned using a guided diamond-coated wet saw to assure a clean and straight cut. All specimens were sectioned along the fiber direction ( $0^\circ/90^\circ$  orientation) with select specimens additionally sectioned in the  $45^\circ$  orientation for damage comparison around the punch periphery. The specimens' sectioned plane

was dipped in a solution of either blue ink and ethyl alcohol or red dye penetrant and acetone. Excess dye on the sectioned plane was removed by wiping with a paper towel soaked in acetone. Specimens were allowed to air dry, then digitally photographed for further analysis. A typical specimen section is shown in Figure 2.6.



**Figure 2.6 – Typical sectioned specimen (11.09-mm punch, 5.08-mm sample)**

## **2.4 Finite Element Model**

Experimental observations do not permit an analysis of the stresses within the specimen during testing. To explore the distribution of stresses leading to failure in the specimens, a finite element (FE) model was developed using Dassault Systemes' CATIA software (CATIA v5 R19). A quarter-symmetric model was created with appropriate boundary conditions to reduce the required computational resources.

The composite specimen was modeled as a 3-D anisotropic material on a frictionless rigid foundation. Use of a 3-D anisotropic material allowed for input of all the properties presented in Table 2.1 without any simplifying material assumptions.

The punch was modeled as a quarter-cylinder of elastic steel (elastic modulus =  $E = 200$  GPa; Poisson's ratio =  $\nu = 0.29$ ; density =  $\rho = 7850$  kg/m<sup>3</sup>). A chamfer of 0.01" (0.254-mm) was included to match the punches used in testing. The punch was given a height of 12.70-mm (0.50-in) to provide sufficient distance for stress redistribution within the punch. The cover plate was neglected in modeling based on an assumption that any uplift at the specimen edges is negligible.

A uniform stress of 100,000 Pa (14.5 psi) was applied to the top of the punch in all models. The boundary conditions on the punch ensured that translation occurred only along the vertical axis. A surface-to-surface contact was defined between the punch and specimen with a friction coefficient of  $\mu = 0.20$ . Elastic deformation was modeled using the Elfini linear-elastic static analyzer native to CATIA. Since the confined compression experiments performed only considered material behavior up to first failure, a linear elastic solver was found to be sufficient for analysis.

The model was meshed using linear 3-D hexahedral (six-sided) elements, with a refined mesh near the punch contact and a coarser mesh at the specimen edges. A baseline mesh of two through-thickness elements per ply, where  $H_{ply} = 0.635$ -mm, was considered. The size of the FE models ranged from 50,000 elements to 183,000 elements. Visualizations of the model and meshing are presented in Figure 2.7. It was observed that oscillations in the stress normal to the specimen surface existed for most specimens at the baseline level of refinement (see Figure 2.8). The mesh was further refined until a smooth stress distribution was achieved on the specimen surface. This refinement is shown in Figure 2.8, where a mesh of 1.5 to 2.0 times the baseline mesh is seen to be sufficient. Stress concentrations are also noted at the punch periphery on

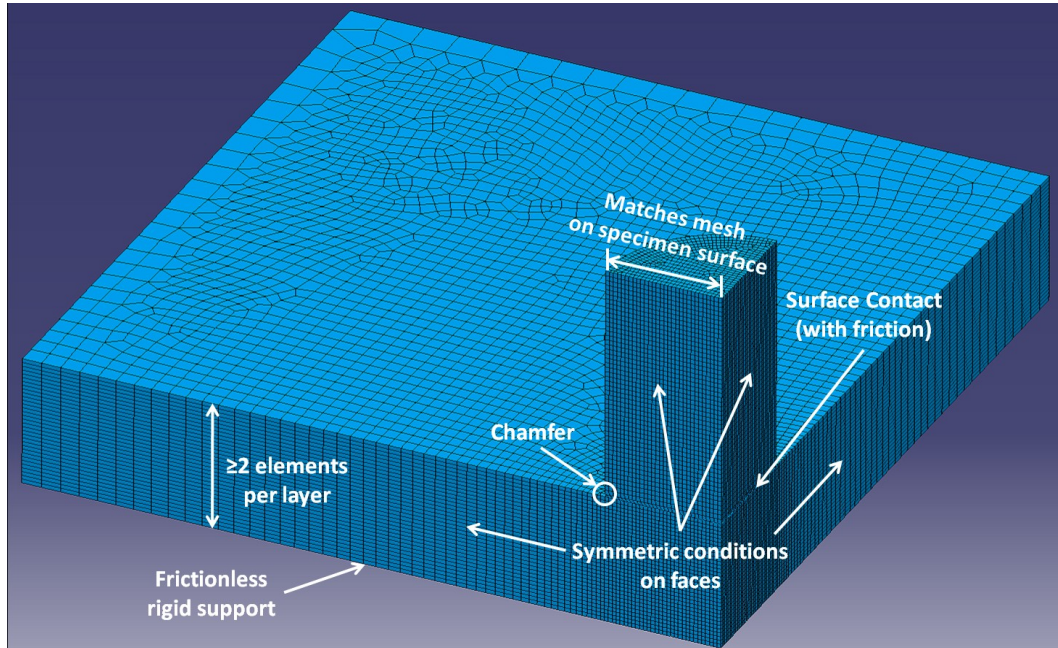


Figure 2.7 – Finite element model schematic (12.70-mm punch, 6.99-mm sample)

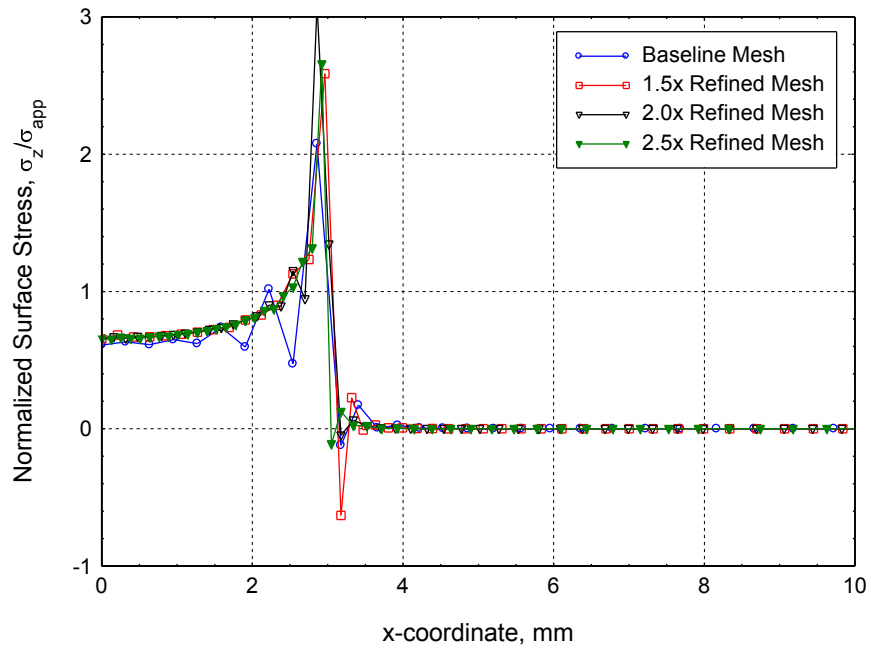


Figure 2.8 – Mesh comparison for  $\sigma_z$  (6.35-mm punch, 6.99-mm sample)

the surface of the specimen. In a linear elastic model, these stress concentrations will approach a stress singularity with continued refinement. Since linear elements were used, maximum stress values only occurred at the nodes, resulting in a more pronounced stress concentration for more refined meshes. However, it was noted that the maximum stress values in Figure 2.8 are also dependent on the nodal locations, which vary for different mesh refinements.

The effect of the mesh refinement on the through-thickness shear stress distribution at the punch periphery is shown in Figure 2.9. Again, sensitivity to the mesh refinement and nodal locations is noted. The averaging of stresses at the initiation of fracture over the ply thickness will be discussed in Chapter 6 as a solution to mesh sensitivity. The effect of mesh refinement on averaged values of the six stress components is shown in Figure 2.10. It is seen that refinement is achieved for meshes with a density greater than 1.5 times the baseline mesh, as observed in Figure 2.8.

CATIA permitted visualization of all stress components and principal stresses. When a more detailed analysis was required, results for a particular face were output to Microsoft Excel for further study. These stress results will be presented in Chapter 6.

## **2.5 Analytical Model**

Analytical models of a physical problem are useful for parametric analysis. Referencing a valid model allows for easy identification of those parameters which affect a problem and suggests relationships between those parameters. An analytical model also provides a theoretically sound comparison for experimental and numerical results.

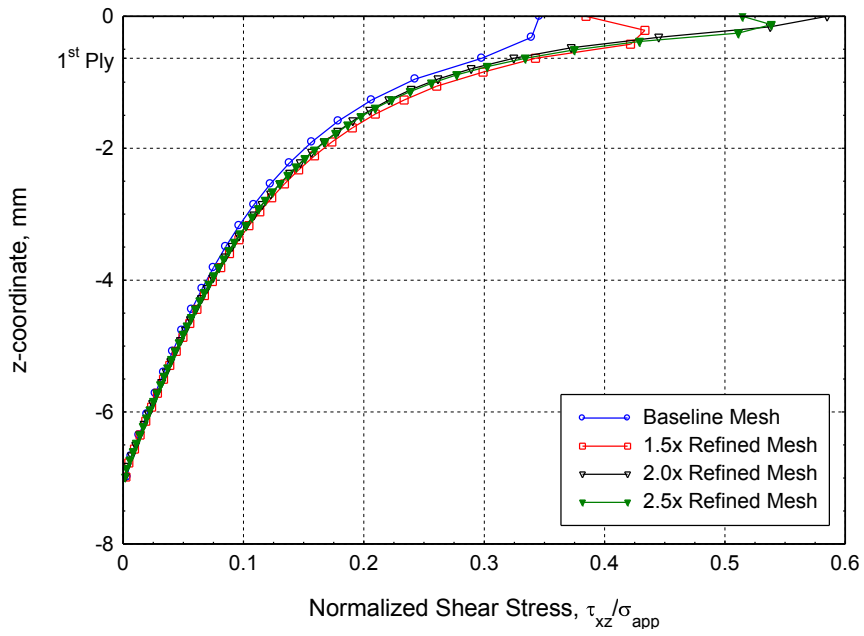


Figure 2.9 – Mesh comparison for  $\tau_{xz}$  (6.35-mm punch, 6.99-mm sample)

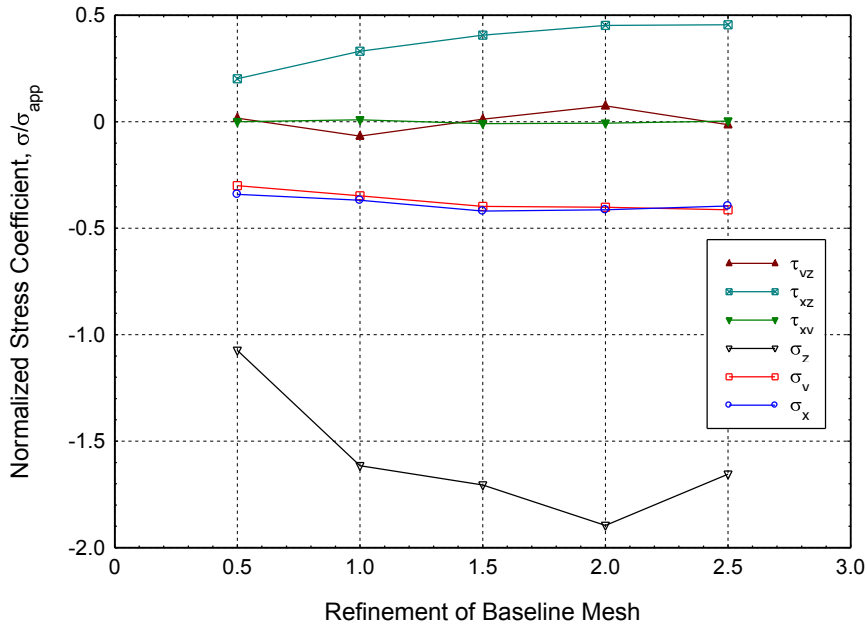
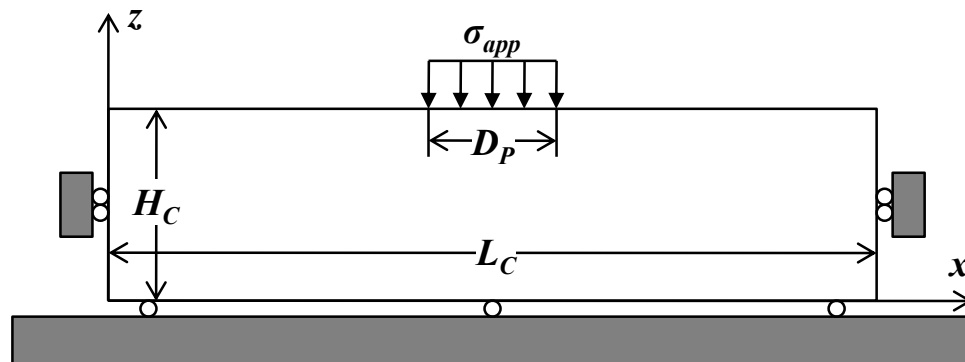


Figure 2.10 – Mesh effect on maximum stress (6.35-mm punch, 6.99-mm sample)

The current work uses an analytical model presented by Milovic (1992, pp 182-189). This model makes a number of simplifying assumptions when compared with the experimental setup. The specimen is assumed to be infinite in extent in the  $y$ -direction (longitudinal) with an infinite strip stress loading applied in the  $z$ -direction over a contact area  $D_p$ . This configuration allows for a 2-D plane strain approximation of stresses in the specimen. The specimen is treated as an anisotropic material. The contact with the support is treated as rigid and frictionless, while the specimen edges are constrained in the  $x$ -direction (transverse). A schematic of the analytical model is shown in Figure 2.11.



**Figure 2.11 – Schematic of assumptions and parameters in analytical model**

The problem solution is framed by two partial differential equations:

$$A_{11} \frac{\partial u}{\partial x^2} + A_{55} \frac{\partial u}{\partial z^2} + (A_{13} + A_{55}) \frac{\partial w}{\partial x \partial z} = 0 \quad (2.1)$$

$$A_{55} \frac{\partial w}{\partial x^2} + A_{33} \frac{\partial w}{\partial z^2} + (A_{13} + A_{55}) \frac{\partial u}{\partial x \partial z} = 0 \quad (2.2)$$

where  $u$  and  $w$  are the displacements in the  $x$  and  $z$ -directions, respectively, and the coefficients  $A$  are given by:

$$A_{11} = \frac{E_x \left(1 - \nu_{xz} \frac{E_x}{E_z}\right)}{(1 + \nu_{xz}) \left(1 - \nu_{xz} - 2\nu_{xz} \frac{E_x}{E_z}\right)} \quad (2.3)$$

$$A_{13} = \frac{E_x \nu_{xz}}{\left(1 - \nu_{xz} - 2\nu_{xz} \frac{E_x}{E_z}\right)} \quad (2.4)$$

$$A_{33} = \frac{E_z (1 - \nu_{xz})}{\left(1 - \nu_{xz} - \nu_{xz} \frac{E_x}{E_z}\right)} \quad (2.5)$$

$$A_{55} = \bar{J}_{xz} \quad (2.6)$$

The necessary material properties for S-2/SC15 composite were given in Table 2.1.

By solving for the displacements  $u$  and  $w$  using trigonometric series, the equations for the three stress components can be found:

$$\sigma_x = \frac{\sigma_{xp} D}{L} + \sigma_{xp} \sum_{m=1}^M \frac{\sin \frac{m\pi}{2L} \left[ 6.05 \times 10^8 \sinh\left(\frac{0.47m\pi}{L}\right) \cosh\left(\frac{3.32m\pi}{L}\right) - 5.74 \times 10^9 \sinh\left(\frac{3.32m\pi}{L}\right) \cosh\left(\frac{0.47m\pi}{L}\right) \right] \cos \frac{m\pi}{L}}{m\pi \left[ 1.51 \times 10^8 \sinh\left(\frac{0.47m\pi}{L}\right) \cosh\left(\frac{3.32m\pi}{L}\right) - 1.44 \times 10^9 \sinh\left(\frac{3.32m\pi}{L}\right) \cosh\left(\frac{0.47m\pi}{L}\right) \right]} \quad (2.7)$$

$$\sigma = \frac{0.52\sigma_{,p}D}{L} + \sigma_{,p} \sum_{m=1}^M \frac{\sin \frac{m\pi}{2L} \left[ 9.05 \times 10^9 \sinh\left(\frac{0.47m\pi}{L}\right) \cosh\left(\frac{3.32m\pi}{L}\right) - 1.02 \times 10^9 \sinh\left(\frac{3.32m\pi}{L}\right) \cosh\left(\frac{0.47m\pi}{L}\right) \right] \cos \frac{m\pi}{L}}{m\pi \left[ 1.51 \times 10^8 \sinh\left(\frac{0.47m\pi}{L}\right) \cosh\left(\frac{3.32m\pi}{L}\right) - 1.44 \times 10^9 \sinh\left(\frac{3.32m\pi}{L}\right) \cosh\left(\frac{0.47m\pi}{L}\right) \right]} \quad (2.8)$$

$$\tau_z = -\sigma_{,p} \sum_{m=1}^M \frac{1.25 \sin \frac{m\pi}{2L} \left[ 2.40 \times 10^9 \sinh\left(\frac{0.47m\pi}{L}\right) \cosh\left(\frac{3.32m\pi}{L}\right) - 2.40 \times 10^9 \sinh\left(\frac{3.32m\pi}{L}\right) \cosh\left(\frac{0.47m\pi}{L}\right) \right] \cos \frac{m\pi}{L}}{m\pi \left[ 1.51 \times 10^8 \sinh\left(\frac{0.47m\pi}{L}\right) \cosh\left(\frac{3.32m\pi}{L}\right) - 1.44 \times 10^9 \sinh\left(\frac{3.32m\pi}{L}\right) \cosh\left(\frac{0.47m\pi}{L}\right) \right]} \quad (2.9)$$

Further details on the derivation of equations (2.7-2.9) can be found in Milovic's text (1992, pp 182-189). It should be noted that the constants shown in equations (2.7-2.9) reflect the material properties of the S-2 glass/SC15 epoxy composite. The complexity of the solution required the inputting of material properties in equations (2.3-2.6) rather than maintaining the variable form. A similar solution for a circular load on an elastic layer was given by D.M. Wood (1984) using Bessel functions. However, a series solution was found to be more amenable for computational calculations.

The assumption of plane strain used above is not true for the experimental and numerical cases, where the applied load is axisymmetric. Additionally, an elastic punch will not apply a uniform stress to the specimen, but will have a non-uniform distribution with stress concentrations around the punch periphery. Figure 2.12 shows a comparison of the stress distributions arising from the analytical model and a plane strain loading, a circular region of uniform stress, and an elastic punch loading modeled using the CATIA/Elfini software. It was seen that the numerical prediction of the analytical model shows an acceptable level of agreement. It was also noted that the plane strain and axisymmetric loadings exhibit similar behavior, suggesting that a

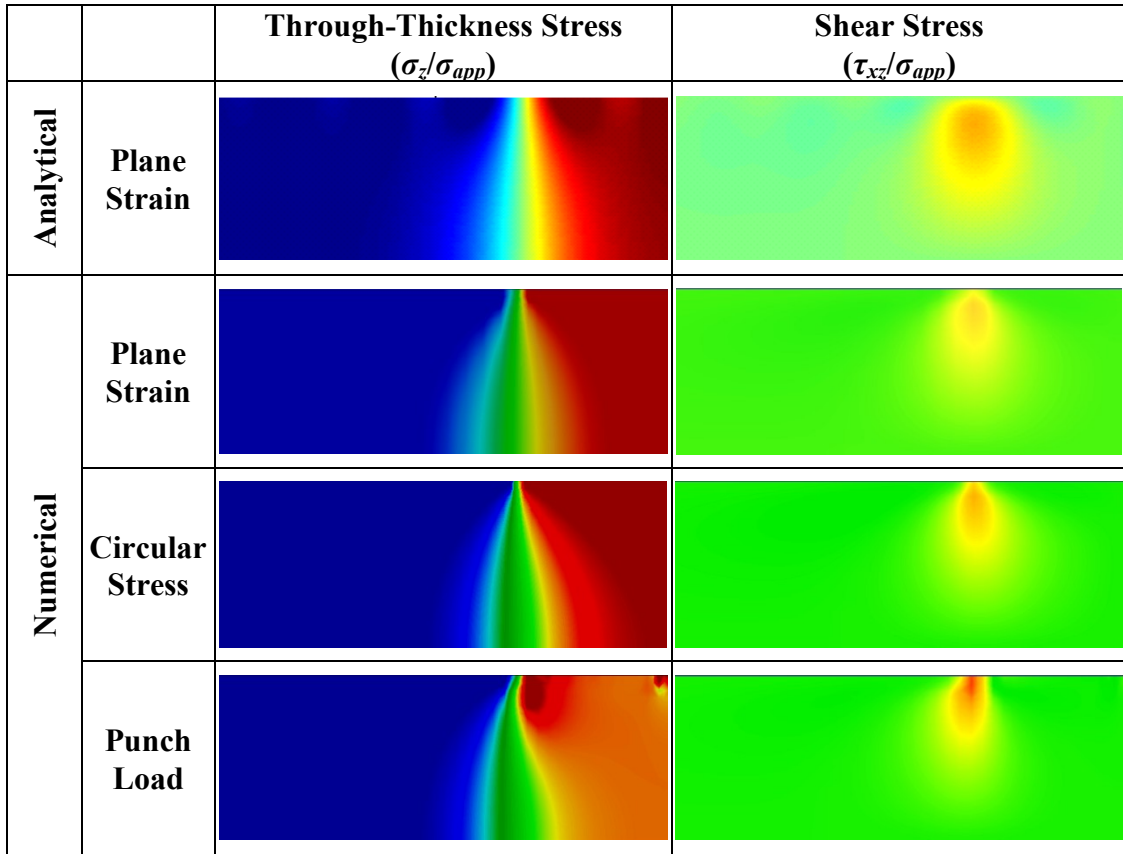


Figure 2.12 – Comparison of stress distributions for analytical model and different numerical loading assumptions (12.70-mm punch, 6.99-mm sample)

plane strain assumption is acceptable. However, discrepancies are noted between the uniform stress loadings and punch loading, as expected. These differences will necessitate that any analytical conclusions using an infinite transverse ( $y$ -axis) strip loading be validated against the numerical model of the experimental setup. Nonetheless, the analytical model provides insights into the geometric parameters governing scaling laws for the punch-composite system, as will be discussed in Chapter 5.

Additional assumptions were made for the boundary conditions of the problem. The assumption of a frictionless rigid support is common to both the analytical and numerical models. In the experimental fixture, the steel of the base plate is approximately ten times as stiff as the composite, making the assumption of rigidity acceptable. Both the fixture and specimen surface are smoothed at their contact. While this does not validate the assumption of a frictionless surface, this was found to be more acceptable than an assumption of perfect adhesion between the specimen and the fixture. The final boundary assumption is of lateral constraint at the specimen edges. While this assumption does not match the experimental or numerical setup, Chapter 4 will demonstrate that the edge effects become negligible under certain conditions.

Analytical calculations were performed by deriving the material coefficients shown in equations (2.7-2.9) using Maplesoft's Maple software (Maple 13) and encoding these equations in MathWorks' MATLAB software (MATLAB v7.6.0 R2008a). The analytical formulation provided the state of stress at a point of interest. The specimen domain was discretized into a set of at least 20,000 points in MATLAB for which the state of stress was computed. While the solution is in the

form of a Fourier series, summation of a finite number of terms is necessary for computation. An analysis of the convergence of the transverse ( $x$ ) and through-thickness ( $z$ ) stresses at the bottom of the specimen along the axis of loading was performed. It was noted that the number of terms needed for convergence ( $M$ ) was related to the width of the specimen considered ( $L$ ). Figure 2.13 shows the convergence of the through-thickness stress ( $\sigma_z$ ) as  $M$  varies. Figure 2.14 shows a plot of the value of  $M$  needed for convergence as a function of  $L$ , where  $L$  is measured in meters. It was noted that a value of  $M > 400L$  ensured convergence of the solution. A value of  $M = 500L$  was used in the MATLAB program.

The MATLAB code was programmed to display results visually, similar to output in CATIA. Results could also be output to Microsoft Excel for more detailed analysis as needed.

## **2.6 Chapter Summary**

The manufacturing methods used in the present study have been presented in the current chapter. The use of consistent manufacturing ensured consistent material properties for experimental testing, enabling accurate comparisons with analytical and numerical models. The experimental testing and data reduction methodologies employed were described. Numerical and analytical models of the experimental setup were presented as well as assumptions used in their development. Having established consistent methodologies for examining the behavior of S-2/SC15 composites under confined compression, the failure behavior of the composite can be characterized using experimental measurements and observations and numerical modeling.

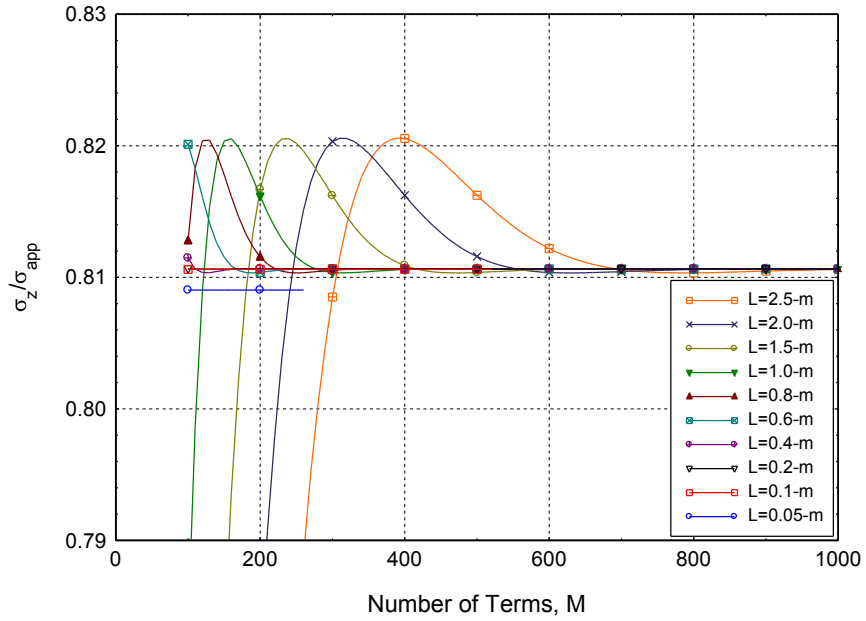


**Figure 2.13 – Convergence of solution for normal stresses ( $\sigma_z$ ) as a function of number of terms ( $M$ ) for various specimen widths ( $L$ )**

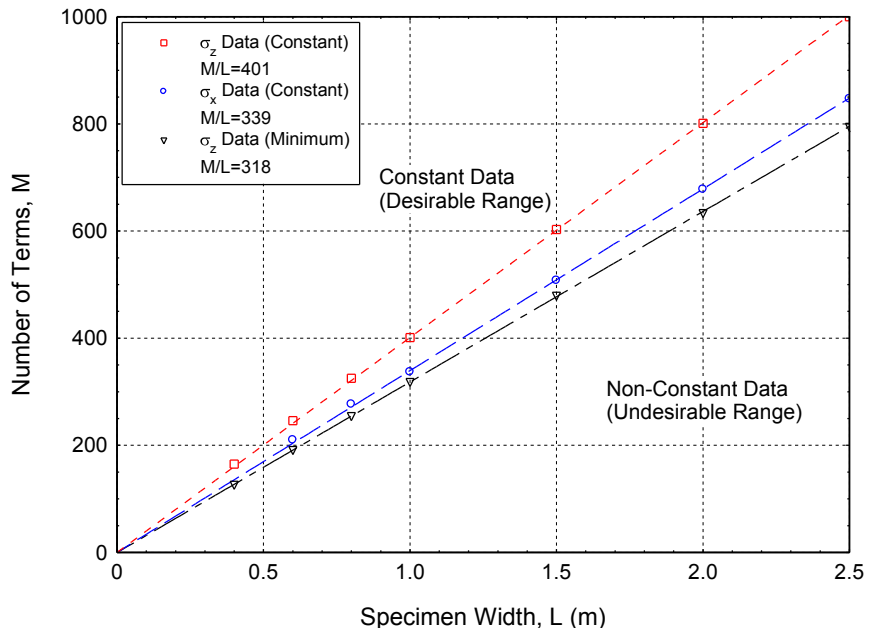


**Figure 2.14 – Calibration of relationship between  $M$  and  $L$**

## **Chapter 3**

### **EXPERIMENTAL FAILURE BEHAVIOR**

Understanding the failure mode of a mechanical system is important for the development of parametric scaling laws. If similar failure modes are demonstrated for specimens with a range of geometries, it would be expected that a single criterion could be discerned to characterize failure for any specimen within the range tested. Conversely, if specimens display distinct modes of failure over a range geometries, different scaling rules would be expected for each damage regime. This chapter explores the observed failure modes and applied stresses for confined compression testing of S-2/SC15 composite specimens as a means of establishing limits on the applicability of potential scaling laws and providing insights into what mechanisms may control such scaling laws.

#### **3.1 Failure Mode**

A typical sectioned specimen is shown in Figure 3.1. Some characteristics of the damage are noted. Diagonal fractures are observed in the region beneath the punch. These fractures pass through both the matrix and fiber materials and appear to initiate at the surface of the composite around the punch periphery. The fractures can be conceptualized as a “plug” of damaged material within the specimen. Similar characteristics were noted for all the specimens examined during experimental testing.



**Figure 3.1 – Confined compression failure (11.09-mm punch, 5.08-mm sample)**

While visual inspection permits an initial understanding of the failure of S-2/SC15 composites under confined compression, a number of questions are raised. Is the angle of fracture constant as specimen thickness and punch diameter vary? As the specimen thickness decreases, the through-thickness stress distribution approaches a uniform state of compression in the specimen beneath the punch. Nearly vertical fractures may be expected for thin specimens, while thick specimens would exhibit a more conical behavior, as seen in Figure 3.1. Additional questions remain about the development of the fractures. What is the local state of stress which leads to fracturing of the composite? Do the fractures initiate in a uniform location? How quickly do they propagate through the composite?

To answer the first of these questions, the fracture angles visible in the photographs of sectioned specimens were measured. The method of measuring is illustrated in Figure 3.2 for the same sample shown in Figure 3.1. Using a program with picture-editing capabilities, such as Microsoft PowerPoint, the photograph of the specimen was aligned such that horizontal surfaces, such as the bottom face of the specimen, were aligned with the horizontal axis of the page. Lines were drawn

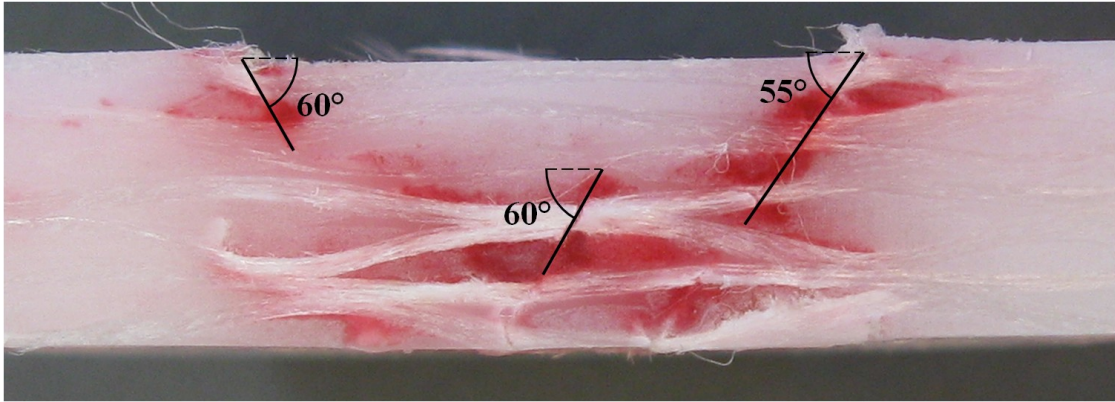


**Figure 3.2 – Measuring fracture angles (11.09-mm punch, 5.08-mm sample)**

concurrent with the fracture orientations in the specimen. By recording the height and width of the imposed lines, the angle of each fracture was calculated.

Once the individual fracture angles were measured for each specimen, their average value was taken as representative of that specimen. This analysis was repeated for a test matrix of 29 specimens with various diameters and thicknesses. The representative fracture angles are presented in Table 3.1 and plotted as a function of diameter (Figure 3.3) and thickness (Figure 3.4). Examination of Figures 3.3 and 3.4 shows some experimental scatter in the data, but no clear trend with respect to either diameter or thickness. It is concluded that the angle of fracture is a characteristic of the material system regardless of specimen geometry. A basic statistical analysis of the data is presented in Table 3.2. It is observed that the standard deviation and coefficient of variation are both reasonable for the entire data set, suggesting a characteristic fracture angle is indeed valid. It is also observed that the deviations in fracture angle measurements within each specimen is minimal, and may be influenced by the smaller sampling size within each specimen.

**Table 3.1 – Experimental test matrix with fracture angle values,  $\theta$  (in degrees)**

		<u>Punch Diameter, <math>D_p</math>, mm</u>					
		<b>6.27</b>	<b>7.62</b>	<b>7.92</b>	<b>10.16</b>	<b>11.09</b>	<b>12.70</b>
<u>Specimen Thickness, <math>H_c</math>, mm</u>	<b>20.83</b>	---	56	---	56	---	57
	<b>13.72</b>	---	51	---	56	---	50
	<b>7.62</b>	58	---	57	---	53	57
	<b>7.11</b>	---	50	---	55	---	57
	<b>6.35</b>	57	---	55	---	55	54
	<b>5.08</b>	60	---	62	---	60	50
	<b>3.81</b>	58	---	55	---	54	51
	<b>2.54</b>	50	---	56	---	58	55

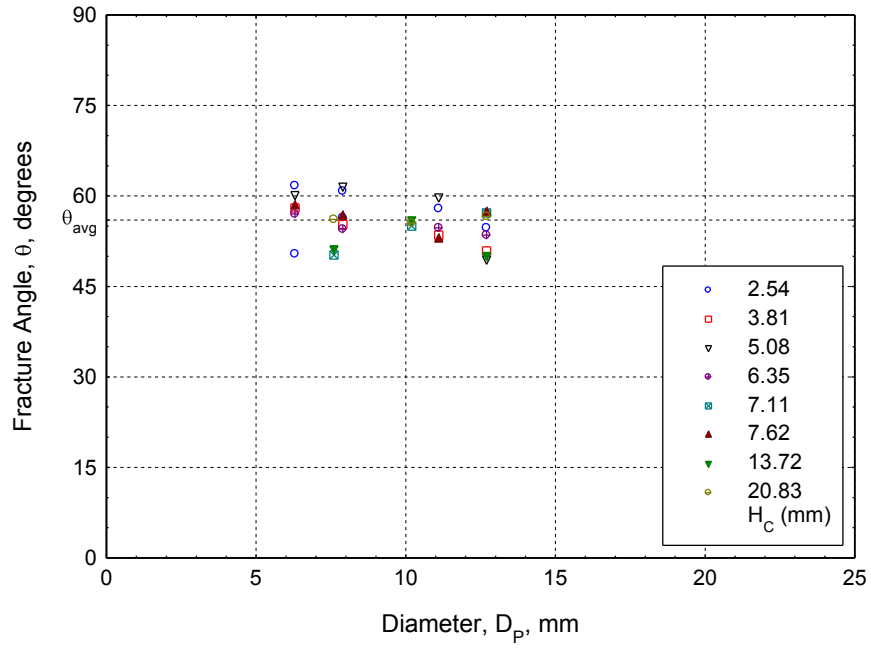


**Figure 3.3 – Fracture angle as a function of punch diameter**

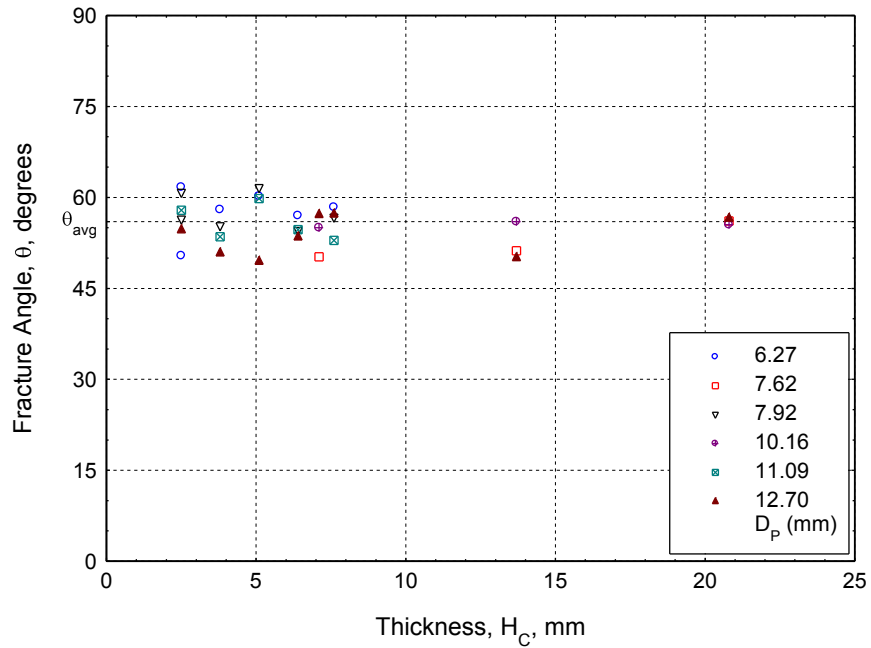


**Figure 3.4 – Fracture angle as a function of specimen thickness**

**Table 3.2 – Statistical analysis of fracture angle**

<b>Complete Data Set</b>			<b>Averages from Specimens</b>	
<b>Average Angle</b>	<b>Standard Deviation</b>	<b>Coefficient of Variation</b>	<b>Standard Deviation</b>	<b>Coefficient of Variation</b>
55.6°	3.4°	6.2%	4.8°	8.8%

### **3.1.1 Off-Axis Fracture Angles**

It is important to note that the results presented above were drawn from sectioning planes intentionally chosen to align with the fiber orientation in the composite (i.e. a 0°/90° orientation). For a plain-weave composite, such as the S-2/SC15 composite tested in the present work, specimen behavior may vary between the 0°/90° orientation, where fiber properties dominate, and the 45° (off-axis) orientation, where matrix properties have a greater influence. This characteristic of composites could lead to a different characteristic fracture angle in the off-axis direction.

Using the methodology presented above, a subset of six specimens were sectioned along a plane in the 45° orientation passing through the axis of loading. The re-sectioned specimens were again dyed and photographed, and the angles were measured as described above. A comparison of the sections in the 0°/90° and 45° orientations is shown in Figure 3.5. It was noted that similar fractures occur in the off-axis planes. Moreover, these fractures appear to form at the same angles as those fractures in the 0°/90° planes. Table 3.3 compares the average measured angles and their deviation for both on-axis and off-axis cases. While some variation does exist

between the two, this variation is found to be less than the standard deviations for the two sectioning planes. In addition, there was no distinct trend relating to whether the off-axis fracture angles were smaller or larger than the on-axis case; the distributions appear to be random, as illustrated in Figure 3.5. Based on these observations, it is concluded that the fractures created during the confined compression test form at a characteristic angle. For S-2/SC15 composites, experimental calculations estimate this characteristic fracture angle to be  $56^\circ$ . It is noted that Yen et al. (2004) obtained a similar value of  $53^\circ$  for the fracture angle of S-2/SC15 composites by performing confined compression testing using a different experimental setup.

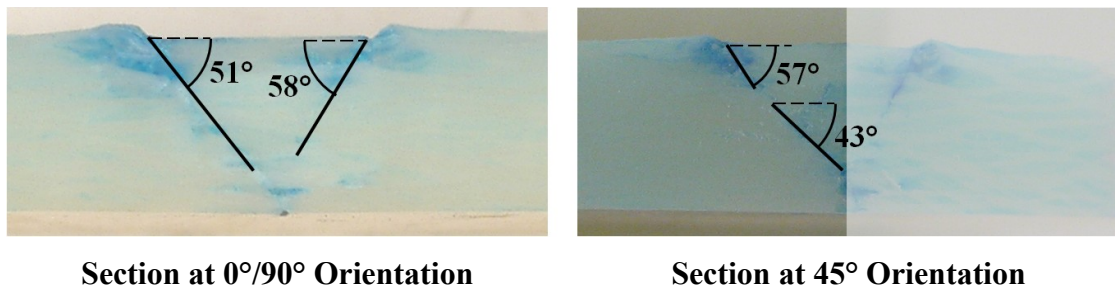


**Figure 3.5 – Comparison of fracture angles on different sectioning planes  
(10.16-mm punch, 7.11-mm sample)**

**Table 3.3 – Comparison of average fracture angles on different sectioning planes**

<u>0°/90° Orientation</u>		<u>45° Orientation</u>	
<b>Average</b>	<b>Standard Deviation</b>	<b>Average</b>	<b>Standard Deviation</b>
54.3°	±8.4°	51.5°	±8.6°

### 3.1.2 Defining “Thin” and “Thick” Specimens

If the angle of fracture is assumed to be constant, the damaged region in the composite specimen can be idealized as a conical “plug” of material. The height of this plug,  $H_p$ , can be estimated knowing the angle of fracture and the diameter of the punch:

$$H_p = \frac{1}{2} D_p \tan \theta \quad (3.1)$$

This relationship is illustrated in Figure 3.6.

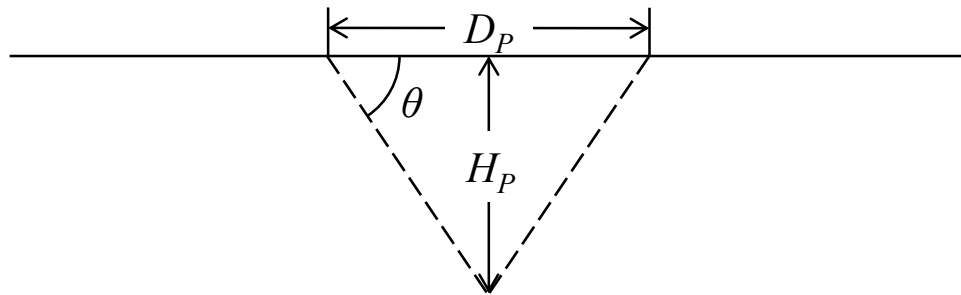


**Figure 3.6 – Schematic of idealized fracture plug formations**

If a specimen has a thickness which is less than the theoretical plug height (i.e.  $H_C < H_p$ ) the fracture angles would be expected to propagate through the specimen to the support, forming a “truncated cone”. A specimen with greater thickness (i.e.  $H_C > H_p$ ) will fracture completely within the specimen, with no effect from the support. This change in plug formation is used to define a “thin” and “thick” specimen, respectively. Using equation (3.1) these “thickness regimes” can be expressed mathematically:

$$\begin{aligned}
 H_C < \frac{1}{2} D_P \tan \theta &\rightarrow \text{"in"} \\
 H_C \geq \frac{1}{2} D_P \tan \theta &\rightarrow \text{"nick"}
 \end{aligned}
 \tag{3.2}$$

The difference between interactions of the plug either with the “rigid” support or with the softer undamaged composite material could reasonably be expected to affect the stress distribution of the specimen at failure. In the remainder of this study, these two thickness regimes will be considered as geometric sets with potentially distinct behaviors.

### 3.2 Applied Stress at Failure

The typical force-displacement relationship for confined compression testing of S-2/SC15 composites is presented in Figure 3.7. The load drop in Figure 3.7 is assumed to represent the initiation of fracturing in the specimen, as verified by sectioning of specimens. The peak load at this load drop, normalized by the area of the punch to define an applied stress, is taken to be the applied load (stress) at the initiation of failure. The relationship between this applied stress and diameter and thickness was studied using the test matrix of 29 experimental specimens with various thicknesses and punch diameters. The combinations used and corresponding values of applied stress are shown in Table 3.4. The applied stresses at failure for all specimens are also plotted as a function of diameter and thickness in Figures 3.8 and 3.9, respectively.

It is noted that, although some scatter exists in the data, the applied stress remains relatively invariant as a function of both diameter and thickness (see Figures 3.8 and 3.9). A basic statistical analysis of the data in Table 3.4 likewise suggests that the applied stress has an average value  $\sigma_{avg} = 887$  MPa regardless of specimen

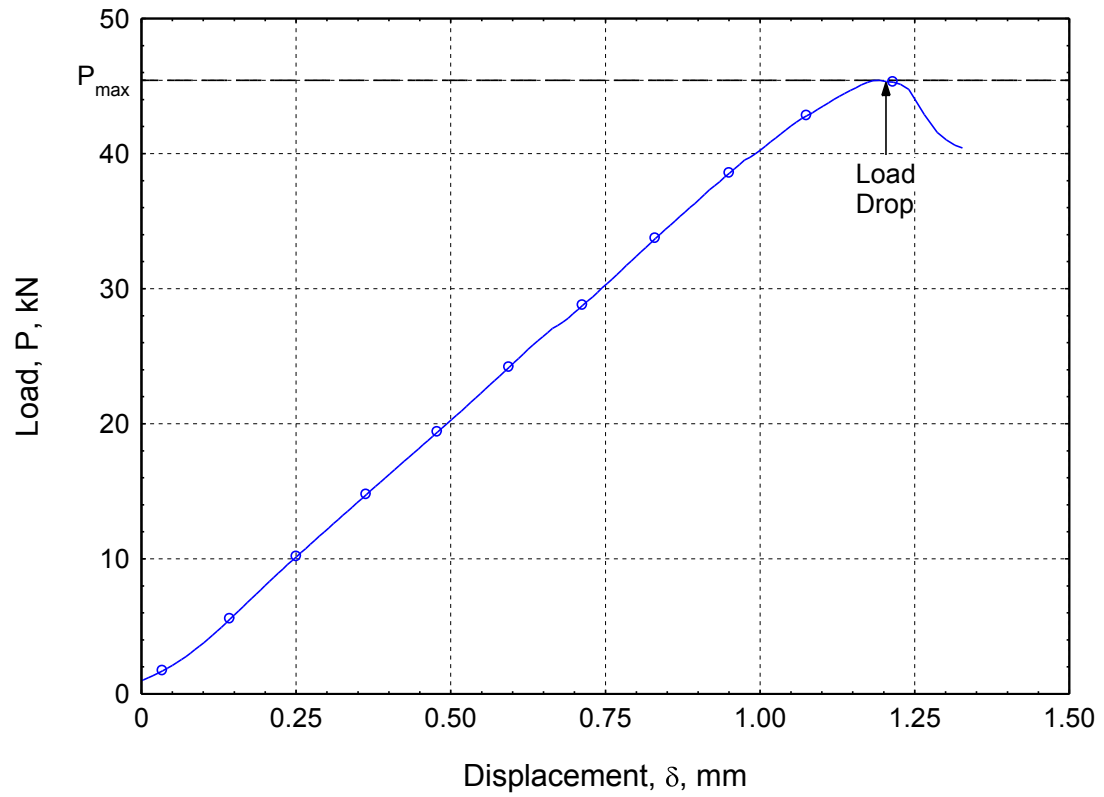


**Figure 3.7 – Force-displacement curve (7.62-mm punch, 7.11-mm sample)**

**Table 3.4 – Experimental test matrix with applied stress values,  $\sigma_{app}$  (in MPa)**

		<u>Punch Diameter, <math>D_p</math>, mm</u>					
		<b>6.27</b>	<b>7.62</b>	<b>7.92</b>	<b>10.16</b>	<b>11.09</b>	<b>12.70</b>
<u>Specimen Thickness, <math>H_c</math>, mm</u>	<b>20.83</b>	---	868	---	924	---	903
	<b>13.72</b>	---	752	---	951	---	718
	<b>7.62</b>	912	---	898	---	822	933
	<b>7.11</b>	---	996	---	913	---	838
	<b>6.35</b>	851	---	819	---	832	820
	<b>5.08</b>	954	---	991	---	877	895
	<b>3.81</b>	870	---	856	---	787	870
	<b>2.54</b>	974	---	1014	---	1059	831

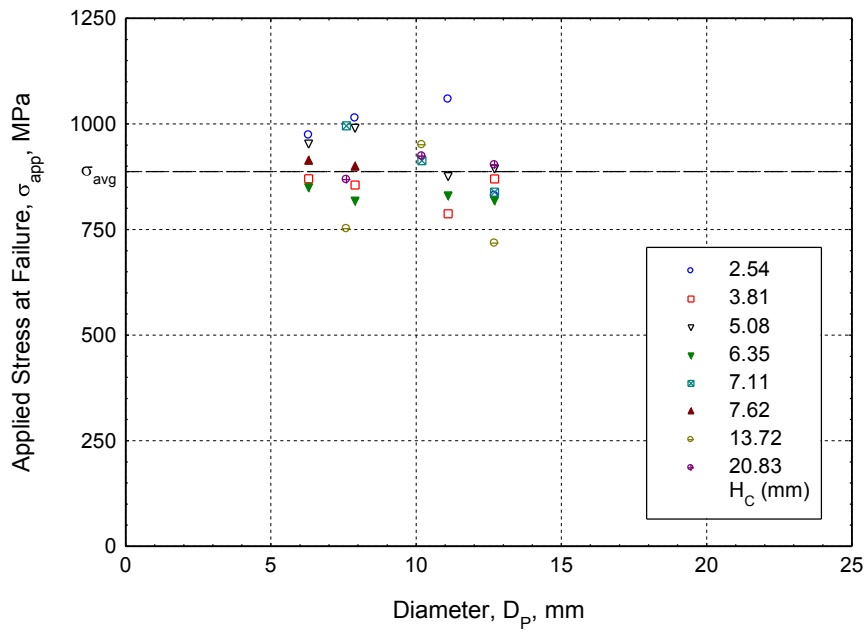


**Figure 3.8 – Applied stress at failure as a function of punch diameter**

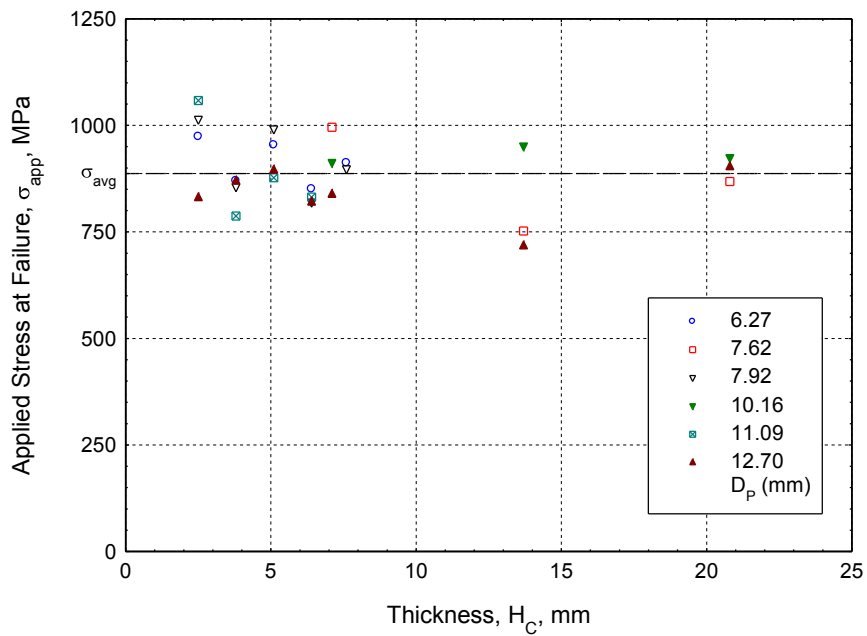


**Figure 3.9 – Applied stress at failure as a function of specimen thickness**

geometry, with a standard deviation of 78 MPa and a coefficient of variation of 8.8%. Given the randomness of the scatter in the data in Figures 3.8 and 3.9, this error is considered reasonable.

The result of a characteristic applied stress for initial failure regardless of specimen thickness is inconsistent with expected behavior. As the specimen becomes thinner (or the punch becomes larger) the stress distribution is expected to exhibit more uniform compression. To conceptualize this expected change in behavior, a cylindrical “column” of material defined by the punch diameter (Figure 3.10) is considered. Performing a force balance in the vertical direction on this column gives:

$$P_{app} = \tau_{Periphery} + \tau_{Support} \quad (3.3)$$

where  $P_{app}$  is the force applied by the punch,  $F_{Periphery}$  is the shear reaction force acting on the sides of the column, and  $F_{Support}$  is the normal reaction force acting at the specimen support. Equation (3.3) can also be expressed using the average stress components acting on the hypothetical column of material:

$$\sigma_{app} \frac{\pi D_p^2}{4} = \tau_{avg} (\pi D_p H_C) + \tau_{support} \frac{\pi D_p^2}{4} \quad (3.4)$$

The average stress components can be expressed in terms of the forces on the column or integrals of the stress distributions acting on the column:

$$\tau_{avg} = \frac{F_{Periphery}}{\pi D_p H_C} = \frac{\int (\tau_{rz} \cos \phi + \tau_{rz} \sin \phi) dA}{\pi D_p H_C} \quad (3.5)$$

$$\sigma_{support} = \frac{F_{Support}}{\frac{\pi}{4} D_p^2} = \frac{\int \tau_z dA}{\frac{\pi}{4} D_p^2} \quad (3.6)$$

The expression within the integral in equation (3.5) is intended to capture the radial shear stress, with the angle  $\phi$  being measured from the  $x$ -axis.

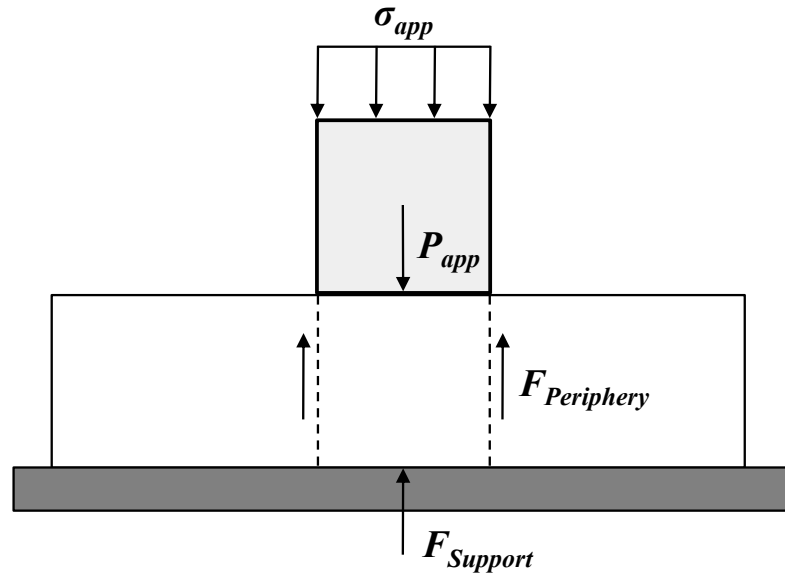


**Figure 3.10 – Force reactions on a “column” of material beneath the punch**

Increases in  $F_{Periphery}$  indicate shear-dominated behavior while increases in  $F_{Support}$  indicate compression-dominated behavior. A comparison of these two reaction forces as a ratio with the applied load ( $P_{app}$ ) is shown in Figure 3.11 for a 12.70-mm punch using results from the numerical model. It is observed that compressive behavior does dominate for thinner specimens, while shear behavior is more prevalent for thicker specimens. This change in internal behavior with specimen geometry suggests that the applied stress at initial failure should also vary with specimen geometry.

A similar force balance can be performed for the radial ( $x$  and  $y$  direction) forces acting on the “column” in Figure 3.10. Because no external forces act in the  $x$  or  $y$  directions, all internal forces are self-equilibrating. Stresses arising from the Poisson expansion of the column are counteracted by confining stresses produced by the undamaged material outside the column. These confining stresses can be

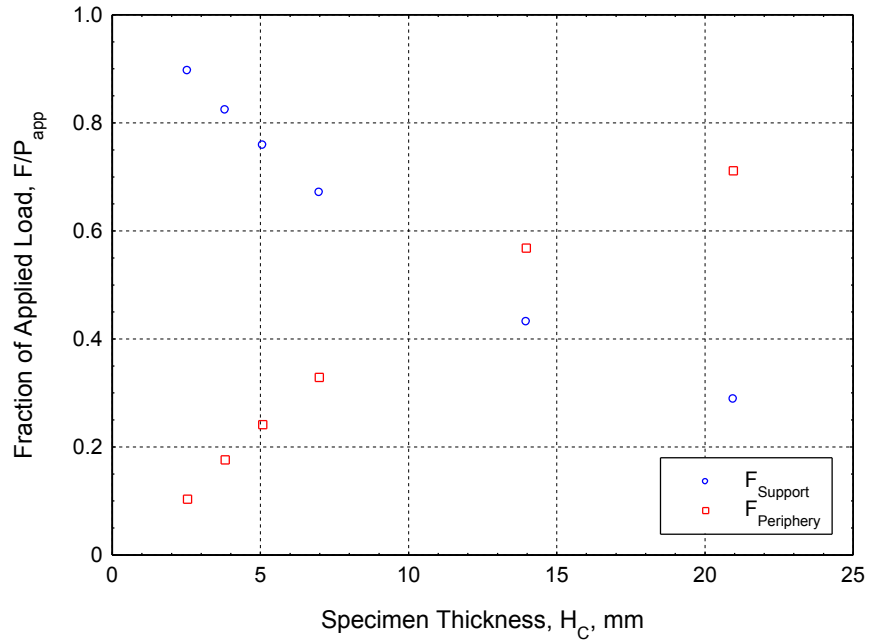


**Figure 3.11 – Comparison of normal and shear reactions (12.70-mm punch)**

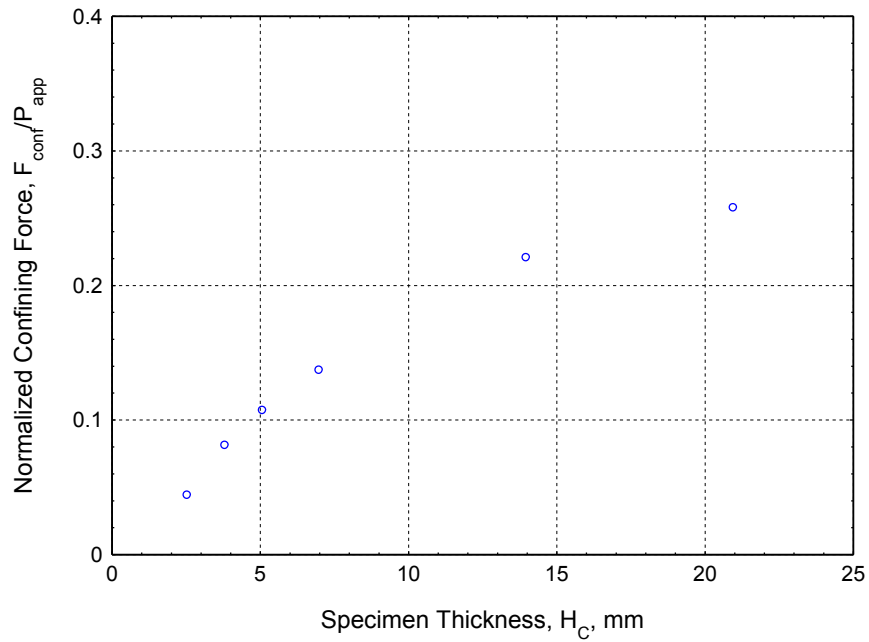


**Figure 3.12 – Normalized confinement vs. specimen thickness (12.70-mm punch)**

integrated over the surface area of the column to yield a net confining force,  $F_{conf}$ . Using the numerical model, the ratio of  $F_{conf}$  to the applied force  $P_{app}$  for specimens of various thicknesses loaded with a 12.70-mm punch was plotted in Figure 3.12. It is observed that the value of the confining force increases with increasing thickness. This result is expected, since a thicker column will experience greater through-thickness displacement and exhibit greater Poisson expansion effects.

The observed experimental applied stress behavior (Figures 3.8 and 3.9) contradicts the behavior of the internal applied stresses (Figure 3.11). The consistent fracture behavior for all geometries (Section 3.1) also contradicts the varying behavior of the internal stresses. These observations raise the question of what combination of stress interactions give a characteristic applied stress and fracture mode despite the variations in the internal stresses. Chapter 6 will present a more detailed analysis of the internal stress distributions and use various failure criteria to explain this contradiction of the confined compression test.

### **3.3 Stresses on the Fracture Plane**

To begin investigating the stress interactions in confined compression specimens, the internal stresses in the specimen were transformed into components on the fracture plane. Such a transformation enables an analysis of the stress state that is causing fractures to form. Based on the observation of a characteristic fracture angle regardless of specimen geometry or circumferential location with respect to the punch, it was assumed that the stress components in the radial direction (i.e.  $xz$ -plane) were rotated by an angle  $\theta$ , but that the stress components in the circumferential direction (i.e.  $y$ -axis) remained unrotated. The transformation is illustrated in Figure 3.13, with the  $y$ -axis going into the page.

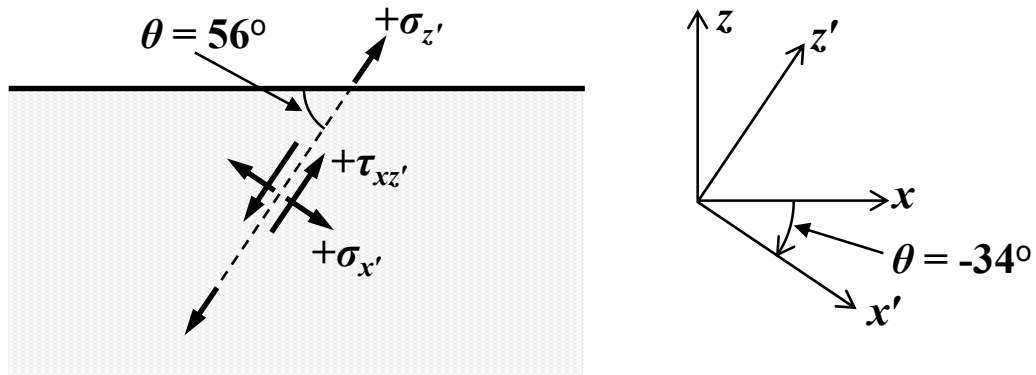


**Figure 3.13 – Schematic of transformation of stresses into fracture plane**

Directional cosines were defined to transform the stresses from the material coordinates ( $x$ - $y$ - $z$ ) into the fracture plane ( $x'$ - $y'$ - $z'$ ) described above (Boresi & Schmidt, 2003, p 31):

$$\begin{matrix} x' \\ y' \\ z' \end{matrix} \begin{bmatrix} x & y & z \\ \cos \theta & 0 & \sin \theta \\ 0 & 1 & 0 \\ -\sin \theta & 0 & \cos \theta \end{bmatrix} \quad (3.7)$$

Knowing the directional cosines it is possible to define the transformed stress components in term of the stresses in the material coordinates (Boresi & Schmidt, 2003, p 32):

$$\sigma_{x'} = \frac{\tau_x + \tau_z}{2} + \frac{\tau_x - \tau_z}{2} \cos 2\theta + \tau_{xz} \sin 2\theta \quad (3.8)$$

$$\sigma_{z'} = \frac{\tau_x + \tau_z}{2} - \frac{\tau_x - \tau_z}{2} \cos 2\theta - \tau_{xz} \sin 2\theta \quad (3.9)$$

$$\tau_{xz'} = -\frac{\tau_{xz} - \tau_{yz}}{2} \sin 2\theta + \tau_{xz} \cos 2\theta \quad (3.10)$$

$$\sigma_{y'} = \tau_{yz} \quad (3.11)$$

$$\tau_{xy'} = \tau_{yz} \sin \theta + \tau_{xy} \cos \theta \quad (3.12)$$

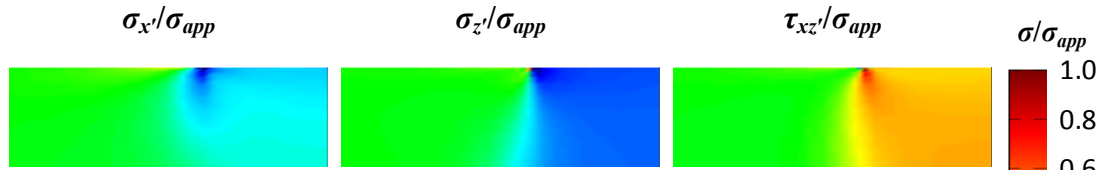
$$\tau_{yz'} = \tau_{yz} \cos \theta - \tau_{xy} \sin \theta \quad (3.13)$$

It is noted that equations (3.8-3.10) are the same as those for a two-dimensional transformation of stress (Hibbeler, 2005, pp 456-458). Since the  $y$ -axis is not rotated, the normal component of stress ( $\sigma_y$ ) remains unchanged, although the shear stresses on the  $xy$  and  $yz$ -planes are transformed.

Some comment is also necessary on the choice of a value for  $\theta$ . While the fracture plane is oriented at  $56^\circ$ , maintaining the  $x$ -direction across the fracture and the  $z$ -direction along the fracture necessitated a rotation of  $-34^\circ$ . This is illustrated in Figure 3.13.

Representative stress distributions in the fracture plane orientation are shown in Figure 3.14 for both a “thin” and a “thick” specimen using results from the numerical model. It is noted in both cases that the stresses acting across the fracture face (i.e.  $\sigma_{x'}$ ) are compressive. Thus the fracture is not formed due to tensile failure; rather, compressive stresses act to keep the fracture plane closed. Likewise, the stresses acting parallel to the fracture (i.e.  $\sigma_{z'}$ ) are compressive. However, the shear stresses along the fracture plane (i.e.  $\tau_{xz'}$ ) are positive. Referring to Figure 3.13, it is noted that positive shear corresponds to the kind of sliding fracture a confined compression test would cause. It was also noted that the circumferential normal and shear stresses (i.e.  $\sigma_{y'}$ ,  $\tau_{xy'}$ , and  $\tau_{yz'}$ ) were at most 30% of the maximum value of the

**12.70-mm punch, 5.08-mm sample**



**12.70-mm punch, 13.97-mm sample**

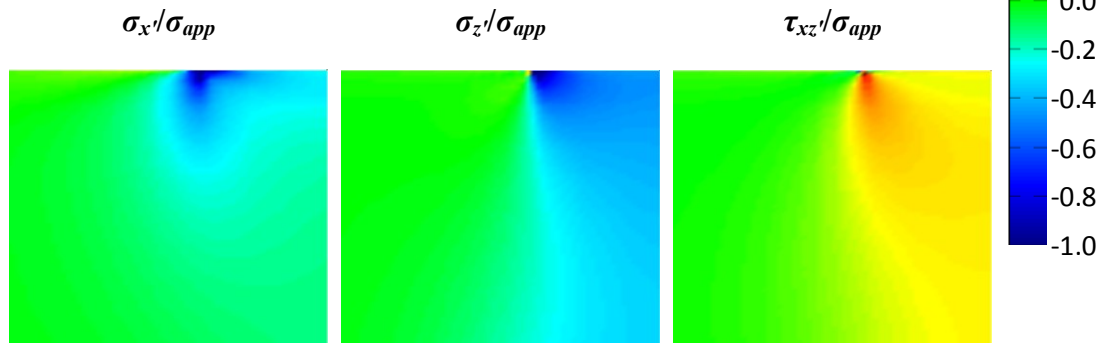


**Figure 3.14 – Comparison of transformed stresses on the fracture plane for a “thin” and a “thick” specimen**

shear and normal stresses on the fracture plane. This suggests that the radial stress components will dominate the fracture behavior.

These observations suggest that fractures in the specimens are caused by a compression-shear interaction on the fracture plane, initiating at the punch periphery. It is also noted that the shear stress distribution is slightly more uniform in the “thin” specimen (see Figure 3.14). This characteristic may explain why fractures tend to proliferate throughout the width of the plug for “thin” specimens, but not for “thick” specimens. The observation of a compression-shear interaction will be considered in Chapter 6 to explain the contradictory experimental applied stress behavior described previously. The development of an appropriate failure criterion for this behavior will also be used to determine the locations of crack initiation.

### **3.4 Chapter Summary**

In the present chapter the failure behavior of S-2/SC15 composite specimens under confined compression was examined. Cross-sectioning of specimens showed diagonal fractures of the fibers as the main failure mode. Fractures were observed to occur at a characteristic angle regardless of the dimensions of the punch and specimen and the orientation with respect to the fibers. While the fracture mechanism appeared consistent regardless of geometry, it was noted that the “cone” of damaged material either propagated to the support or was contained within the specimen. This criterion was used to define “thin” and “thick” specimens, which may exhibit different behaviors.

A similar analysis of the applied stress to initiate failure was performed. It was observed that the value of applied stress remains constant for all punch diameters and specimen thicknesses considered. This behavior was seen to be contradictory to

the internal stress distribution, which is more shear-dominated for thicker specimens and more compression-dominated for thinner specimens. To begin exploring how dissimilar stress states lead to similar applied failure stresses, the stress components were transformed into the fracture plane at the characteristic angle. It was seen that a compression-shear interaction exists along the fracture. It was concluded that the fracture is caused by shearing failure of the fibers. The observations discussed in this chapter motivate the analysis of various failure criteria presented in Chapter 6.

## Chapter 4

### MINIMUM SPECIMEN WIDTH

#### 4.1 Background

When performing experimental and numerical studies, it is typically impractical and undesirable to test extremely large samples. Ideally, one goal of an experimental setup should be to minimize the size of the specimen to conserve the amount of material used in testing. However, this desire for minimum size must be balanced with the need for consistent behavior regardless of specimen size.

To conceptualize the calculation of the minimum experimental specimen width, a confined compression test that is carried out on a hypothetical circular specimen with a diameter equal to the punch diameter is considered. As the specimen is compressed along the axis of the punch ( $z$ -axis), bulging would occur in the transverse and longitudinal directions ( $x$  and  $y$ -axes) due to Poisson expansion effects. If a ring of material were added around the specimen, it would provide added lateral confinement, restricting the Poisson expansion in the  $x$  and  $y$ -directions. However, at some critical width the addition of further material would provide no additional confinement.

For any specimen with a diameter greater than this critical width the load path from the punch to the support would not pass through the additional material. Therefore the stress distribution within the specimen would remain the same, regardless of the amount of additional material. Calculating this critical width ensures

that all specimens are sufficiently large to allow for the maximum possible load distribution (i.e. the amount of load distribution expected in a specimen of infinite width).

## 4.2 Analytical Calculation

The critical specimen width for S-2/SC15 composites under confined compression was initially calculated using Milovic's analytical solution for an infinite longitudinal ( $y$ -direction) strip load (see equations (2.7-2.9)). The critical width for a given specimen, denoted as  $L_{crit}$ , was defined as the diameter at which the stress normal to the support ( $\sigma_z$ ) becomes zero. This choice is rationalized as follows. The load path through the specimen passes from the punch to the support. At the diameter where the stress normal to the support becomes zero, the load from the punch has been completely transferred into the support and no additional load distribution is expected. Any material beyond this value of  $L_{crit}$  will not affect the stress distribution within the specimen. This definition of  $L_{crit}$  is illustrated in Figure 4.1.

In calculating the critical width it was recognized that, for a given material, the critical width could be a function of both the diameter of the punch and the thickness of the specimen. Stress distributions on the support were calculated for two diameters (12.70-mm and 25.40-mm) with a variety of thicknesses and two thicknesses (12.70-mm and 25.40-mm) with a variety of diameters. Plots of these stress distributions for a varying thickness (constant diameter) and varying diameter (constant thickness) are shown in Figures 4.2 and 4.3, respectively.

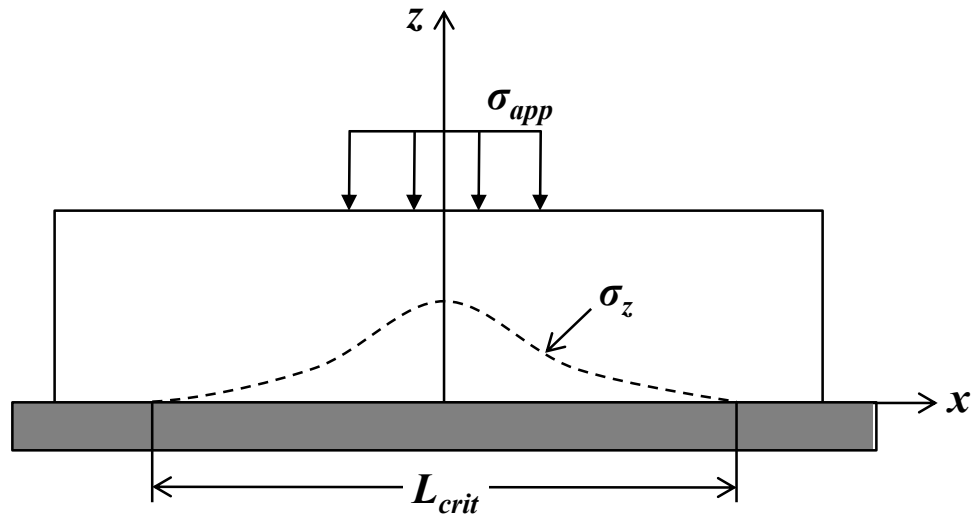


**Figure 4.1 – Schematic of definition of critical width,  $L_{crit}$**

Using the data from the plots in Figures 4.2 and 4.3, the coordinate at which the support stress became zero was identified. Some characteristics of these stress distributions were also noted. For specimens with a large punch diameter to specimen thickness ratio the stress distribution in the region below the punch has an almost constant value equal to the applied stress, but drops off to zero almost immediately outside the punch. For specimens with a small punch diameter to specimen thickness ratio, the stresses are more distributed, since the greater thickness allows for a greater distribution by the load path.

Once all values of  $L_{crit}$  were measured for the given specimens, they were plotted as a function of either thickness or diameter. These plots are shown in Figures 4.4 and 4.5 for the stress distributions shown in Figures 4.2 and 4.3, respectively. Plots of  $L_{crit}$  as functions of thickness and diameter are also shown in Figures 4.6 and

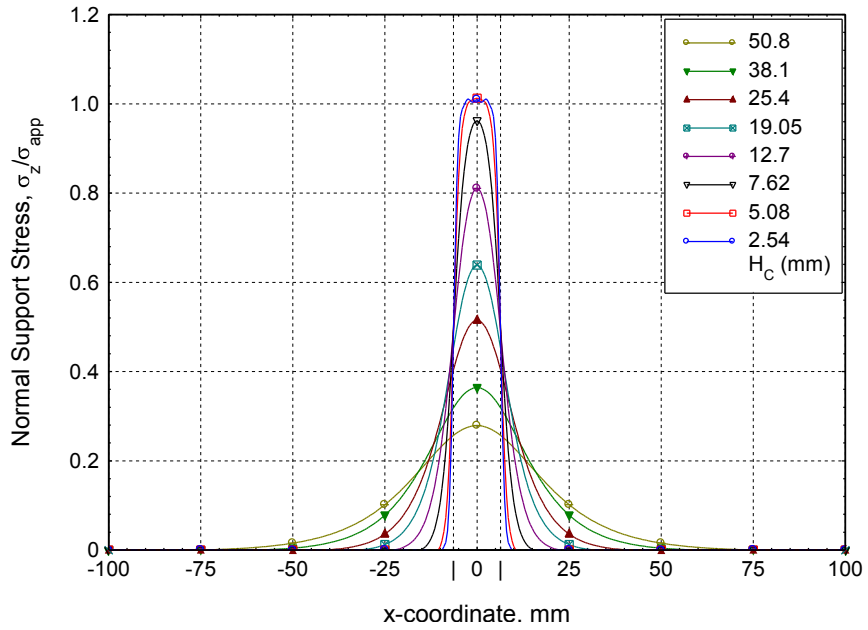


Figure 4.2 – Stress distributions for varying thickness (12.70-mm punch)

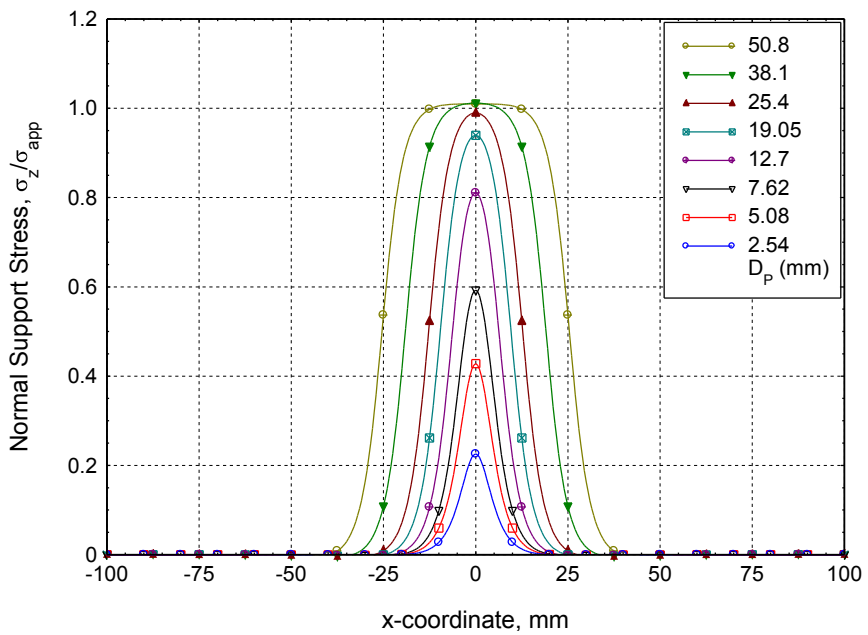


Figure 4.3 – Stress distributions for varying diameter (12.70-mm sample)

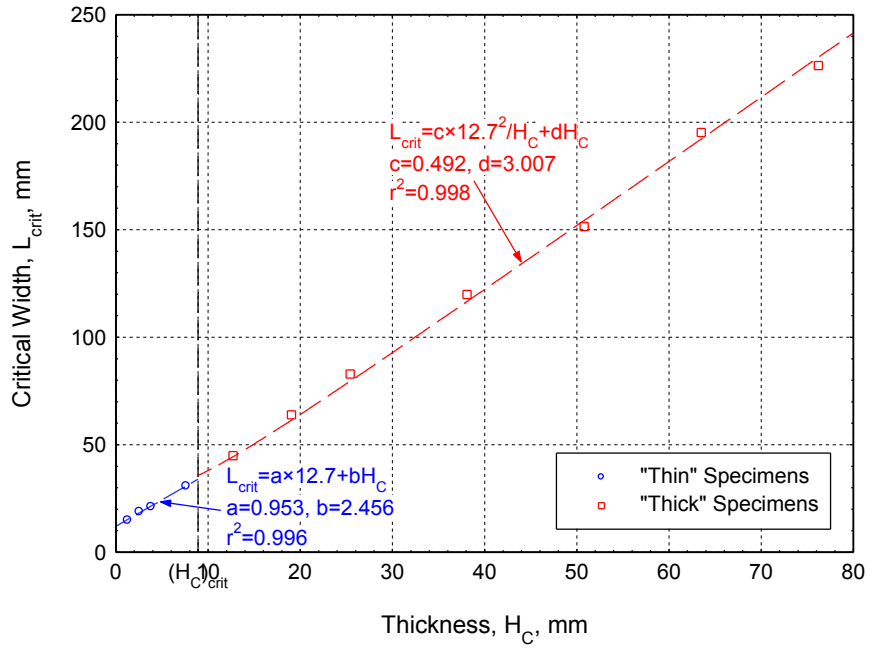


Figure 4.4 – Critical width as a function of thickness (12.70-mm punch)

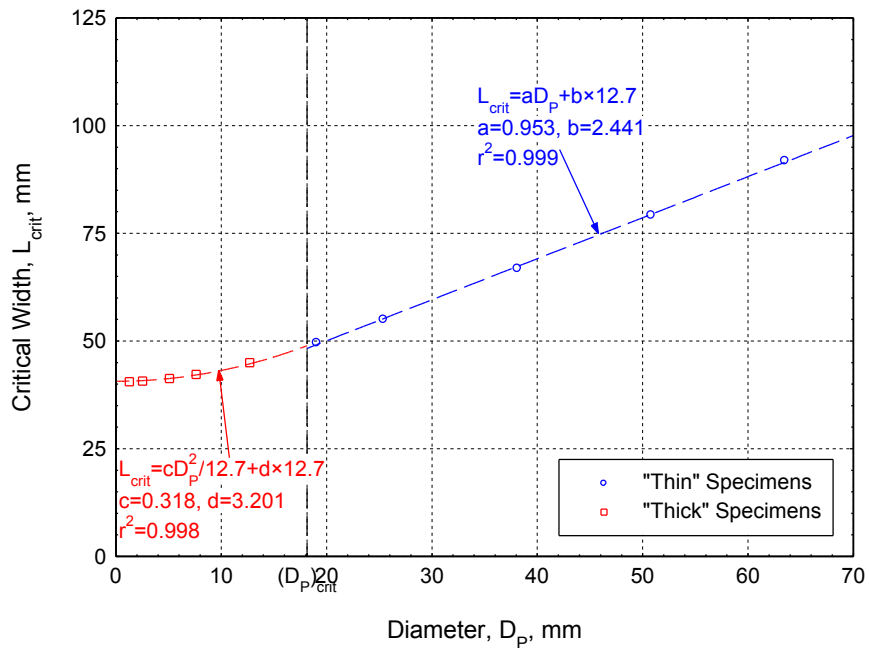


Figure 4.5 – Critical width as a function of diameter (12.70-mm sample)

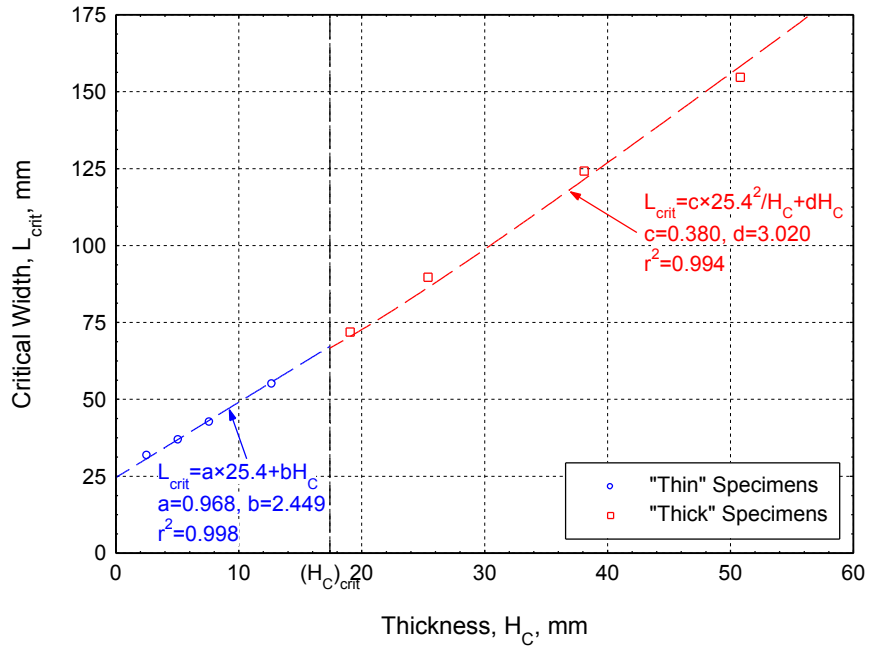


Figure 4.6 – Critical width as a function of thickness (25.40-mm punch)

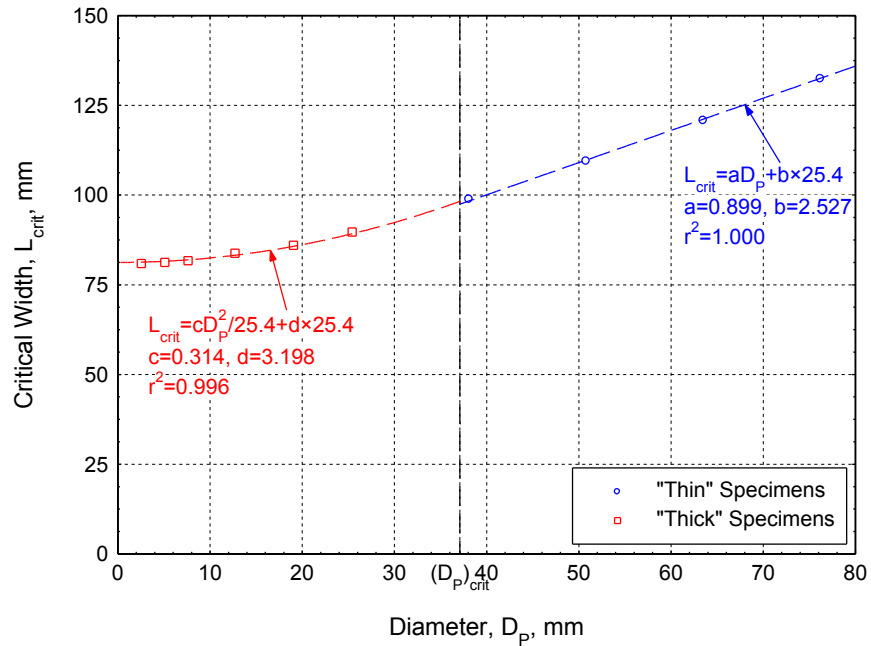


Figure 4.7 – Critical width as a function of diameter (25.40-mm sample)

4.7 for  $D_P = 25.4$ -mm and  $H_C = 25.4$ -mm, respectively. In Chapter 3 it was noted that two “thickness regimes” existed for the specimens based on fracture depth, and that these two regimes could potentially exhibit different behaviors. The results presented in Figures 4.4-4.7 suggest that this is the case for critical width. The thickness or diameter at the boundary between the regimes (i.e.  $(H_C)_{crit}$  or  $(D_P)_{crit}$ ) is noted in all figures.

A regression analysis was performed on the data, expecting that  $L_{crit}$  would be a simple polynomial function of  $H_C$ ,  $D_P$ , or a combination of the two. These fitting curves and equations are shown in Figures 4.4-4.7. Recognizing that the functional forms for the individual parameters ( $H_C$  and  $D_P$ ) should match in a more general functional form including both parameters, the following general equations for  $L_{crit}$  were developed:

$$L_{crit} = aD_P + bH_C \text{ (thin)} \quad (4.1)$$

$$L_{crit} = c\frac{D_P^2}{H_C} + dH_C \text{ (thick)} \quad (4.2)$$

where  $a$ ,  $b$ ,  $c$ , and  $d$  are fitting coefficients. The coefficients for equations (4.1) and (4.2) were calculated from the fitting curves in Figures 4.4-4.7. By averaging the values of the fitting coefficients obtained, the equations for  $L_{crit}$  for the S-2/SC15 composite were found to be:

$$L_{crit} = 1.95D_P + 1.48H_C \text{ (thin)} \quad (4.3)$$

$$L_{crit} = 1.36\frac{D_P^2}{H_C} + 1.11H_C \text{ (thick)} \quad (4.4)$$

The correlation coefficients between equations (4.3) and (4.4) and the data in Figures 4.4-4.7 are shown in Table 4.1. It should also be noted that the error in the value of  $L_{crit}$  at the intersection of equations (4.3) and (4.4) is 0.11%.

**Table 4.1 – Correlation of equations (4.3) and (4.4) with data in Figures 4.4-4.7**

<b>Const. Dim.</b>	$D_p = 12.70\text{-mm}$	$H_C = 12.70\text{-mm}$	$D_p = 25.40\text{-mm}$	$H_C = 25.40\text{-mm}$
<b>Assoc. Figure</b>	Figure 4.4	Figure 4.5	Figure 4.6	Figure 4.7
<b><math>r^2</math> Coefficient</b>	0.996	0.997	0.996	0.991

Limits exist for the applicability of the expressions for  $L_{crit}$  in equations (4.3) and (4.4). The use of the analytical solution necessitates an assumption of material homogeneity. Specimens with  $H_C$  less than a single ply thickness or  $L_{crit}$  smaller than the unit cell of the fabric are likely to exhibit distinguishable matrix and fiber behaviors, violating the assumption of homogeneity. The specimens considered in the present study are significantly larger than these bounds, and usage of equations (4.3) and (4.4) is valid. The curve fitting in Figures 4.4-4.7 was performed for the range  $1.27\text{-mm} < H_C < 76.20\text{-mm}$  and  $1.27\text{-mm} < D_p < 63.50\text{-mm}$ . Extrapolation of equations (4.3) and (4.4) outside these ranges should not be performed. All specimen-punch combinations tested in the present study fall within these ranges.

#### **4.2.1 Effect of Varying Moduli on $L_{crit}$**

It is important to note that the coefficients in equations (4.3) and (4.4) are purely empirical fits to the normal stress distribution decay behavior for the S-2/SC15 composite. The fitting coefficients shown in equations (4.3) and (4.4) are not valid for different material systems. A parametric study of the effect of the three moduli ( $E_x$ ,  $E_z$ , and  $G_{xz}$ ) was performed to explore the effect of varying these moduli on the stress

distribution normal to the specimen support. The results of this analysis are shown in Figure 4.8 for a specimen with  $D_P = H_C = 12.70$ -mm.

Each modulus was varied by doubling or halving its value relative to the baseline S-2/SC15 composite material (see Table 2.1) while holding the other moduli constant at their baseline values. Analysis of Figure 4.8 leads to observations about the effects of these moduli on  $L_{crit}$ . Increasing the axial modulus ( $E_x$ ) causes a slight increase in the spread of the stresses normal to the support. Recalling that increasing the modulus tends to draw load, this increase in the spread of stresses in the axial direction is expected. Increasing the through-thickness modulus ( $E_z$ ) causes a more pronounced decrease in the spread of the stresses normal to the support. This increase should tend to transfer more load in the through-thickness direction, which would decrease the axial spread of the stresses, as observed. Lastly, increasing the through-thickness shear modulus ( $G_{xz}$ ) causes a significant increase in the spread of the stresses normal to the support. An increase in the shear modulus should increase the transfer of stresses from the through-thickness to axial directions, as observed. It is also noted that  $E_z$  and  $G_{xz}$  have a much greater effect on the value of  $L_{crit}$  than  $E_x$ , though  $E_x$  still has a measureable effect on the stress distribution at the support.

From the proceeding discussion, it is apparent that the values of  $L_{crit}$  are highly dependent on the properties of material tested. Therefore, the values of  $L_{crit}$  given in equations (4.3) and (4.4) are only valid for the S-2/SC15 composite material considered in the present study. Different equations for  $L_{crit}$  should be derived for different materials, following a methodology similar to that presented above.

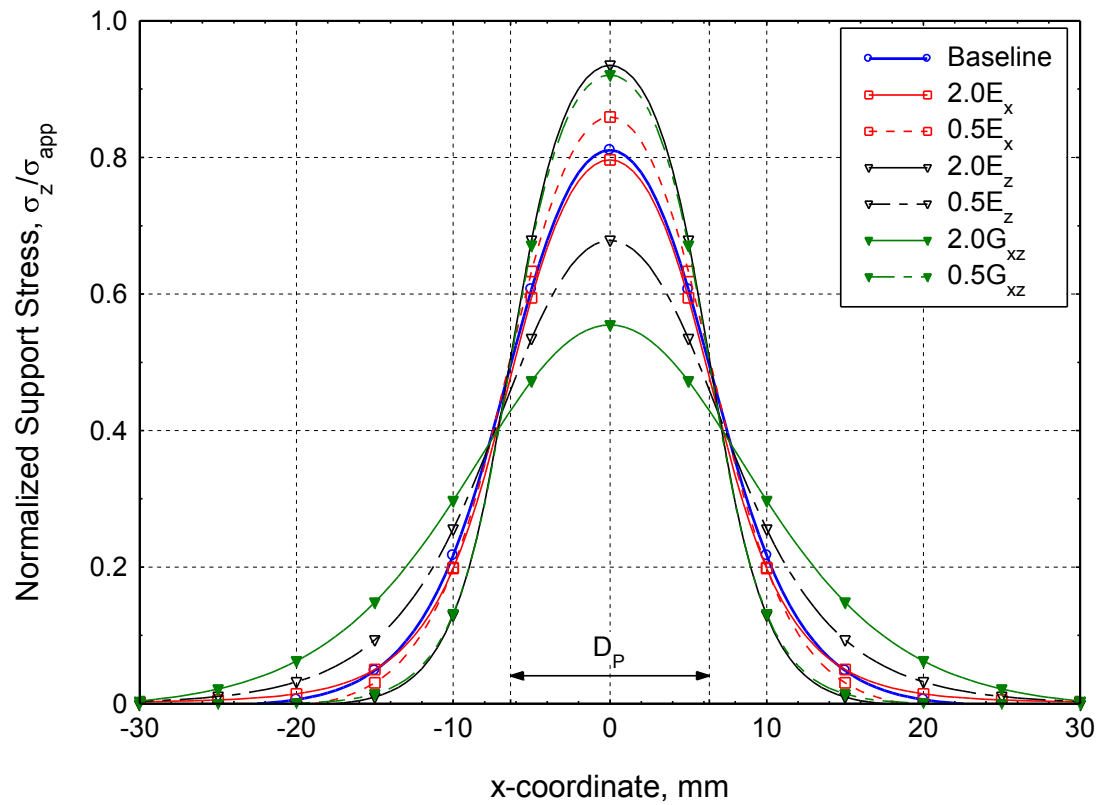


**Figure 4.8 – Effect of varying moduli on the stress distribution normal to the support (12.70-mm punch, 12.70-mm sample)**

#### 4.2.2 Off-Axis Verification of $L_{crit}$

Equations (4.3) and (4.4) for  $L_{crit}$  were calculated from stresses in the fiber ( $0^\circ/90^\circ$ ) orientation. Because of the anisotropy of composite materials, the effective material properties will be different between the fiber direction ( $0^\circ/90^\circ$  orientation), where the stiffer fibers allow for greater lateral redistribution of the load, and off-axis orientations (e.g.  $45^\circ$ ), where the fiber properties are less dominant. From the discussion in Section 4.2.1 it is noted that different properties in the off-axis orientation will likely lead to different values of  $L_{crit}$ . Therefore it is important to verify that the values of  $L_{crit}$  given by equations (4.3) and (4.4) are conservative for all circumferential orientations.

The off-axis moduli were calculated using the Composite Design and Simulation (CDS) software developed at the University of Delaware's Center for Composite Materials (CDS v2.0.2b). The material properties from Table 2.1 were used to define an S-2/SC15 composite lamina. The lamina was then rotated  $45^\circ$  transversely (i.e. about the  $z$ -axis) and the material properties calculated for the unrotated global axes were recorded. The resulting off-axis properties are shown along with the  $0^\circ/90^\circ$  orientation properties in Table 4.2. It is seen that the through-thickness moduli (i.e.  $E_z$ ,  $G_{xz}$ , and  $G_{yz}$ ) are unchanged by the transformation.

**Table 4.2 – Comparison of material properties in the 0°/90° and 45° orientations**

	<u>Elastic Moduli</u>			<u>Shear Moduli</u>			<u>Poisson Ratios</u>		
	$E_x$	$E_y$	$E_z$	$G_{xy}$	$G_{xz}$	$G_{yz}$	$\nu_{xy}$	$\nu_{xz}$	$\nu_{yz}$
	<i>GPa</i>	<i>GPa</i>	<i>GPa</i>	<i>GPa</i>	<i>GPa</i>	<i>GPa</i>	---	---	---
<b>0°/90°</b>	27.5	27.5	11.8	2.90	2.14	2.14	0.11	0.18	0.18
<b>45°</b>	7.5	7.5	11.8	12.39	2.14	2.14	0.76	0.06	0.06

The values of  $E_x'$ ,  $\nu_{xy}'$ , and  $\nu_{xz}'$  for the off-axis (45°) orientation were substituted into the analytical model and the analysis presented above was repeated to obtain values of  $L_{crit}$  for the off-axis orientation. Plots of  $L_{crit}$  in the off-axis orientation as a function of thickness and diameter are presented in Figures 4.9 and 4.10, respectively, and compared with the curves from the fiber orientation. It is noted that the value of  $L_{crit}$  in the 45° orientation is always less than the value of  $L_{crit}$  in the 0°/90° orientation. The decrease in influence from the fibers in the off-axis orientation causes a reduction in the axial modulus ( $E_x$ ), leading to less transverse load distribution for the off-axis orientation. This causes a narrower stress distribution on the support (cf. Figure 4.8), and a lower value of  $L_{crit}$  in the off-axis orientation, as observed. Therefore the expressions for  $L_{crit}$  presented in equations (4.3) and (4.4) are found to be conservative for all circumferential orientations, as desired.

### 4.3 Numerical Validation

The analytical model assumes a uniform strip loading in the longitudinal ( $y$ -axis) direction (see Figure 2.11). However, the experimental punch setup generates

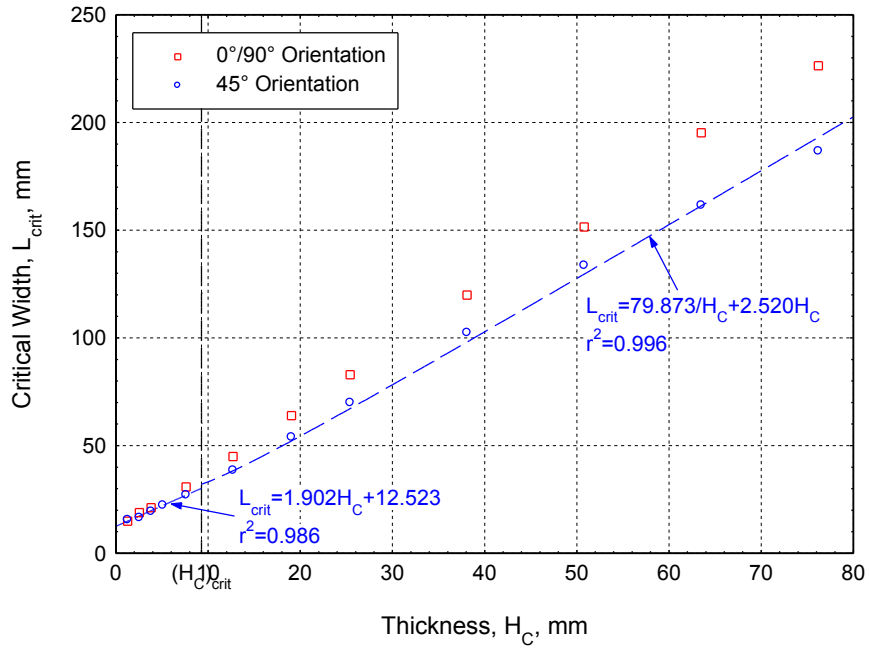


Figure 4.9 – Off-axis critical width as a function of thickness (12.70-mm punch)

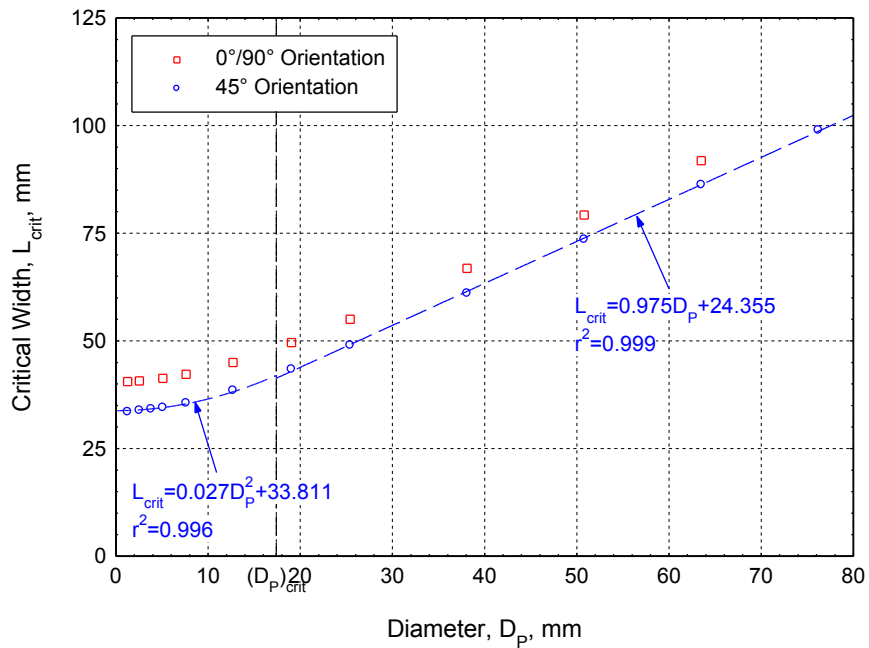


Figure 4.10 – Off-axis critical width as a function of diameter (12.70-mm sample)

stress concentrations at the periphery of the punch. Verification of the expressions for  $L_{crit}$  presented in Section 4.2 is required since the analytical and experimental loadings are different. The estimates of  $L_{crit}$  presented in equations (4.3) and (4.4) were compared with support stress distributions calculated using the finite element model. Two examples of this comparison are shown in Figures 4.11 and 4.12 for a “thin” and a “thick” specimen, respectively. The colors used in the plots show the support stresses as a percentage of the applied load, while the white dashed line shows the location of  $L_{crit}$  calculated for that particular specimen using equation (4.3) or (4.4). It is apparent that the numerical critical width is slightly less than the analytical value in Figure 4.11. The same conclusion is not as apparent in Figure 4.12. However, closer inspection shows that the stress on the support beyond  $L_{crit}$  in Figure 4.12 is less than 0.5% of the applied load and can be considered negligible. Therefore, good agreement is seen between the analytical values of  $L_{crit}$  and the extent of the numerical stress distributions.

To complete the validation of the calculated values of  $L_{crit}$  it is necessary to compare the stress distributions within the specimen for a range of specimen widths larger than  $L_{crit}$ . A comparison of stress distributions from the FE model are shown in Figures 4.13-4.15 for shear stresses at the punch periphery, normal stresses at the specimen surface, and confining stresses at the punch periphery, respectively. For these three figures,  $D_p = 12.70$ -mm and  $H_C = 6.99$ -mm. Employing equation (4.3), the critical width for the specimen is found to be  $L_{crit} = 29.19$ -mm. It is seen that the stress distributions shown in Figures 4.13-4.15 are essentially constant regardless of the width of the specimen, which is always greater than  $L_{crit}$ .

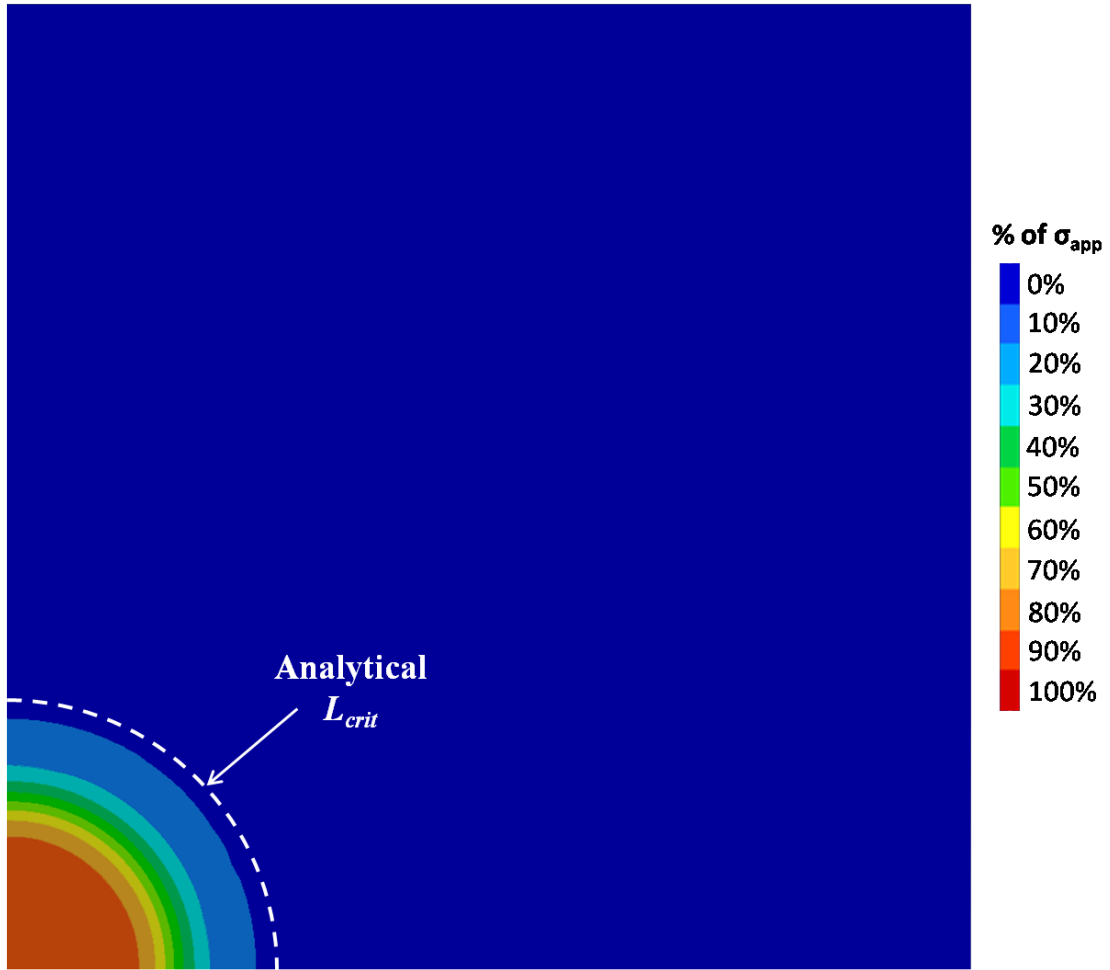


Figure 4.11 – Comparison of numerical stress distribution with analytical value of  $L_{crit}$  (12.70-mm punch, 3.81-mm sample)

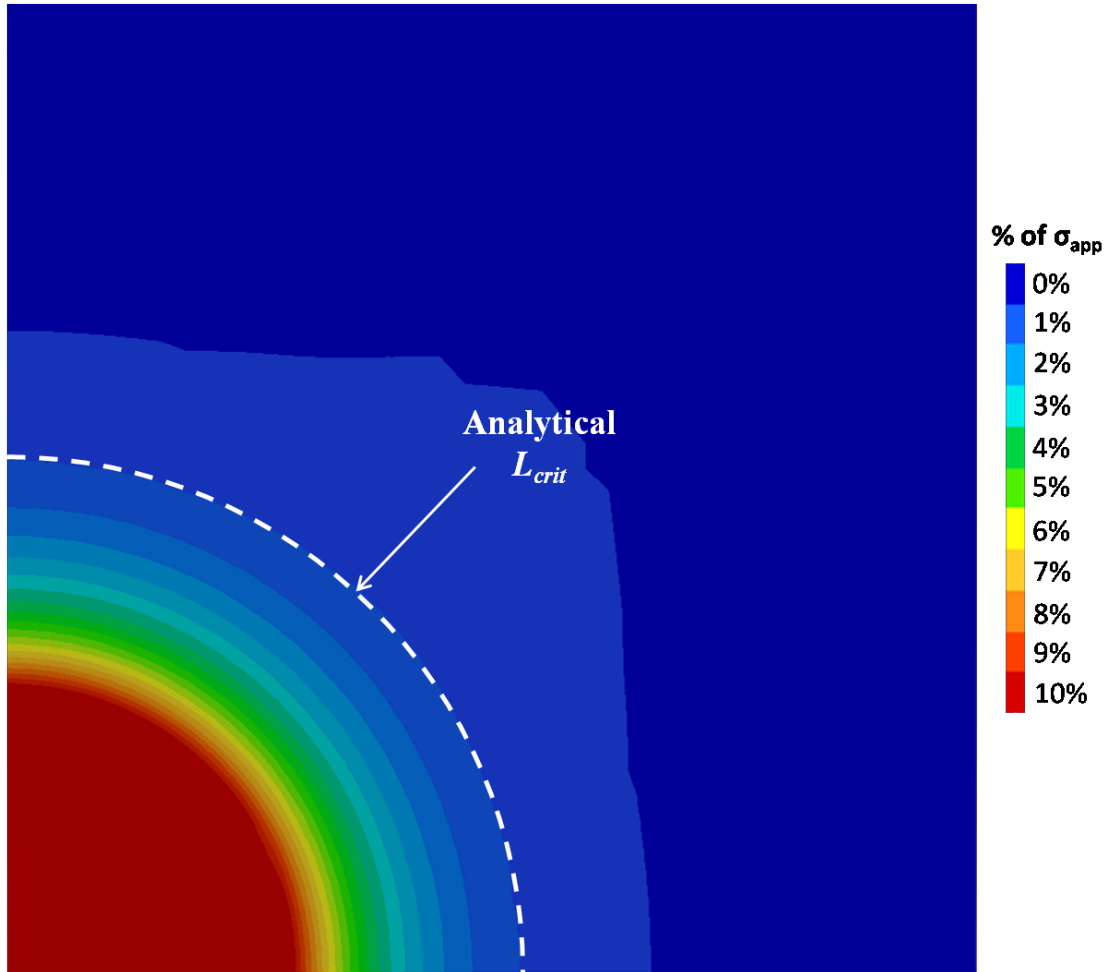
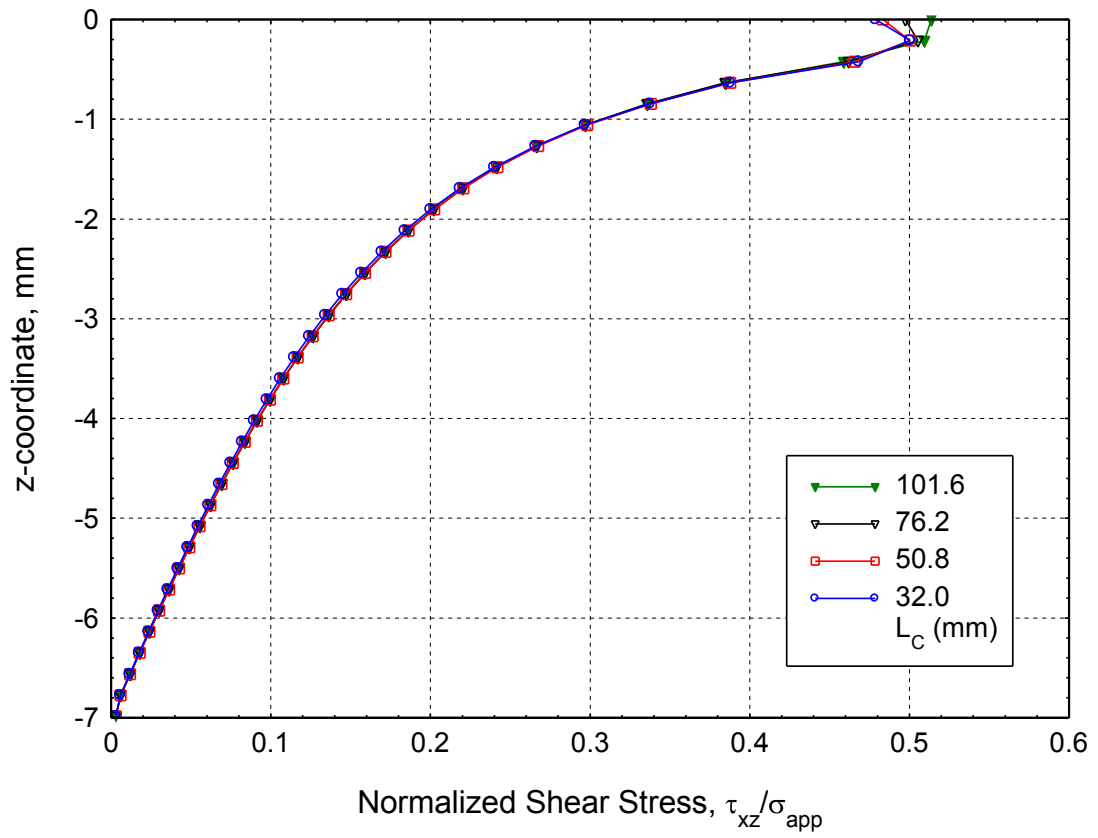
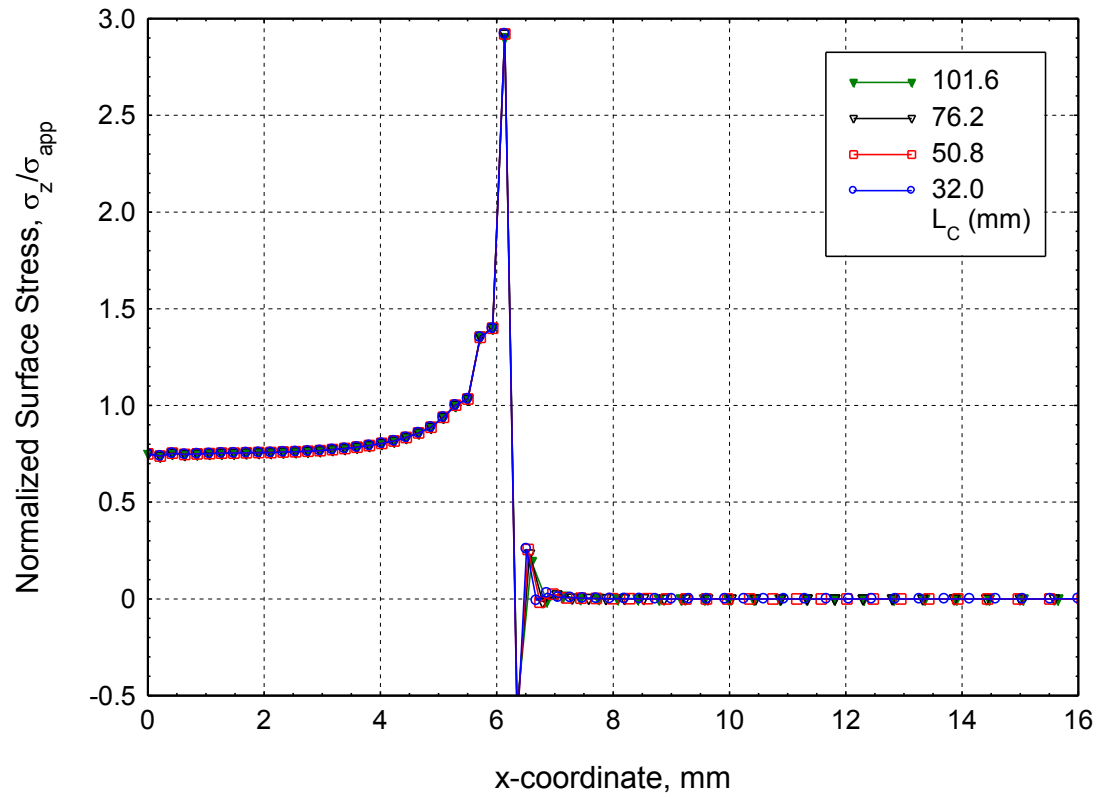


Figure 4.12 – Comparison of numerical stress distribution with analytical value of  $L_{crit}$  (12.70-mm punch, 13.97-mm sample)



**Figure 4.13 – Comparison of shear stress at punch periphery for varying widths,  $L_C$  (12.70-mm punch, 6.99-mm sample)**



**Figure 4.14 – Comparison of normal stress at specimen surface for varying widths,  $L_C$  (12.70-mm punch, 6.99-mm sample)**

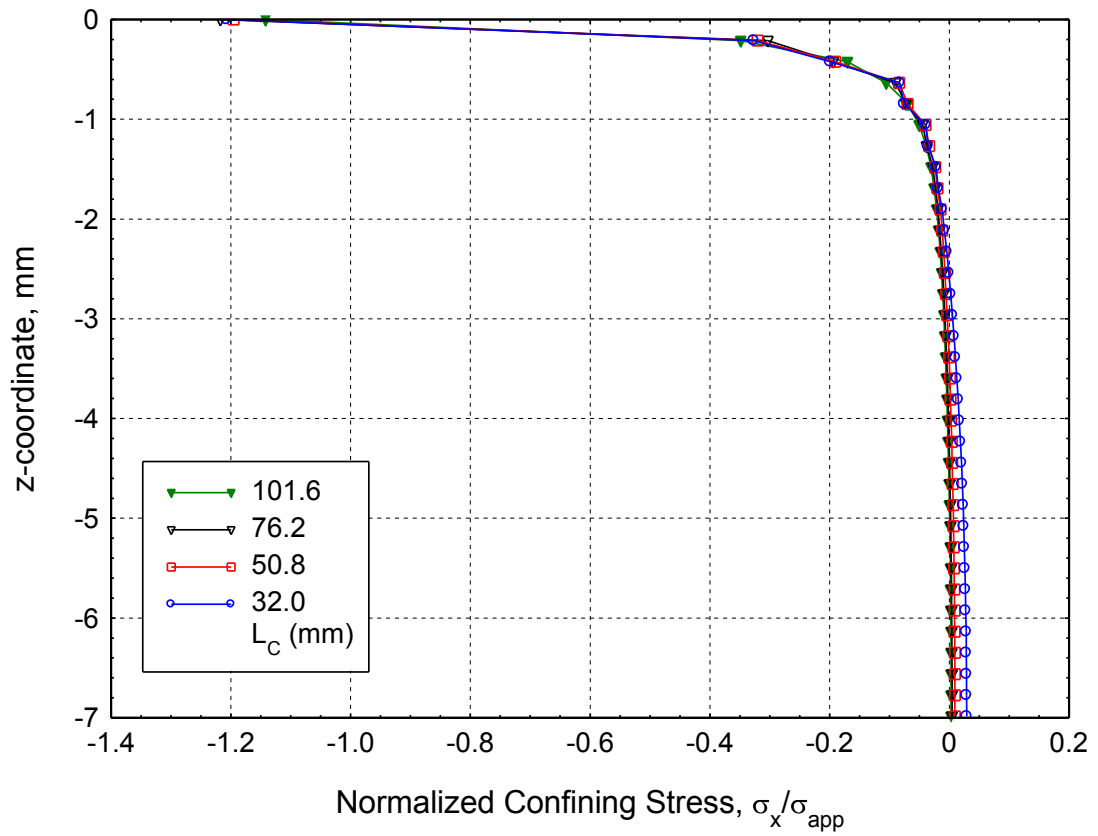


Figure 4.15 – Comparison of confining stress at punch periphery for varying widths,  $L_C$  (12.70-mm punch, 6.99-mm sample)

The discrepancies in the stress distributions are noted to be essentially negligible. The slight differences observed are attributed to minor differences in the location of meshing nodes in the FE model. However, these discrepancies show no trend with specimen width, and are therefore assumed to be random and insignificant. It is also noted that since the three stress components which contribute to the stresses on the fracture plane ( $\sigma_x$ ,  $\sigma_z$ , and  $\tau_{xz}$ ; see equations (3.8-3.10)) are invariant for  $L > L_{crit}$  (see Figures 4.13-4.15), stresses on the fracture plane will also be invariant for  $L > L_{crit}$ .

The consistency of the stress distributions validates the definition of  $L_{crit}$  given in equations (4.3) and (4.4). Using the concept of a maximum area of stress distribution in a specimen, a “critical width” has been defined beyond which additional material provides no additional confining pressure (see Figure 4.15). Using the expressions presented, specimens can be sized for any geometry (i.e. punch diameter and specimen thickness) such that the internal stress distribution is not affected by the specimen width.

#### 4.4 Experimental Comparisons

Table 4.3 shows the values of  $L_{crit}$  for the specimens in the experimental test matrix. Samples with  $L < L_{crit}$  are indicated in boldface and brackets, recalling from Section 2.2 that  $L = 25.4$ -mm for specimens in the mini punch-shear fixture ( $H_C = 2.54, 3.81, 5.08, 6.35,$  and  $7.62$ -mm) and  $L = 76.2$ -mm for specimens in the punch-shear fixture ( $H_C = 7.11, 13.72,$  and  $20.83$ -mm). It is seen that five specimens are below  $L_{crit}$  by more than 1% of  $L_{crit}$ . Figure 4.16 compares the experimentally measured applied stress at failure for specimens with  $L \geq L_{crit}$  and specimens with  $L < L_{crit}$ . It is observed that the specimens which violate the critical width condition show

Table 4.3 – Experimental test matrix with critical width values,  $L_{crit}$  (in mm)

		<u>Punch Diameter, <math>D_p</math>, mm</u>					
		<b>6.27</b>	<b>7.62</b>	<b>7.92</b>	<b>10.16</b>	<b>11.09</b>	<b>12.70</b>
<u>Specimen Thickness, <math>H_c</math>, mm</u>	<b>20.83</b>	---	65.8	---	66.6	---	67.6
	<b>13.72</b>	---	44.2	---	45.4	---	47.0
	<b>7.62</b>	25.6	---	<b>[26.7]</b>	---	<b>[29.2]</b>	<b>[30.8]</b>
	<b>7.11</b>	---	25.1	---	27.1	---	29.5
	<b>6.35</b>	22.0	---	23.4	---	<b>[26.1]</b>	<b>[27.6]</b>
	<b>5.08</b>	18.7	---	20.0	---	23.0	24.5
	<b>3.81</b>	15.3	---	16.9	---	19.8	21.3
	<b>2.54</b>	12.2	---	13.7	---	16.7	18.2

Note: [Boldface and bracketed] terms represent  $L < L_{crit}$

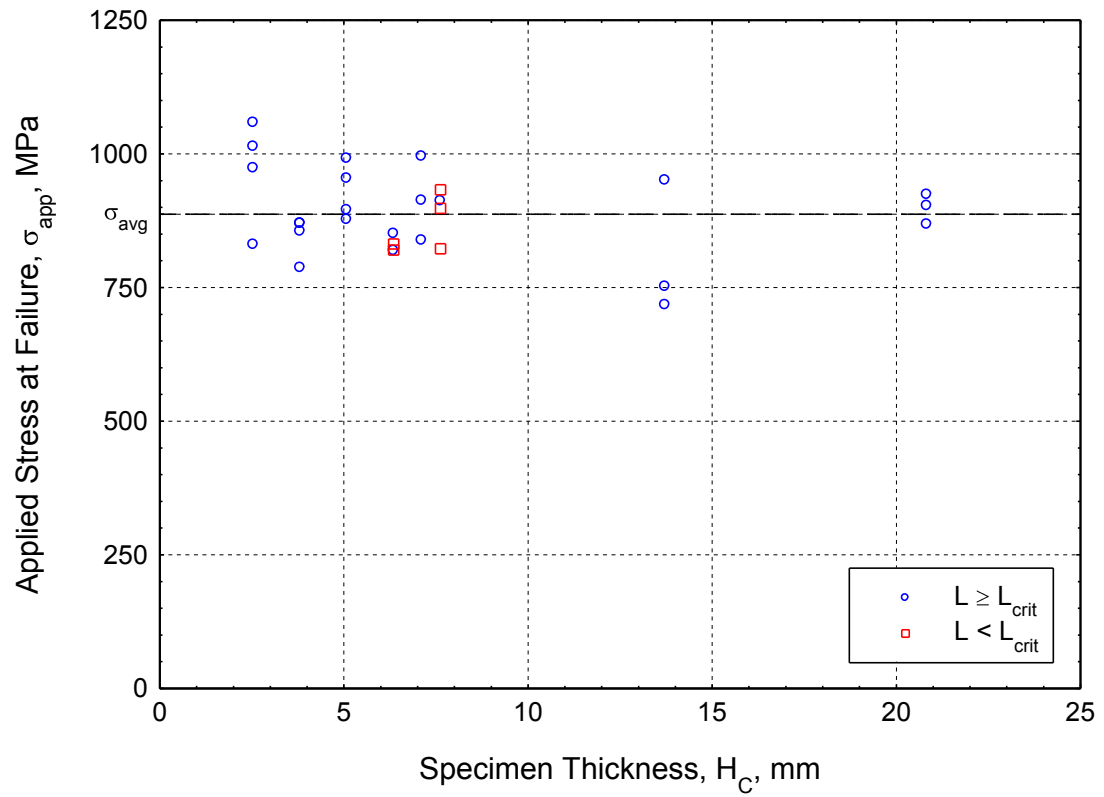


Figure 4.16 – Effect of  $L < L_{crit}$  on the experimental applied stress at failure

no unique trend and all fall within one standard deviation of the experimental average. It is also seen that the greatest deviation of  $L$  from  $L_{crit}$  is 18%. Figure 4.16 suggests that the specimens that violate the critical width condition are still valid for the analysis. It is possible that the value of  $L_{crit}$  given by equations (4.3) and (4.4) is conservative. Figure 4.11 suggests this may be the case, especially for thin specimens. It is also possible that the effects of  $L < L_{crit}$  are only noticeable for  $L \ll L_{crit}$ , and that this threshold is not violated by the specimens considered. Therefore, while having  $L > L_{crit}$  is ideal when sizing experimental specimens, the specimens with  $L < L_{crit}$  in Figure 4.16 demonstrate acceptable agreement for consideration in the remainder of this study.

#### 4.5 Chapter Summary

The present chapter focused on the development of a criterion for the minimum allowable specimen width. Recognizing that an ideal finite-sized specimen should capture all transverse Poisson expansion effects induced by through-thickness compression, the critical width was defined as the diameter at which the stress normal to the support became zero. Using Milovic's analytical model (1992), values of  $L_{crit}$  were calculated for a range of punch and specimen dimensions. Curve-fitting of the analytical results was used to develop two empirical equations for "thin" and "thick" S-2/SC15 specimens in terms of the punch diameter and specimen thickness. A parametric study of the specimen moduli showed that varying the material properties can greatly affect  $L_{crit}$ . Therefore, equations for  $L_{crit}$  were calculated in the off-axis ( $45^\circ$ ) orientation, showing that the value of  $L_{crit}$  calculated in the fiber orientation is most conservative. Comparison of stress distributions from numerical analysis of specimens of various widths showed equivalent behavior for all  $L > L_{crit}$ . This

conclusion ensures that Poisson expansion effects are negligible for all specimens considered and allows for simplifications to Milovic's analytical solution, enabling further parametric analysis.

## Chapter 5

### GEOMETRIC SCALING PARAMETERS

#### 5.1 Problem Parameters

Identifying the parameters present in a physical system is an important step in developing parametric scaling laws for the system (White, 2003, pp 298-301). A schematic of the experimental confined compression setup is shown in Figure 5.1. Three parameters are identified which define the geometry of the system, characterizing its layout. These are the punch diameter ( $D_P$ ) and the specimen thickness ( $H_C$ ) and width ( $L_C$ ). Two additional parameters are identified which define the response of the system, characterizing its behavior. These are the angle of the fracture plane ( $\theta$ ) and the peak stress at failure ( $\sigma_{app}$ ).

The properties of the material forming the specimen and the punch are also important in characterizing the system and would influence any scaling laws. Their importance was demonstrated in Section 4.2.1, where different material properties yielded different values of  $L_{crit}$ . However, since only one consistent material is considered in the present work, the parametric effects resulting from the material are beyond the scope of this study. Likewise, it was demonstrated in Section 3.1 that the angle of fracture is constant for all geometries for the material tested. Therefore, the angle of fracture is not expected to be influenced by the geometric parameters of the problem, although material parameters would likely affect the angle.

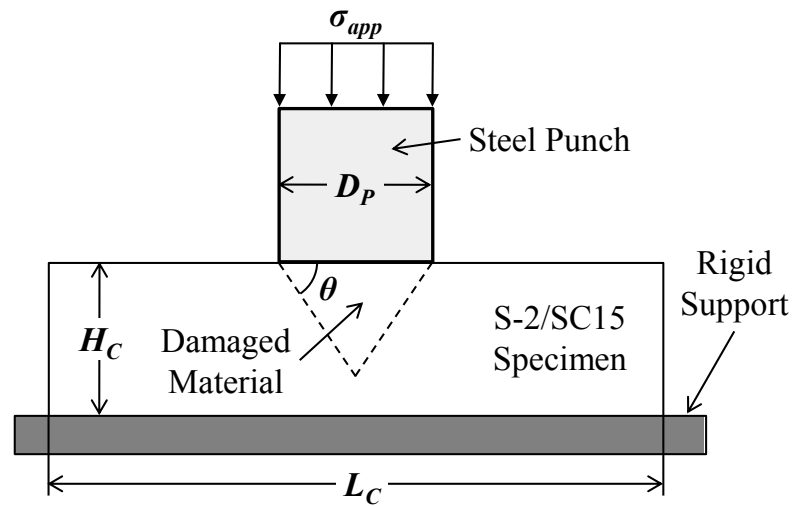


**Figure 5.1 – Parameters in the confined compression problem**

## 5.2 Analytical Form

If a given system has an analytical form which describes the system behavior, the analytical form can be used to suggest parametric scaling ratios. Other methods of deriving parametric ratios exist, such as the Buckingham Pi Theorem (White, 2003, pp 302-304). However, while the Pi Theorem provides all possible parametric combinations for a given system, an analytical form suggests only those combinations which are likely to influence the system.

The analytical form used is a solution of the confined compression problem given by D. Milovic (1992, pp 182-189). The solution gives expressions for the three stress components under plane strain components ( $\sigma_x$ ,  $\sigma_z$ , and  $\tau_{xz}$ ) in terms of the four parameters previously identified ( $D_P$ ,  $H_C$ ,  $L_C$ , and  $\sigma_{app}$ ). The expressions are repeated from Section 2.5:

$$\sigma_z = \frac{\sigma_{-z,p} D}{L} + \sigma_{-z,p} \sum_{m=1}^M \frac{\sin \frac{m\pi}{2L} \left[ 6.05 \times 10^8 \sinh\left(\frac{0.47m\pi}{L}\right) \cosh\left(\frac{3.32m\pi}{L}\right) - 5.74 \times 10^9 \sinh\left(\frac{3.32m\pi}{L}\right) \cosh\left(\frac{0.47m\pi}{L}\right) \right] \cos \frac{m\pi}{L}}{m\pi \left[ 1.51 \times 10^8 \sinh\left(\frac{0.47m\pi}{L}\right) \cosh\left(\frac{3.32m\pi}{L}\right) - 1.44 \times 10^9 \sinh\left(\frac{3.32m\pi}{L}\right) \cosh\left(\frac{0.47m\pi}{L}\right) \right]} \quad (5.1)$$

$$\sigma_r = \frac{0.52\sigma_{-z,p} D}{L} + \sigma_{-z,p} \sum_{m=1}^M \frac{\sin \frac{m\pi}{2L} \left[ 9.05 \times 10^9 \sinh\left(\frac{0.47m\pi}{L}\right) \cosh\left(\frac{3.32m\pi}{L}\right) - 1.02 \times 10^9 \sinh\left(\frac{3.32m\pi}{L}\right) \cosh\left(\frac{0.47m\pi}{L}\right) \right] \cos \frac{m\pi}{L}}{m\pi \left[ 1.51 \times 10^8 \sinh\left(\frac{0.47m\pi}{L}\right) \cosh\left(\frac{3.32m\pi}{L}\right) - 1.44 \times 10^9 \sinh\left(\frac{3.32m\pi}{L}\right) \cosh\left(\frac{0.47m\pi}{L}\right) \right]} \quad (5.2)$$

$$\tau_{rz} = -\sigma_{-z,p} \sum_{m=1}^M \frac{1.25 \sin \frac{m\pi}{2L} \left[ 2.40 \times 10^9 \sinh\left(\frac{0.47m\pi}{L}\right) \cosh\left(\frac{3.32m\pi}{L}\right) - 2.40 \times 10^9 \sinh\left(\frac{3.32m\pi}{L}\right) \cosh\left(\frac{0.47m\pi}{L}\right) \right] \cos \frac{m\pi}{L}}{m\pi \left[ 1.51 \times 10^8 \sinh\left(\frac{0.47m\pi}{L}\right) \cosh\left(\frac{3.32m\pi}{L}\right) - 1.44 \times 10^9 \sinh\left(\frac{3.32m\pi}{L}\right) \cosh\left(\frac{0.47m\pi}{L}\right) \right]} \quad (5.3)$$

Note that the subscripts *C* and *P*, denoting “composite” and “punch” respectively, have been dropped from equations (5.1-5.3) to simplify the presentation. The constants shown represent the material constants present in the analytical form, as discussed in Section 2.5.

Examining equations (5.1-5.3), the analytical form is observed to contain three basic expressions: the applied stress ( $\sigma_{app}$ ), material constants, and geometric ratios of thickness or diameter with specimen width ( $H_C/L_C$  or  $D_P/L_C$ ). In all three equations, the applied stress can be divided through such that the stress components can be expressed as a ratio with the applied stress (i.e.  $\sigma_z/\sigma_{app}$ ). Since only linear-elastic behavior is considered, this result is expected.

### 5.3 A Geometric Scaling Parameter

In Chapter 4 it was demonstrated that there exists a critical specimen width,  $L_C = L_{crit}$ , for which all wider specimens have equivalent stress distributions. Since any specimens with  $L_C < L_{crit}$  are considered invalid in the present study and all specimens with  $L_C > L_{crit}$  are expected to exhibit equivalent behavior, only specimens with  $L_C = L_{crit}$  need to be considered in the analytical form. Therefore  $L_C$  can be set equal to  $L_{crit}$  in equations (5.1-5.3). If the expressions for  $L_{crit}$  in equations (4.3) and (4.4) are substituted into the ratios of  $H_C/L_C$  and  $D_P/L_C$  in equations (5.1-5.3) the following simplifications result:

$$\frac{H_C}{L_{crit}} = \frac{H_C}{0.94D_P + .47H_C} = \left( .94 \frac{D_P}{H_C} + .47 \right) \quad (\text{Thin}) \quad (5.4)$$

$$\frac{H_C}{L_{crit}} = \frac{H_C}{0.37D_P^2/H_C + .11H_C} = \left( .37 \left( \frac{D_P}{H_C} \right)^2 + .11 \right) \quad (\text{Thick}) \quad (5.5)$$

$$\frac{D_P}{L_{crit}} = \frac{D_P}{0.94D_P + .47H_C} = \left( .94 + .47 \frac{H_C}{D_P} \right) \quad (\text{Thin}) \quad (5.6)$$

$$\frac{D_P}{L_{crit}} = \frac{D_P}{0.37D_P^2/H_C + .11H_C} = \left( .37 \frac{D_P}{H_C} + .11 \frac{H_C}{D_P} \right) \quad (\text{Thick}) \quad (5.7)$$

In a similar manner, the expressions for  $z/L_C$  and  $x/L_C$  in equations (5.1-5.3) can be simplified as demonstrated below employing the results of equations (5.4-5.7):

$$\frac{z}{L_{crit}} = \frac{z}{H_C} \cdot \frac{H_C}{L_{crit}} = \frac{z}{H_C} \left( .94 \frac{D_P}{H_C} + .47 \right) \quad (\text{Thin}) \quad (5.8)$$

$$\frac{z}{L_{crit}} = \frac{z}{H_C} \cdot \frac{H_C}{L_{crit}} = \frac{z}{H_C} \left( .37 \left( \frac{D_P}{H_C} \right)^2 + .11 \right) \quad (\text{Thick}) \quad (5.9)$$

$$\frac{x}{L_{crit}} = \frac{x}{D_P} \cdot \frac{D_P}{L_{crit}} = \frac{x}{D_P} \left( .94 + .47 \frac{H_C}{D_P} \right) \quad (\text{Thin}) \quad (5.10)$$

$$\frac{x}{L_{crit}} = \frac{x}{D_P} \cdot \frac{D_P}{L_{crit}} = \frac{x}{D_P} \left( .37 \frac{D_P}{H_C} + .11 \frac{H_C}{D_P} \right) \quad (\text{Thick}) \quad (5.11)$$

Equations (5.4-5.11) demonstrate that the analytical form can be simplified in terms of three dimensionless geometric ratios. The first is the ratio  $D_P/H_C$  (or its inverse), described as a “relative thickness” parameter. The second and third are the coordinate scaling parameters  $z/H_C$  and  $x/D_P$ , which normalize each coordinate to the defining geometric parameter in its respective axes. Thus, if two specimen setups have different physical dimensions but share the aspect ratio  $D_P/H_C$  they will have equivalent stress distributions in a scaled geometric space.

#### 5.4 Numerical Validation

A numerical validation of this geometric scaling for the experimental setup is shown in Figures 5.2 and 5.3 for specimens with  $D_P/H_C = 0.909$ . Slight discrepancies in the stress distributions at the punch periphery are noted. These are attributed to the use of a chamfer on the punch. A 0.25-mm chamfer was used in all numerical punches to mimic the experimental setup as discussed in Section 2.4. For smaller specimens (i.e. the  $D_P = 6.35\text{-mm}/H_C = 6.99\text{-mm}$  sample in Figures 5.2 and 5.3) this chamfer has a greater effect than for larger specimens (i.e. the  $D_P = 12.70\text{-mm}/H_C = 13.97\text{-mm}$  and  $D_P = 19.05\text{-mm}/H_C = 20.96\text{-mm}$  samples in Figures 5.2 and 5.3) since the point of contact is further from the punch periphery. Thus the applied stress concentration (Figure 5.3) is further from the punch periphery (i.e.  $x/D_P = 0.5$ ) for the smaller specimen than the larger specimen. This effect reduces the shear stresses measured at the actual punch periphery, as seen in Figure 5.2. Moreover, it is noted that as the chamfer radius,  $r_C$ , decreases relative to the punch diameter (i.e.  $r_C/D_P \rightarrow 0$ ), the stress distributions become convergent. This is illustrated by the  $D_P = 12.70\text{-mm}/H_C = 13.97\text{-mm}$  and  $D_P = 19.05\text{-mm}/H_C = 20.96\text{-mm}$  combinations in Figures 5.2 and 5.3. Recalling that  $r_C = 0.254\text{-mm}$  for the numerical punches, this

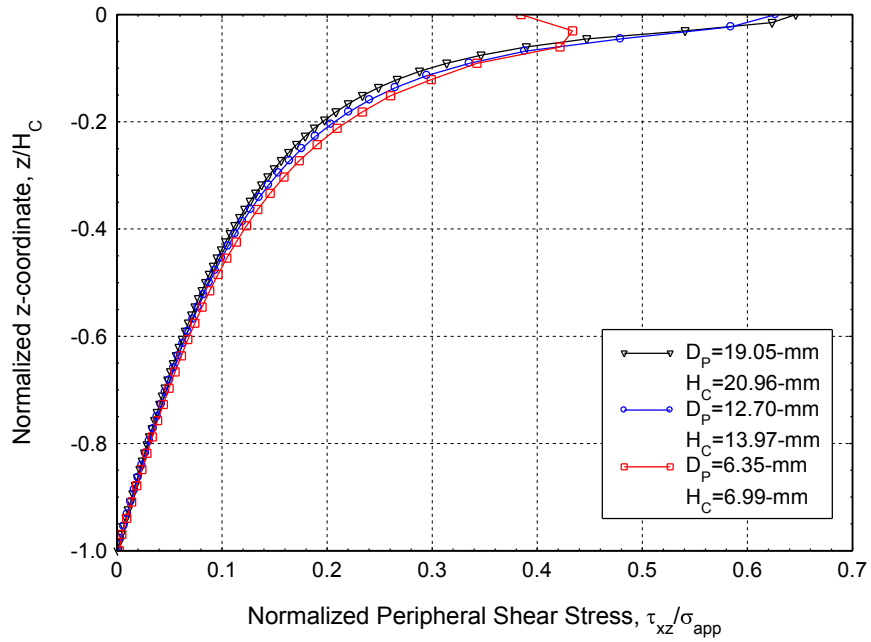


Figure 5.2 – Comparison of shear stress at periphery for  $D_p/H_C = 0.909$

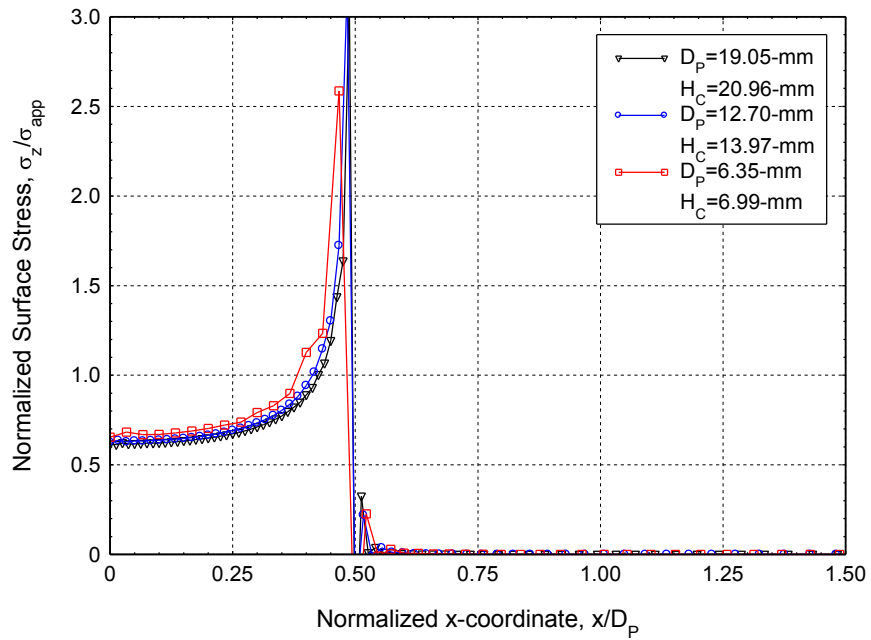


Figure 5.3 – Comparison of normal stress on surface for  $D_p/H_C = 0.909$

observation suggests that a ratio of  $r_C/D_P \leq 0.02$  would give convergence for equal values of  $D_P/H_C$  in the present study. It is also noted that the stress distributions in Figure 5.3 are essentially equivalent except for this minor discrepancy, and that the stress distributions in Figure 5.2 agree except for the discrepancy explained here.

Two numerical models without punch chamfers were created to explore the effects of chamfering on scaling by  $D_P/H_C$ . The through-thickness stress distribution and surface normal stress distribution are shown for these models in Figures 5.4 and 5.5, respectively. The scaled stress distributions in Figures 5.4 and 5.5 show significantly improved agreement when compared with Figures 5.2 and 5.3. The maximum error between the two scaled curves is 5% in Figure 5.4, and may be attributed to slight meshing differences at the punch periphery. Figures 5.4 and 5.5 suggest that geometric scaling by  $D_P/H_C$  is valid for the elastic punch loading when the value of  $D_P/H_C$  measured at the contact between the punch and specimen is constant. The introduction of a chamfer, however, only approximates a constant value of  $D_P/H_C$ , leading to discrepancies. The sensitivity of the stress singularities to the meshing at the point of contact also introduces discrepancies.

## 5.5 Experimental Comparisons

The values of  $D_P/H_C$  for the punch-specimen combinations in the experimental test matrix are shown in Table 5.1. Geometrically similar specimens within a 2% error are noted in boldface with superscripts. Recognizing that the two experimental measures,  $\theta$  and  $\sigma_{app}$ , have already been shown to have characteristic values for all punch diameters and specimen thicknesses (Chapter 3), the experimental results alone cannot be used to demonstrate the effectiveness of scaling by  $D_P/H_C$ .

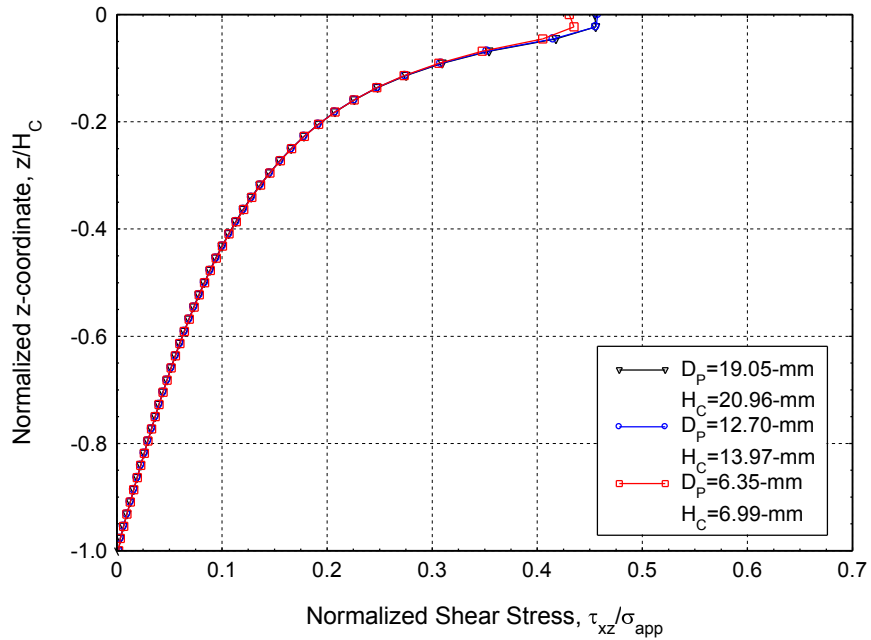


Figure 5.4 – Comparison of shear stress for  $D_p/H_C = 0.909$  with no chamfer

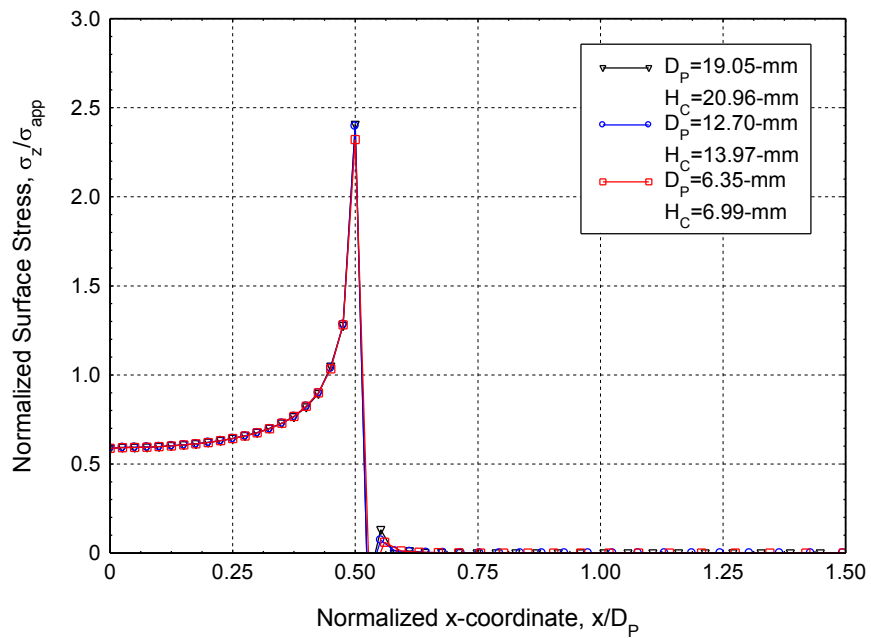


Figure 5.5 – Comparison of normal stress for  $D_p/H_C = 0.909$  with no chamfer

**Table 5.1 – Experimental test matrix with geometric ratios of  $D_p/H_C$**

		<u>Punch Diameter, <math>D_p</math>, mm</u>					
		<b>6.27</b>	<b>7.62</b>	<b>7.92</b>	<b>10.16</b>	<b>11.09</b>	<b>12.70</b>
<u>Specimen Thickness, <math>H_C</math>, mm</u>	<b>20.83</b>	---	0.37	---	0.49	---	0.61
	<b>13.72</b>	---	0.56	---	0.74	---	0.93
	<b>7.62</b>	0.82	---	1.04	---	<b>1.46<sup>b</sup></b>	<b>1.67<sup>c</sup></b>
	<b>7.11</b>	---	1.07	---	<b>1.43<sup>b</sup></b>	---	1.79
	<b>6.35</b>	0.99	---	<b>1.25<sup>a</sup></b>	---	1.75	2.00
	<b>5.08</b>	<b>1.24<sup>a</sup></b>	---	1.56	---	2.18	<b>2.50<sup>d</sup></b>
	<b>3.81</b>	<b>1.65<sup>c</sup></b>	---	2.08	---	2.91	3.33
	<b>2.54</b>	<b>2.47<sup>d</sup></b>	---	3.12	---	4.37	5.00

**Note:** Superscripts <sup>a, b, etc.</sup> represent similar values of  $D_p/H_C$

## 5.6 Chapter Summary

The present chapter examined the parameters present in the analytical model of the confined compression setup. Four parameters were identified in the analytical form: applied stress, punch diameter, specimen thickness, and specimen width. It was demonstrated that all three stress components can be normalized by the applied stress. Recalling the definition of critical width from Chapter 4, it was demonstrated that a geometric scaling parameter  $D_p/H_C$  can be used for all  $L > L_{crit}$ . The numerical model was used to show that punch-specimen pairs with equal values of  $D_p/H_C$  have similar stress distributions, though the effects of the punch chamfer prevented direct equality. However, it was shown that as the ratio of the chamfer to the punch diameter decreases the validity of  $D_p/H_C$  scaling increases. Likewise, punch-specimen pairs with no punch chamfer demonstrated equivalent behavior when the ratio  $D_p/H_C$  was constant. Chapter 6 will explore the behavior of the peak stress distributions to explain why punch-specimen pairs with different values of  $D_p/H_C$  exhibit similar applied stress values at failure.

## Chapter 6

### STRESS STATE AT FAILURE

In Chapter 3 it was seen that the experimental fracture angle and applied stress at failure both appeared to have characteristic values regardless of variations in specimen geometry. A basic force-balance analysis on the specimen showed that compressive reactions dominated for thinner specimens while shear reactions dominated for thicker specimens. It was concluded that the experimental behavior contradicted the variable behavior expected from these changes in the internal stresses. In the present chapter the internal stress distribution will be considered in more depth and used to evaluate a number of common failure criteria to explain the apparent contradiction in experimental behavior.

#### 6.1 Internal Stress Distribution

The internal stress distributions for representative thin and thick specimens are shown in Figure 6.1. Only the components  $\sigma_x$ ,  $\sigma_z$ , and  $\tau_{xz}$  are shown since the circumferential components are significantly smaller at the point of damage initiation. Some characteristics of the stress behavior are noted. For the thin specimen, a state of nearly uniform compression in the  $z$ -direction exists beneath the punch through the entire thickness. However, the stress is concentrated at the punch periphery at the specimen surface for the thick specimen. The axial and shear stress components ( $\sigma_x$  and  $\tau_{xz}$ ) exhibit concentrated stresses at the punch periphery at the specimen surface for both thin and thick specimens. A comparison of the stress

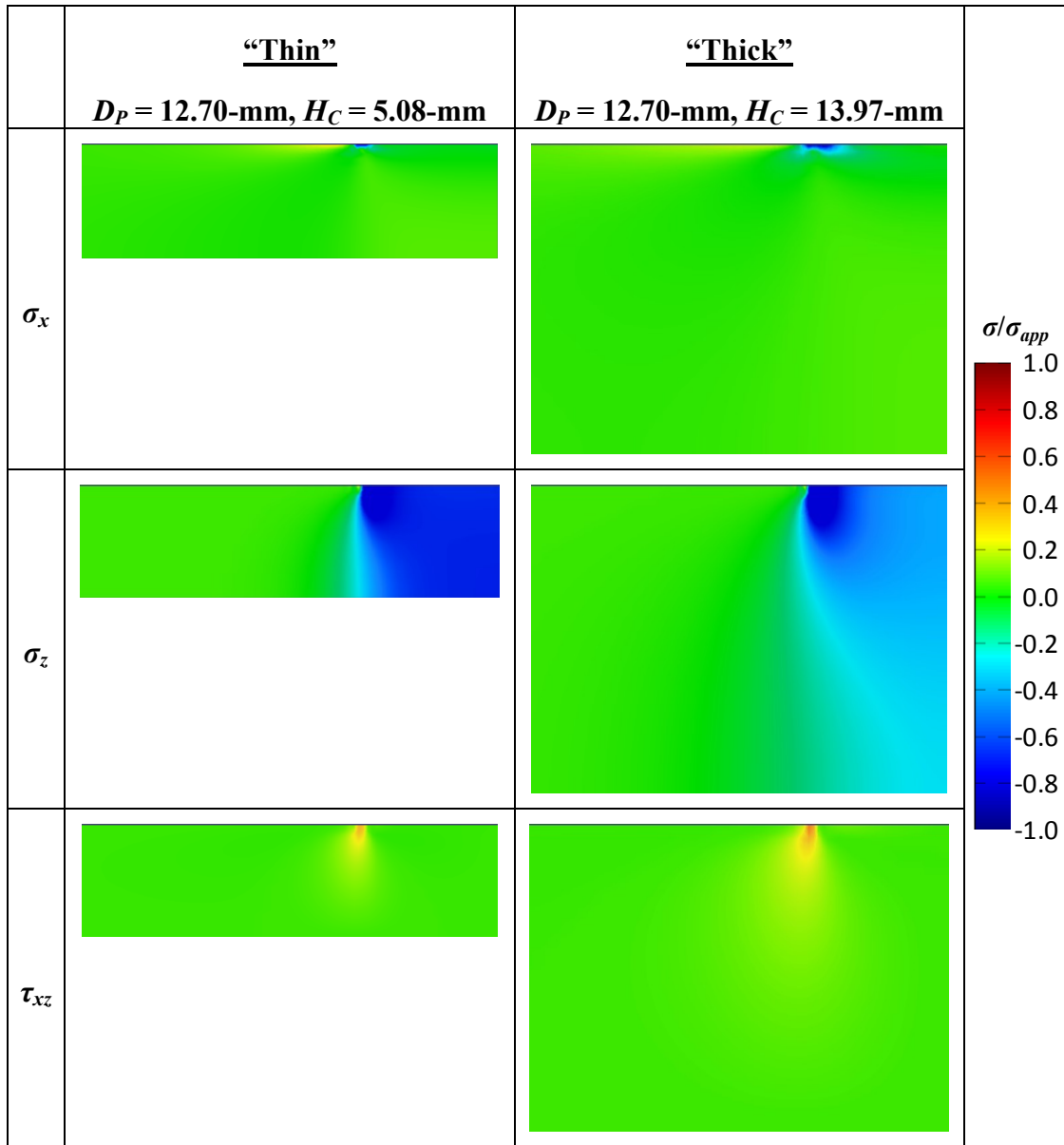
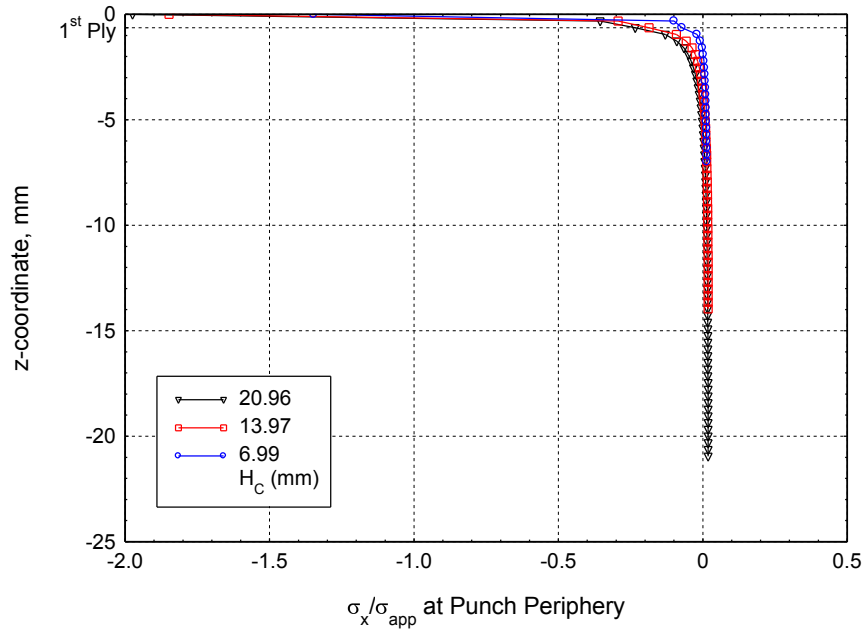


Figure 6.1 – Comparison of “thin” and “thick” stress distributions

distributions for  $\sigma_x$  and  $\tau_{xz}$  in Figure 6.1 suggests that the magnitude of the concentration is indeed more significant for the thicker specimen since a uniform distribution, as observed for thinner specimens, tends to lessen the magnitude of the concentrated stresses.

For both thin and thick specimens within the range of geometries considered the point of maximum stresses in the material axes occurs at the punch periphery in the fiber direction. This is the point at which failure would be expected to initiate, and hence the stresses at this point are of interest. Recalling that the internal stress components can be normalized by the applied stress if linear-elastic behavior is assumed (Section 5.2), stress components are represented by  $\alpha = \sigma/\sigma_{app}$ , where  $\alpha$  is the “normalized stress” and a negative value of  $\alpha$  indicates compression. The stress components can then be calculated for any applied stress as  $\sigma = \alpha \times \sigma_{app}$ . Conversely, since the material strengths ( $\sigma = S$ ) are known from Table 2.1, the applied stress to cause failure can be predicted by calculating  $\sigma_{app} = S/\alpha$ .

Figures 6.2-6.7 show the numerically calculated through-thickness stress distributions for each stress component at the punch periphery in the fiber direction for a 12.70-mm punch. It is observed that significant stress gradients exist in the top ply for all the normal stress components ( $\sigma_x$ ,  $\sigma_y$ , and  $\sigma_z$ ) and the in-plane shear stress component ( $\tau_{xy}$ ) (Figures 6.2-6.5). It should be noted that material strengths are measured at the macroscopic level, typically using specimens with a thickness greater than a single ply which are subjected to uniform stress and strain conditions. Consequently, it is necessary for the internal stress distributions to have no significant stress gradients over distances below the macroscopic level when using strength-based failure criteria. For consistency with the known failure strengths in cases of a



**Figure 6.2 – Transverse stress in the x-direction (12.70-mm punch)**

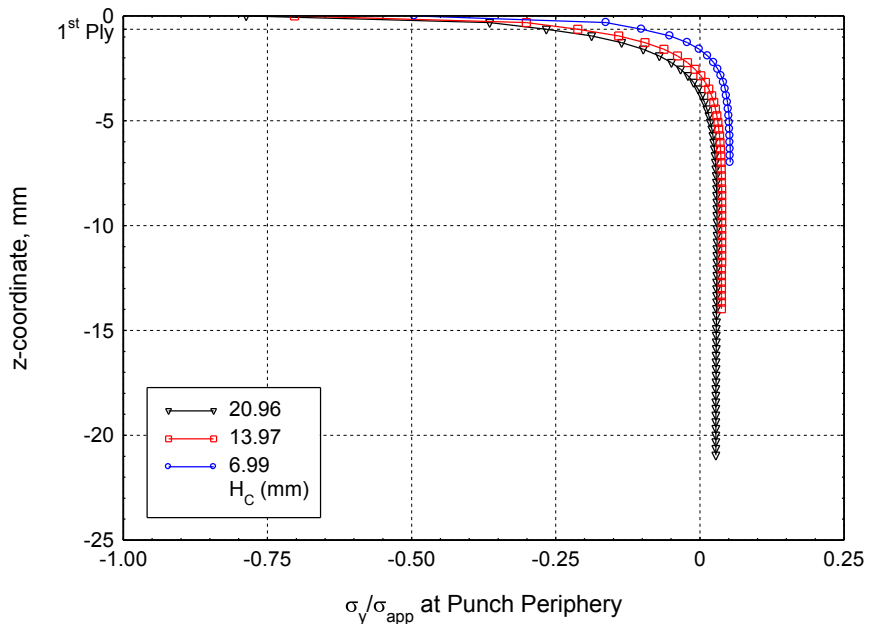


**Figure 6.3 – Transverse stress in the y-direction (12.70-mm punch)**

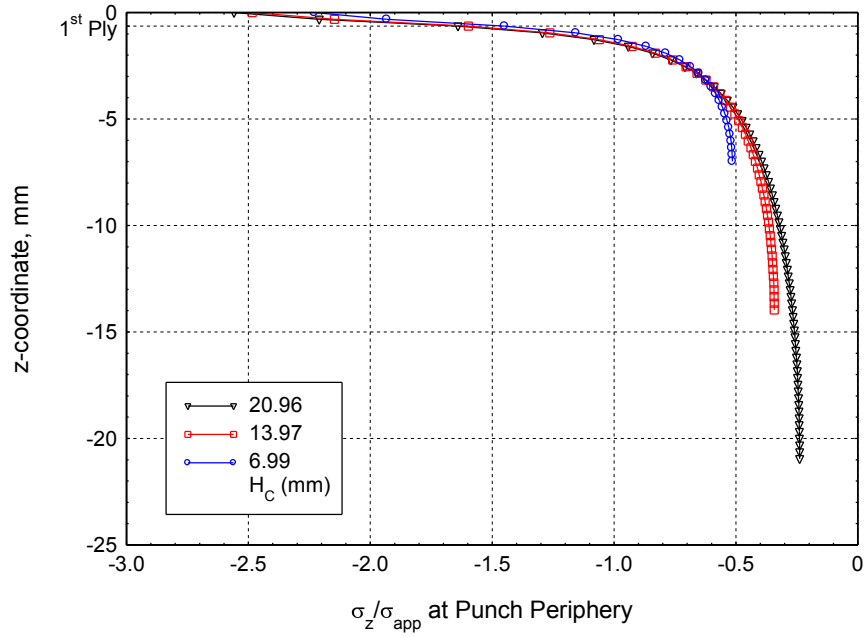


**Figure 6.4 – Through-thickness stress in the  $z$ -direction (12.70-mm punch)**

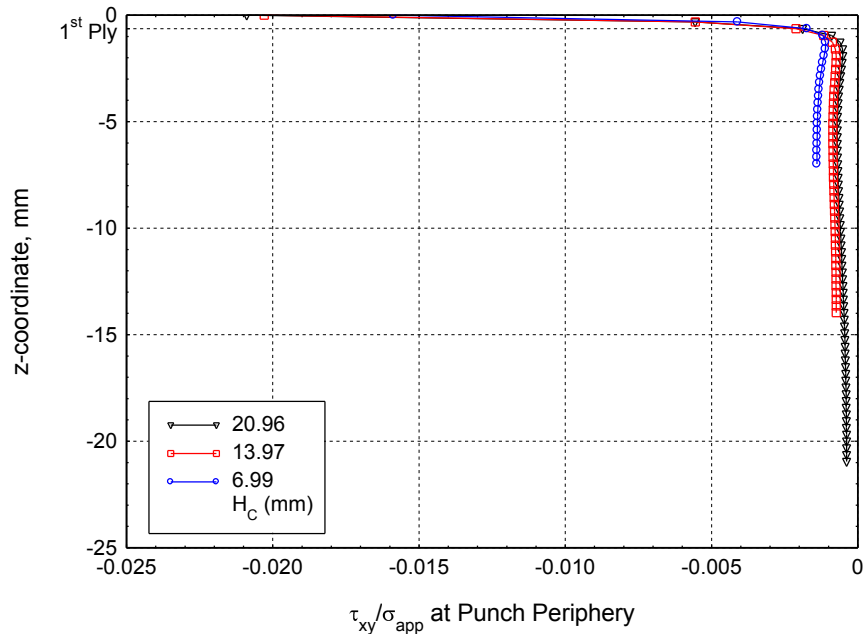


**Figure 6.5 – Shear stress on the  $xy$ -plane (12.70-mm punch)**

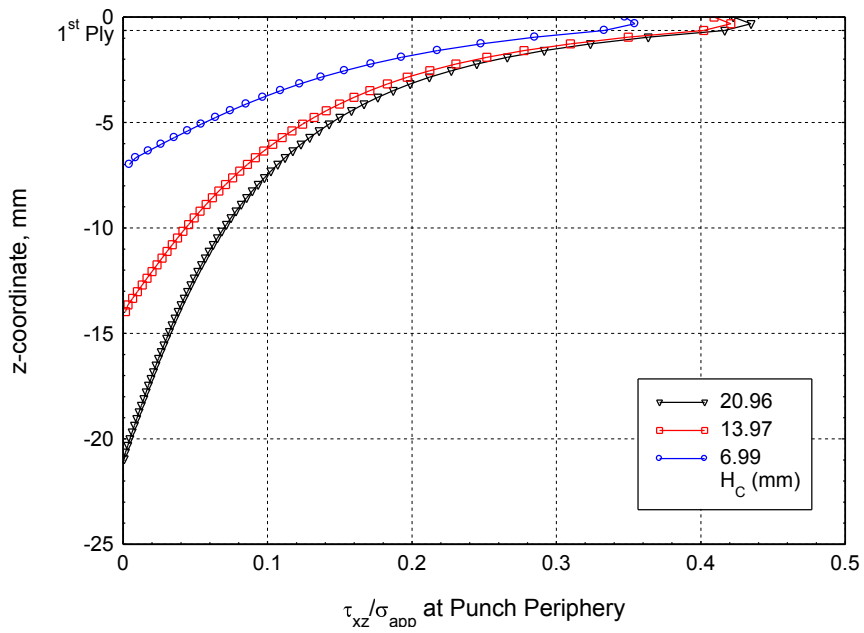


**Figure 6.6 – Shear stress on the  $xz$ -plane (12.70-mm punch)**

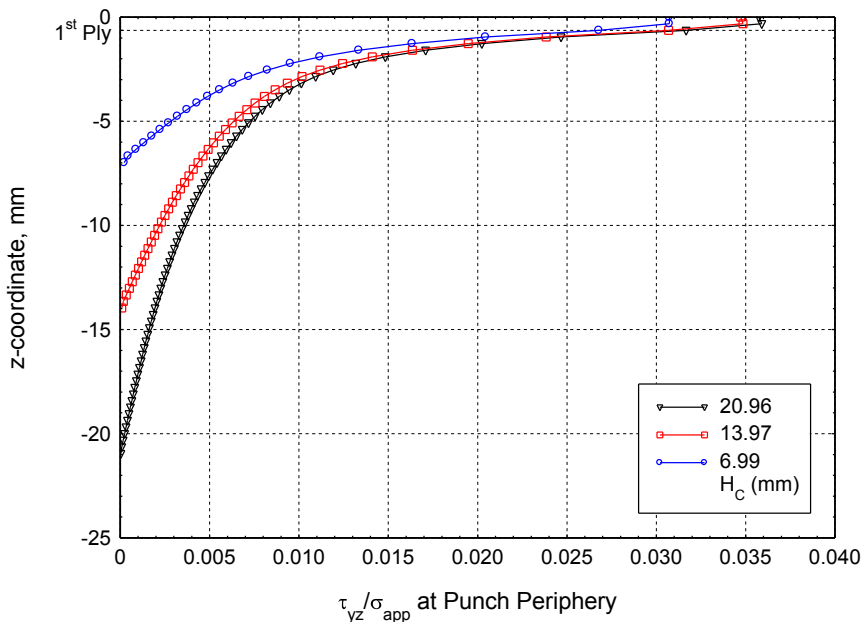


**Figure 6.7 – Shear stress on the  $yz$ -plane (12.70-mm punch)**

significant stress gradient, the maximum stress in the first ply is approximated by the average value of the stress distribution within the first ply. A similar method was proposed by Whitney and Nuismer for stress concentrations caused by holes and cracks (1974). For the S-2/SC15 composite, the thickness of a single ply is taken to be 0.635-mm. The values of the stress components averaged over the top ply are given in Table 6.1. These values are also plotted as a function of  $D_P$  and  $H_C$  in Figures 6.8 and 6.9, respectively. It should be noted that tensile stresses are positive while compressive stresses are negative.

Figures 6.8 and 6.9 provide additional insights into the internal stress behavior shown in Figure 6.1. It is noted that the circumferential stress components ( $\sigma_y$ ,  $\tau_{xy}$ , and  $\tau_{yz}$ ) are smaller than the radial stress components ( $\sigma_x$ ,  $\sigma_z$ , and  $\tau_{xz}$ ). Figure 6.9 suggests that as the specimen becomes thinner the maximum magnitude of all of the stress components decreases. As noted above, this behavior is expected as the stress distribution becomes more uniform. The maximum stresses in Figure 6.8 appear to remain almost constant or increase slightly as punch diameter increases. Increasing punch diameter, which has the effect of making the punch-specimen pair “thinner”, would be expected to cause the stresses to decrease, which is not observed in Figure 6.8. For punches with smaller diameters, this discrepancy is attributed to the punch chamfer which tends to decrease the values of the stress components (see Section 5.4). A slightly smaller range of “relative thicknesses” as measured by the ratio  $D_P/H_C$  may also explain the more uniform behavior shown in Figure 6.8 and subsequent plots which are a function of punch diameter. Figure 6.8 includes punch-specimen pairs in the range  $0.91 \leq D_P/H_C \leq 2.73$ , while Figure 6.9 includes punch-specimen pairs in the range  $0.61 \leq D_P/H_C \leq 5.00$ .

**Table 6.1 – Normalized average stresses at punch periphery in the fiber direction**

$D_P$ <i>mm</i>	$H_C$ <i>mm</i>	<b>Normalized Stress Components (<math>\alpha = \sigma/\sigma_{app}</math>)</b>					
		$\alpha_x$ ---	$\alpha_y$ ---	$\alpha_z$ ---	$\alpha_{xy}$ ---	$\alpha_{xz}$ ---	$\alpha_{yz}$ ---
<b>6.35<sup>a</sup></b>	<b>2.54<sup>a</sup></b>	<b>-0.200</b>	<b>-0.195</b>	<b>-1.616</b>	<b>-0.006</b>	<b>0.348</b>	<b>0.059</b>
<b>6.35<sup>b</sup></b>	<b>6.99<sup>b</sup></b>	<b>-0.420</b>	<b>-0.398</b>	<b>-1.706</b>	<b>-0.009</b>	<b>0.406</b>	<b>0.012</b>
7.62	6.99	-0.437	-0.414	-2.000	-0.007	0.476	0.080
10.16	2.54	-0.165	-0.189	-1.692	-0.004	0.347	0.065
10.16	6.99	-0.450	-0.426	-1.955	-0.011	0.470	0.027
10.16	13.97	-0.651	-0.563	-2.109	-0.013	0.531	0.030
10.16	20.96	-0.711	-0.615	-2.149	-0.013	0.544	0.031
11.43	6.99	-0.494	-0.424	-1.996	-0.012	0.489	0.026
12.70	2.54	-0.127	-0.219	-1.495	0.012	0.288	-0.013
12.70	3.81	-0.252	-0.270	-1.739	-0.010	0.392	0.021
<b>12.70<sup>a</sup></b>	<b>5.08<sup>a</sup></b>	<b>-0.355</b>	<b>-0.337</b>	<b>-1.888</b>	<b>-0.011</b>	<b>0.445</b>	<b>0.024</b>
12.70	6.99	-0.461	-0.418	-2.044	-0.012	0.495	0.026
<b>12.70<sup>b</sup></b>	<b>13.97<sup>b</sup></b>	<b>-0.705</b>	<b>-0.596</b>	<b>-2.277</b>	<b>-0.013</b>	<b>0.569</b>	<b>0.029</b>
12.70	20.96	-0.776	-0.656	-2.179	0.011	0.522	-0.063
15.24	6.99	-0.488	-0.413	-2.059	-0.011	0.500	-0.027
19.05	6.99	-0.477	-0.406	-2.117	0.013	0.511	-0.036
<b>19.05<sup>b</sup></b>	<b>20.96<sup>b</sup></b>	<b>-0.950</b>	<b>-0.698</b>	<b>-2.412</b>	<b>0.0225</b>	<b>0.608</b>	<b>-0.138</b>

**Note:** Superscripts <sup>a</sup> and <sup>b</sup> indicate geometrically similar specimens with  $D_P/H_C$  ratios of 2.50 and 0.91, respectively

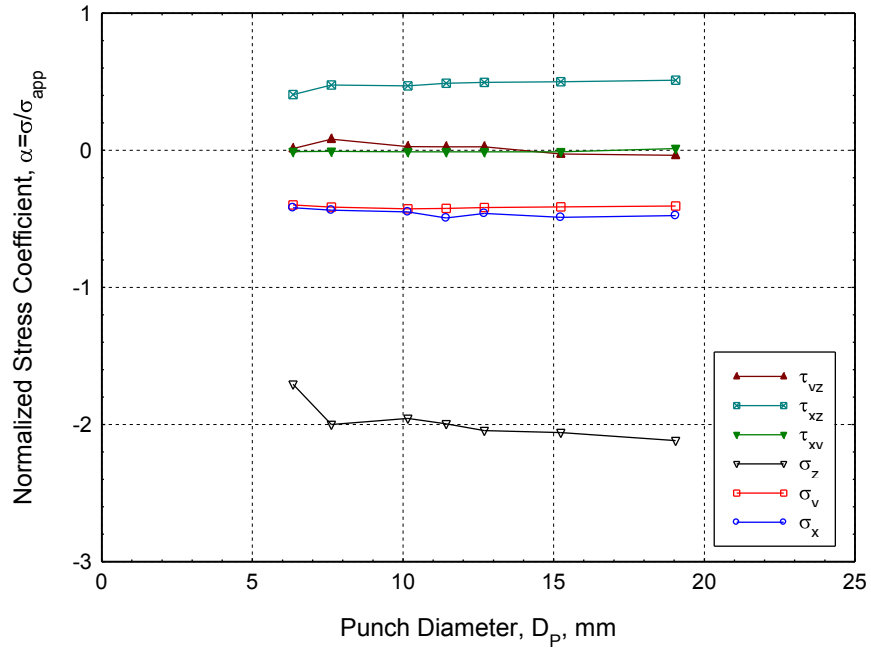


Figure 6.8 – Average stress components  $\alpha$  as a function of  $D_p$  (6.99-mm sample)

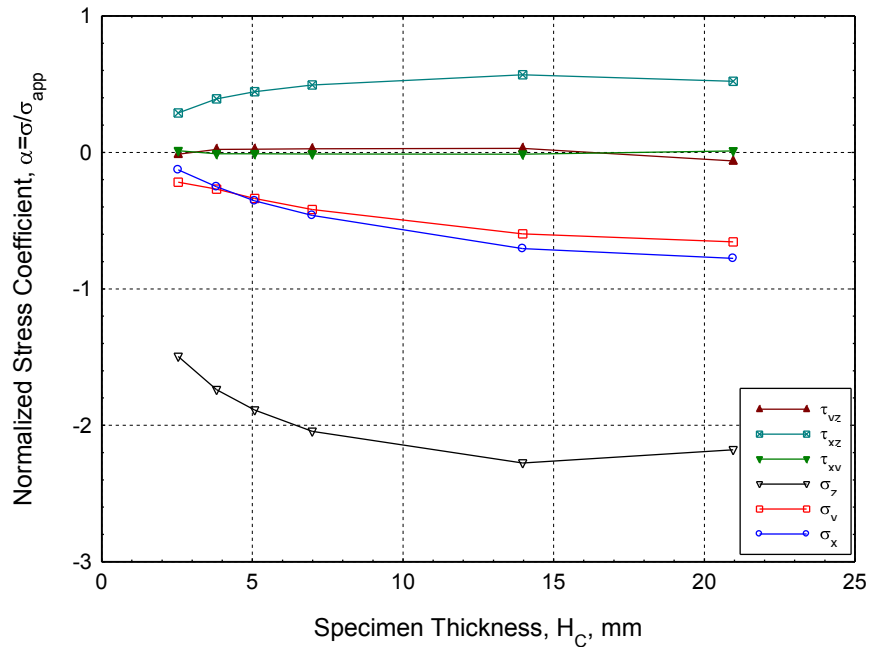


Figure 6.9 – Average stress components  $\alpha$  as a function of  $H_c$  (12.70-mm punch)

The observation of similar behaviors with varying punch-specimen geometries for all stress components is significant for understanding the behavior of confined compression specimens. While the global specimen-level stress distributions (Section 3.2 and Figure 6.1) exhibit a significant change from compression-dominated behavior to shear-dominated behavior, it is possible that the localized stresses at the point of failure are self-equilibrating for all geometries and lead to the characteristic value of applied stress at failure observed experimentally. The next section will consider common failure criteria to mathematically capture this behavior.

It should be noted that discrepancies exist in the values of  $\alpha$  for specimens with equivalent geometric ratios  $D_p/H_C$  as shown in Table 6.1 ( $D_p/H_C = 0.91$  and  $D_p/H_C = 2.51$ ). These discrepancies are attributed to two sources. The first is the effect of the punch chamfer discussed in Section 5.4. The second is the decision to average the stress gradients over the thickness of the first ply. For thinner specimens, this will average a greater portion of the through-thickness stress distribution, leading to a lower calculated value of the average stress component. Comparison of values for the geometrically similar specimens in Table 6.1 (indicated in boldface) shows that this effect is seen.

### **6.1.1 Comments on Fiber Shear Strength**

It was mentioned above that material strengths are typically measured from macroscopic specimens with uniform stress and strain. The fiber shear strength ( $T_F$ ) given in Table 2.1 was measured using a punch shear test with a support span to punch diameter ratio of  $D_S/D_P \approx 1.1$  (Xiao, Gama, & Gillespie, 2007). This test methodology forces the specimen to fail under fiber shear with the shear strength taken as the average shear stress through the thickness:

$$\tau_{vg} = \frac{P_{max}}{\pi_p H_C} \quad (6.1)$$

To investigate if a state of uniform stress exists during punch shear testing, a finite element model was created in CATIA, using a similar methodology to that described in Section 2.4. It was observed that stress concentrations for the shear stress component ( $\tau_{xz}$ ) exist at the top of the specimen. Because stress concentrations exist in the punch shear test,  $\tau_{avg}$  is not an appropriate measure of the true fiber shear strength  $T_F$ , since the failure of the fibers is governed by a strength greater than  $\tau_{avg}$ . Thus, the fiber shear strength should be calculated based on the concentrated shear stresses.

Experimental measurements of  $\tau_{avg}$  for a range of punch-specimen combinations are shown in Figure 6.10 as a function of  $D_p/H_C$ . The values are taken from experimentation as well as an unpublished paper by Gama et al. (2006). It is observed that the value of  $\tau_{avg}$  increases as thickness decreases (i.e. as  $D_p/H_C \rightarrow \infty$ ) due to the diminishing concentration of the shear stress for thinner specimens. The values of the shear stress concentrations normalized by the average applied shear stress ( $\tau_{avg}$ ) are shown in Figure 6.11, also as a function of  $D_p/H_C$ . To obtain valid macroscopic values of the stress concentration, the shear stress distribution was averaged over the top ply of the specimen, as described above. It is observed that the stress concentration decreases as thickness decreases (i.e. as  $D_p/H_C \rightarrow \infty$ ), with a limiting value of  $\tau_{avg}$  for very thin specimens.

Knowing the value of the stress concentration as normalized by the average stress (i.e.  $\tau_{xz}/\tau_{avg}$ ) from Figure 6.11, the experimental value of the stress concentration can be estimated by multiplying the normalized stress concentration and the experimentally measured average stress. A trend line is fit through the data in Figure 6.11 to permit interpolation between the data points, recognizing that  $\tau_{xz} \rightarrow \tau_{avg}$

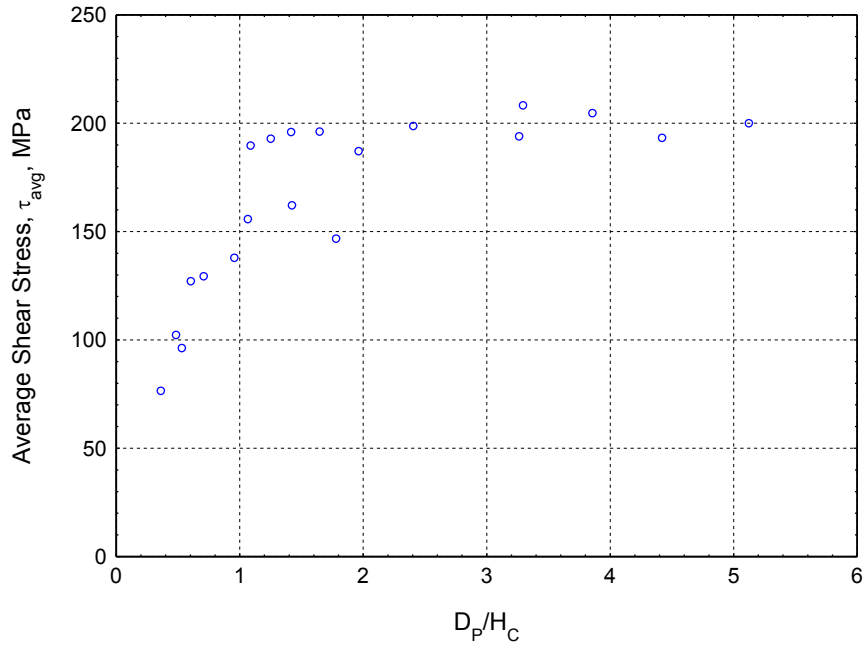


**Figure 6.10 – Experimental values of average shear stress**

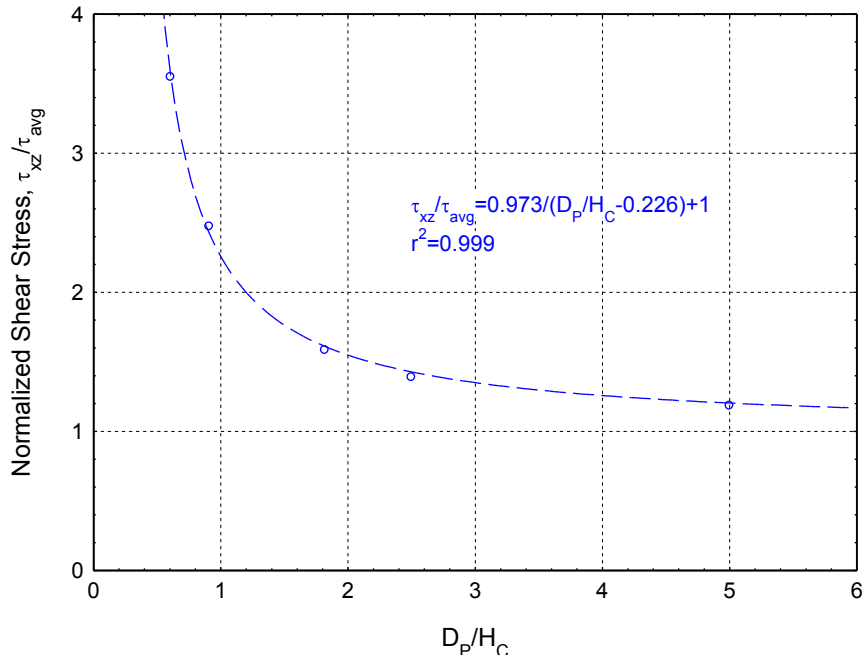


**Figure 6.11 – Numerical values of concentrated normalized shear stress**

as  $D_p/H_C \rightarrow \infty$ . This trend line suggests the following relationship between  $\tau_{xz}$  and  $\tau_{avg}$  within the geometric range of the numerical models ( $0.61 \leq D_p/H_C \leq 5.00$ ):

$$\tau_{xz} = \tau_{avg} \left( \frac{0.973}{D_p/H_C - 0.226} + 1 \right) \quad (6.2)$$

Using equation (6.2), the predicted experimental stress concentrations are presented in Figure 6.12. It is observed that the data in Figure 6.12 have an average value of  $\tau_{xz} = 270$  MPa, with a standard deviation of 31 MPa. In the following analysis of various failure criteria, this corrected value of  $T_F = 270$  will be used for the fiber shear strength in place of the value shown in Table 2.1.

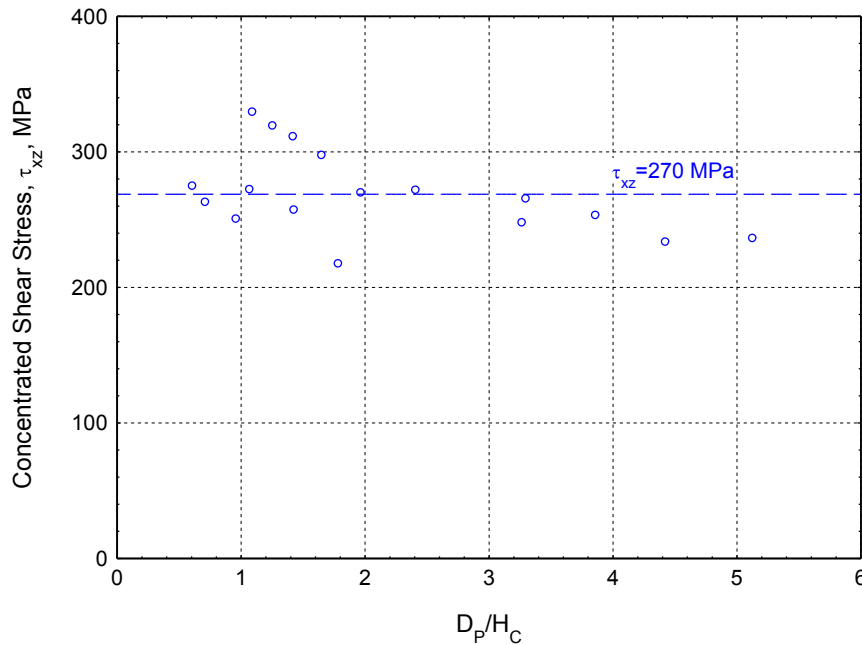


**Figure 6.12 – Calculated values of experimental concentrated shear stress**

## 6.2 Comparison of Failure Criteria

A large number of criteria have been developed to characterize the failure of composite materials (Vinson & Sierakowski, 2002, pp 309-315). Five failure criteria are considered here: the maximum stress criterion, the Tsai-Hill interactive criterion, the Tsai-Wu interactive criterion, a hydrostatic crushing criterion, and a maximum stress criterion based on the deviator stress. It should be noted that in the following discussion a contracted notation may be used in which the subscripts  $i$  and  $j$  are to be replaced with  $x$ ,  $y$ ,  $z$ ,  $xy$ ,  $xz$ , or  $yz$  to represent the stress component of interest.

Evaluation of each failure criterion using the material strengths given in Table 2.1 and the normalized stress coefficients given in Table 6.1 yields a failure coefficient,  $f$ . Failure is defined as occurring when  $f = 1$ . By varying the applied stress in the system using the normalized stress coefficients ( $\alpha$ 's), the applied stress to cause failure for a given criterion (i.e. to cause  $f = 1$ ) can be determined. This applied stress to cause failure is notated as  $\sigma_{fail}$ . The ratio of  $\sigma_{fail}$  to the experimental value of  $\sigma_{avg} = 887$  MPa is defined as the predicted factor of safety  $F$  given by the failure criterion for a specific punch-specimen pair. A value of  $F > 1$  indicates that the specimen is predicted to fail at an applied stress value greater than the experimentally measured value of applied stress at failure ( $\sigma_{avg}$ ) and would not be expected to fail experimentally. A value of  $F < 1$  indicates that the specimen is predicted to fail at an applied stress value lower than the experimentally measured value of applied stress at failure and would be expected to fail earlier than observed. It is desirable to find a failure criteria for which  $F = 1$  regardless of punch-specimen geometry, suggesting that failure should occur when the applied stress is equal to the experimentally measured value.

### 6.2.1 Maximum Stress Criterion

The maximum stress criterion is the simplest of those considered here. Failure is assumed to occur when any one stress component is greater than or equal to the material strength in that direction. This can be represented mathematically as:

$$\frac{\sigma_i}{S_i} = f_i \quad (6.3)$$

where  $S_i$  is the material strength in the  $i$  direction (see Table 2.1), accounting for whether the stress  $\sigma_i$  is in compression or tension. The factors of safety  $F_i$  are displayed in Figures 6.13 and 6.14. It is observed that failure is almost always predicted below the experimental value of applied stress for the through-thickness normal stress  $\sigma_z$  and radial through-thickness shear,  $\tau_{xz}$ . Figure 6.14 shows that the transverse normal stress components  $\sigma_x$  and  $\sigma_y$  fail prematurely for thicker specimens but are not predicted to fail for thinner specimens. The circumferential and in-plane shear components  $\tau_{xy}$  and  $\tau_{yz}$  have factors of safety significantly greater than  $F = 1$  and are not shown in Figures 6.13 and 6.14. Both  $\tau_{xy}$  and  $\tau_{yz}$  are not predicted to fail below the experimental applied stress within the range tested. It is also seen that the through-thickness normal stress controls failure by the maximum stress criterion, since it has the smallest factor of safety.

The maximum stress criterion reflects many of the geometric trends noted in Section 6.1. Figure 6.14 shows that as the specimens become thicker the stress concentrations become more significant, leading to a smaller factor of safety. Likewise, increasing the punch diameter is expected to increase the factor of safety as the stress concentrations decrease. If chamfering effects are accounted for, a weak increasing trend is noted in Figure 6.13. Because each stress component is evaluated individually, the maximum stress criterion is unable to capture the stress interactions

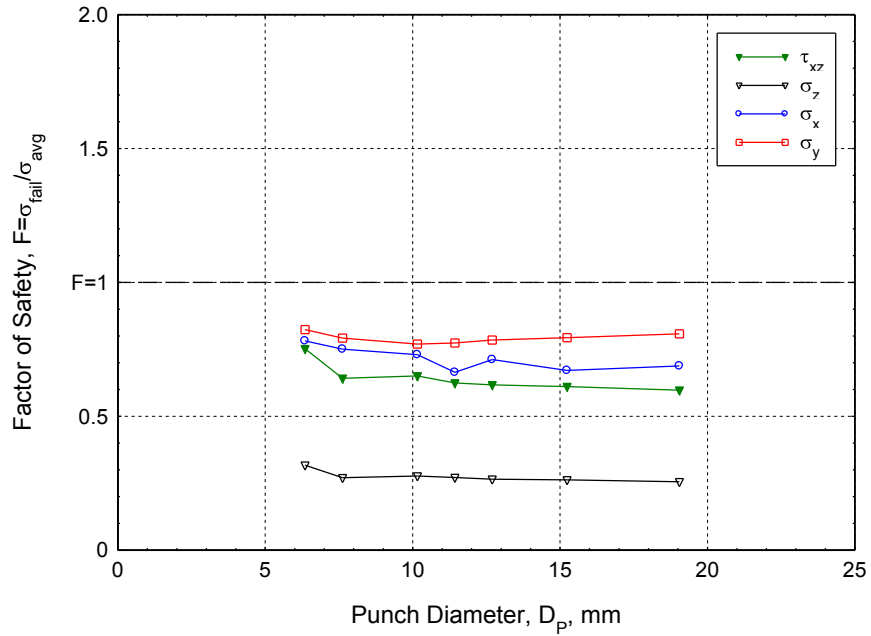


Figure 6.13 – Maximum stress criterion as a function of  $D_p$  (6.99-mm sample)

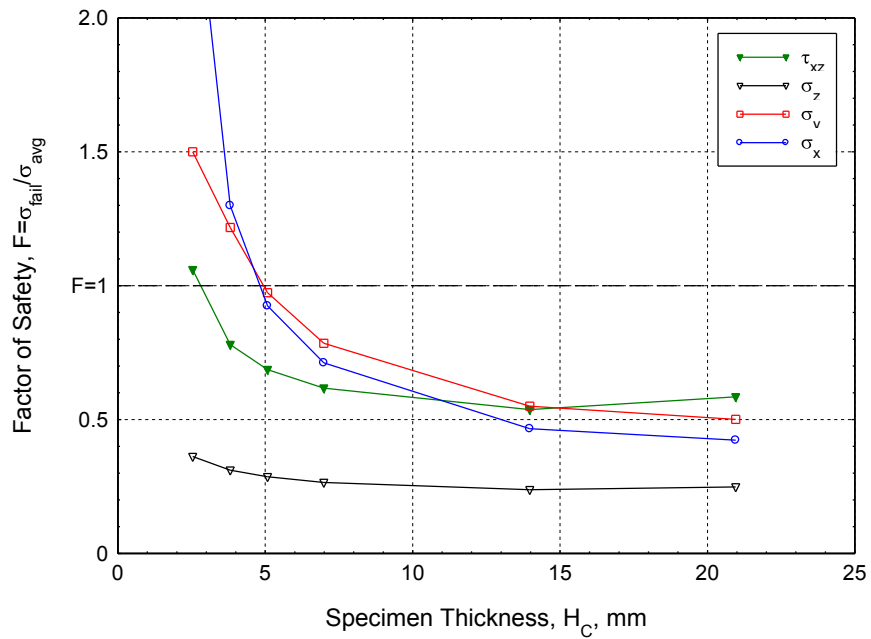


Figure 6.14 – Maximum stress criterion as a function of  $H_c$  (12.70-mm punch)

that may be influencing the failure behavior of the confined compression specimens. Thus the maximum stress criterion is found to be too simplistic for the present study.

### 6.2.2 Tsai-Hill Criterion

Interactive criteria assume that failure initiates due to a combined stress state, not an individual stress component. The Tsai-Hill failure criterion is one of the most basic interactive stress criteria for anisotropic materials such as composites. The failure coefficient is given by the following equation (Hill, 1948, p 285):

$$F(\sigma_x - \sigma_y)^2 + G(\sigma_x - \sigma_z)^2 + H(\sigma_y - \sigma_z)^2 + 2L\tau_{yz} + 2M\tau_{xz} + 2N\tau_{xy} = f \quad (6.4)$$

where the coefficients  $F$ ,  $G$ ,  $H$ ,  $L$ ,  $M$ , and  $N$  are:

$$\begin{aligned} F &= \frac{1}{2S_y^2} + \frac{1}{2S_z^2} - \frac{1}{2S_x^2} \\ G &= \frac{1}{2S_z^2} + \frac{1}{2S_x^2} - \frac{1}{2S_y^2} \\ H &= \frac{1}{2S_x^2} + \frac{1}{2S_y^2} - \frac{1}{2S_z^2} \\ L &= \frac{1}{2T_{yz}^2} \quad M = \frac{1}{2T_{xz}^2} \quad N = \frac{1}{2T_{xy}^2} \end{aligned} \quad (6.5)$$

Because compressive stresses are observed at the point of failure (see Table 6.1), compressive strengths from Table 2.1 are used for the values of  $S_x$ ,  $S_y$ , and  $S_z$  in equation (6.5).

The factors of safety  $F$  are shown in Figures 6.15 and 6.16. It is observed that the Tsai-Hill criterion under-predicts the experimental strength of the composite, as the values of  $F$  are all significantly less than unity. The Tsai-Hill criterion demonstrates almost no dependence on specimen geometry when compared with the maximum stress criterion (Figures 6.13 and 6.14). The inclusion of interaction terms appears to account for some of the differences arising from different stress behaviors.

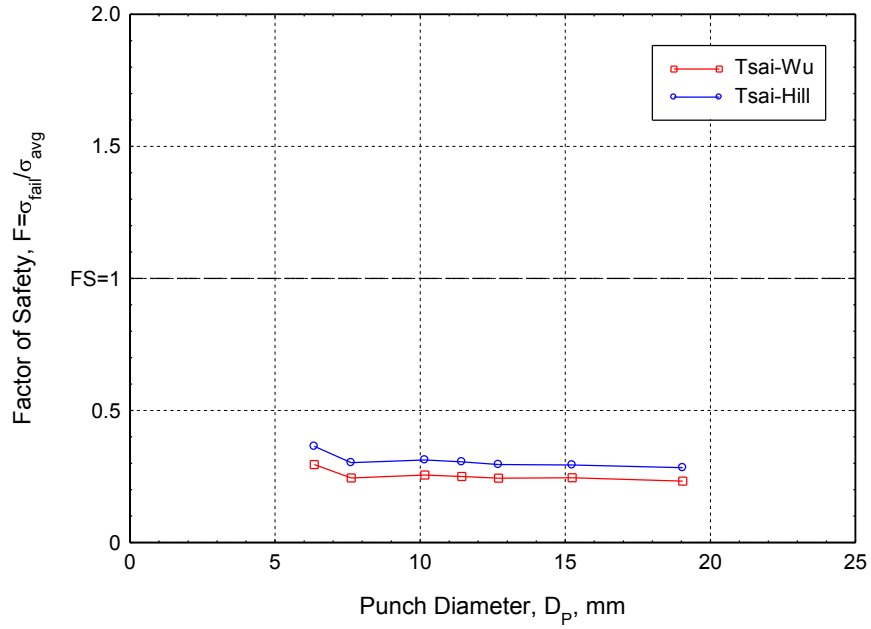


Figure 6.15 – Tsai-Hill and Tsai-Wu criteria as function of  $D_p$  (6.99-mm sample)

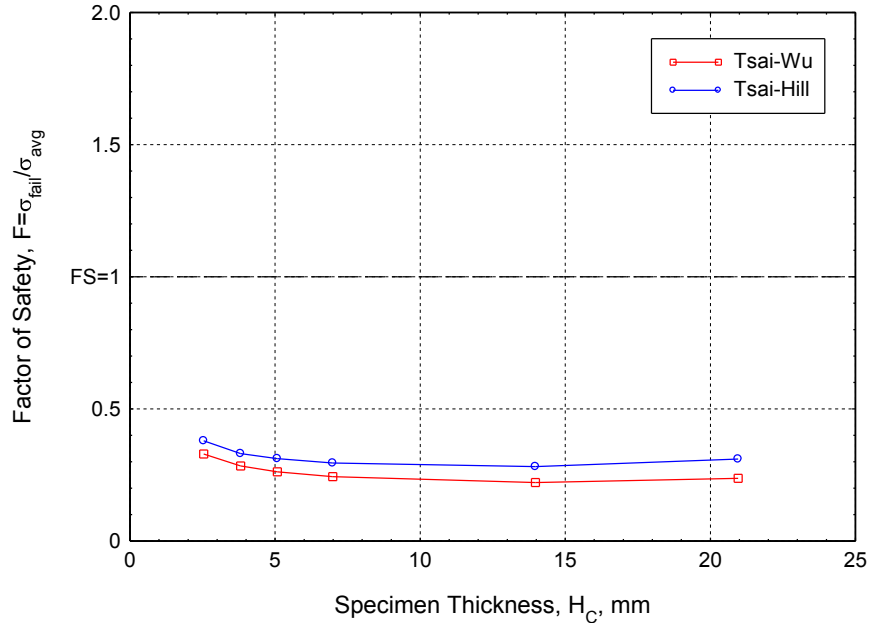


Figure 6.16 – Tsai-Hill and Tsai-Wu criteria as function of  $H_c$  (12.70-mm punch)

It is noted that while the normal stress components interact in equation (6.4), the shear stress components are still treated individually. The through-thickness radial shear component has been observed to be significant relative to its failure strength (Figures 6.13 and 6.14). Because of the lack of shear-normal stress interactions, the Tsai-Hill criterion is found to be ineffective for explaining the experimental behavior.

### 6.2.3 Tsai-Wu Criterion

A more thorough interactive criterion including all possible quadratic stress combinations was developed by Tsai and Wu (1971). It is expressed as:

$$\begin{aligned}
& F_x \sigma_x + F_y \sigma_y + F_z \sigma_z + F_{xy} \tau_{xy} + F_{xz} \tau_{xz} + F_{yz} \tau_{yz} \\
& + F_{x,x} \sigma_x^2 + 2F_{x,y} \sigma_x \tau_{xy} + 2F_{x,z} \sigma_x \tau_{xz} + 2F_{x,xy} \sigma_x \tau_{xy} + 2F_{x,xz} \sigma_x \tau_{xz} + 2F_{x,yz} \sigma_x \tau_{yz} \\
& + F_{y,y} \sigma_y^2 + 2F_{y,z} \sigma_y \tau_{yz} + 2F_{y,xy} \sigma_y \tau_{xy} + 2F_{y,xz} \sigma_y \tau_{xz} + 2F_{y,yz} \sigma_y \tau_{yz} \\
& + F_{z,z} \sigma_z^2 + 2F_{z,xy} \sigma_z \tau_{xy} + 2F_{z,xz} \sigma_z \tau_{xz} + 2F_{z,yz} \sigma_z \tau_{yz} \\
& + F_{xy,xy} \tau_{xy}^2 + 2F_{xy,xz} \tau_{xy} \tau_{xz} + 2F_{xy,yz} \tau_{xy} \tau_{yz} \\
& + F_{xz,xz} \tau_{xz}^2 + 2F_{xz,yz} \tau_{xz} \tau_{yz} \\
& + F_{yz,yz} \tau_{yz}^2 = f
\end{aligned} \tag{6.6}$$

where  $F_i$ ,  $F_{i,i}$ , and  $F_{i,j}$  are strength coefficients which are calculated as follows:

$$\begin{aligned}
F_i &= \frac{1}{S_i^T} - \frac{1}{S_i^C} \\
F_{i,i} &= \frac{1}{S_i^T S_i^C} \\
F_{i,j} &= -\frac{1}{2\sqrt{S_i^T S_i^C S_j^T S_j^C}}
\end{aligned} \tag{6.7}$$

The superscripts  $T$  and  $C$  represent tension and compression, respectively. For the shear components it is assumed that  $S_i^T = S_i^C$ . The expression for  $F_{i,j}$  is traditionally hard to derive; the expression in equation (6.7) was suggested by Vinson and Sierakowski (2002, p 314). The form of equation (6.6) requires that  $F_{i,i}F_{j,j} - F_{i,j}^2 \geq 0$  (Tsai & Wu, 1971, p 60), and it can be shown that the expressions in equation (6.7)

satisfy this requirement. It should be noted that the Tsai-Wu criterion is an improvement on the Tsai-Hill criterion (equations (6.4) and (6.5)), since it accounts for unequal tensile and compressive strengths and includes quadratic interactions between all normal and shear stress components.

The factors of safety calculated with the Tsai-Wu criterion are shown in Figures 6.15 and 6.16. It is seen that the values of  $F$  are again less than unity, predicting failure of the specimen below the experimentally observed applied stress value. They show very similar trends to the Tsai-Hill criterion (also shown in Figures 6.15 and 6.16). Capturing quadratic interactions between all stress components does not generate the behavior observed experimentally. The Tsai-Wu criterion is observed to under-predict the confined compressive strength of the experimental specimens by a greater margin than the Tsai-Hill criterion. While the stresses in the experimental specimen may be interacting to increase the strength of the material, the interactions in both the Tsai-Hill and Tsai-Wu criteria underestimate the apparent strength of the specimen. A failure criterion which accounts for strengthening due to stress interactions is needed.

#### **6.2.4 Hydrostatic Crush Criterion**

A hydrostatic failure criterion is used when all three normal stress components (i.e.  $\sigma_x$ ,  $\sigma_y$ , and  $\sigma_z$ ) are compressive, as seen in Table 6.1. The criterion predicts failure when the compressive stresses acting on an element of material crush the material in a brittle manner. The criterion used in the LS-DYNA MAT162 material model (Livermore Software Technology Corporation, 2007, pp 626-636) is considered here. This criterion is expressed as:

$$\frac{1/3(\sigma_1 + \sigma_2 + \sigma_3)}{S_{HS}} = f \quad (6.8)$$

where  $S_{HS}$  is the hydrostatic crush strength of the material, taken to have a value of 850 MPa (Xiao, Gama, & Gillespie, 2007, p 191).

The factors of safety for the hydrostatic failure criterion are presented in Figures 6.17 and 6.18 as a function of punch diameter and specimen thickness, respectively. The values of  $F$  are observed to be much closer to unity than the previous three criteria. This suggests that hydrostatic effects may be important for confined compression failure. Since a state of 3-D compression exists, this result is expected. However, while the values of  $F$  in Figure 6.17 are approximately constant and may suggest good agreement with the experimental results, Figure 6.18 suggests a strong dependency on specimen thickness. While the hydrostatic crush criterion accounts for the interactions of all three normal stress components in a manner consistent with the observed stress state within a confined compression specimen, it still does not capture strengthening due to geometric effects on the stress interactions.

### 6.2.5 Maximum Deviator Stress Criterion

If hydrostatic compression exists in a specimen, it is possible to redefine the normal stresses in terms of hydrostatic ( $HS$ ) and deviator ( $D$ ) stress components (Boresi & Schmidt, 2003, p 37):

$$\sigma_i = \tau^S + \tau^D = 1/3(\sigma_1 + \sigma_2 + \sigma_3) + \tau^D \quad (6.9)$$

This analysis is based on an assumption that an element of material compressed uniformly in all three directions will not fail in compression, regardless of the value of the hydrostatic stress applied. The amount of deviation ( $\sigma_i^D$ ) in each component from this uniform stress can then be considered as the stress leading to failure. Failure of

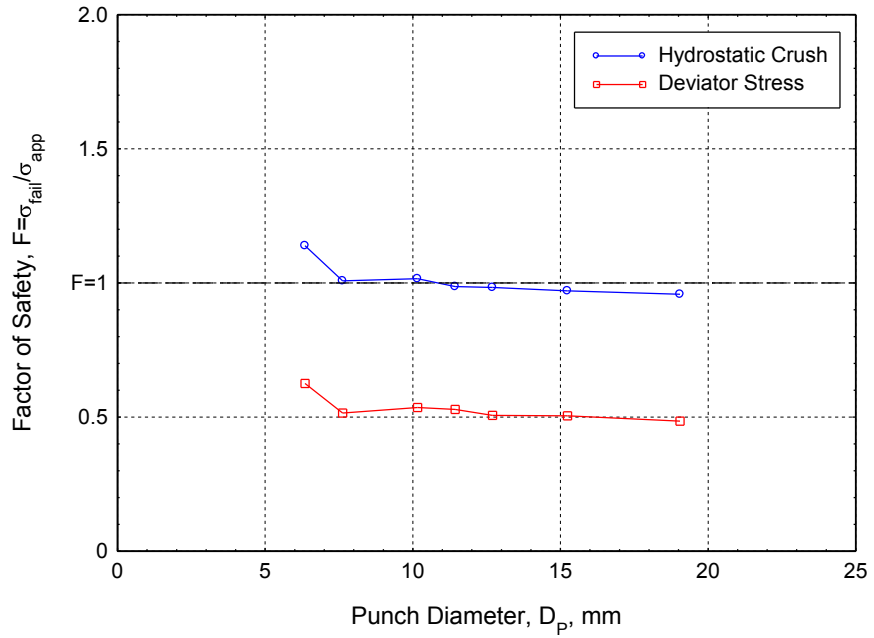


**Figure 6.17 – Crush and deviator criteria as a function of  $D_p$  (6.99-mm sample)**

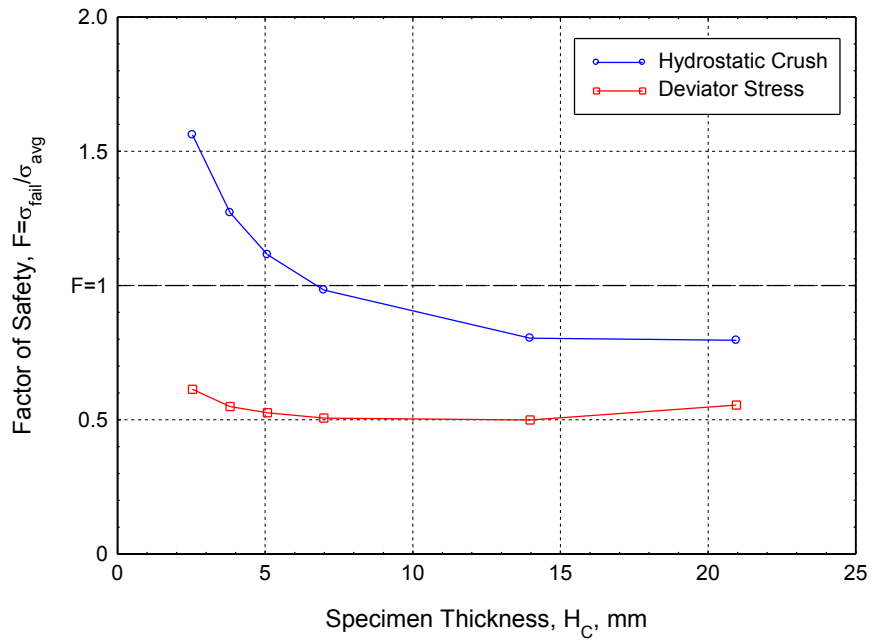


**Figure 6.18 – Crush and deviator criteria as a function of  $H_c$  (12.70-mm punch)**

this deviator stress can be evaluated using the maximum stress criterion given in equation (6.3):

$$\frac{\sigma - \frac{1}{3}(\sigma_1 + \sigma_2 + \sigma_3)}{S_i^C} = f \quad (6.10)$$

In equation (6.10)  $\sigma_i$  is taken to be  $\sigma_z$ , recalling from Figures 6.8 and 6.9 that the most significant normal stress component is the through-thickness stress. The factors of safety for the maximum deviator stress criterion in the through-thickness direction are given in Figures 6.17 and 6.18. It is observed that the values of  $F$  remain approximately constant as the specimen geometry varies. This suggests that the compressive hydrostatic stresses present in the confined compression specimen create the apparent increase in the strength of the specimen. However, the strength of the material is still under-predicted, with all the values of  $F$  being less than unity.

### 6.3 Mohr-Coulomb Criterion

In Chapter 3 it was observed that failure of the confined compression specimens occurred due to fracturing of the fibers and matrix at a characteristic angle. Using transformed stresses, it was determined that a compression-shear stress interaction acted along the fracture plane. The evaluation of the maximum deviator stress criterion in Section 6.2.5 also suggests that the compressive normal stresses within the specimens may be causing the apparent observed changes in material strength for different geometries.

Compression-shear interactions have traditionally been described using Mohr-Coulomb fracture theory. Mohr theorized that for such cases, the shear strength of the material along the fracture plane is a function of the normal stress on the fracture plane:

$$\tau = g(\sigma) \quad (6.11)$$

It should be noted that the terms  $\tau$  and  $\sigma$  in equation (6.11) represent the shear stress along the fracture plane and the stress normal to the fracture plane and are calculated with respect to the orientation of the fracture plane. Equation (6.11) is commonly written using a form originally proposed by Coulomb, which assumes that the function  $g$  is linear:

$$\tau = \mu\sigma + T \quad (6.12)$$

In equation (6.12)  $\mu$  is a friction coefficient and  $T$  is the unconfined shear strength of the material in the plane of fracture (Chatterjee, 1997, p 240). Xiao and Gillespie (2007, p 1299) developed a quadratic form of equation (6.11) to obtain better agreement with experimental data and account for the compressive strength of the material:

$$\tau = \mu \left( 1 - \left( \frac{\sigma}{S^C} \right)^a \right) \sigma + T \quad (6.13)$$

where  $a$  is a fitting parameter and  $S^C$  is the compressive strength of the material in the direction normal to the fracture plane. They also hypothesized that a compressive cut-off existed above which the material failed due to crushing instead of shear. Because of its simpler form, only equation (6.12) will be considered in the present study.

The Mohr-Coulomb failure envelope is defined using Mohr's circle to represent the state of stress at a point. The theory is illustrated schematically in Figure 6.19. The stresses in the material axes are plotted in normal-shear ( $\sigma$ - $\tau$ ) stress space as shown. It is noted that a shear component usually exists for stresses oriented in the material axes and must be accounted for when creating Mohr's circle. Once the angle of fracture ( $\theta$ ) is known, the stress components on the fracture plane can be found by

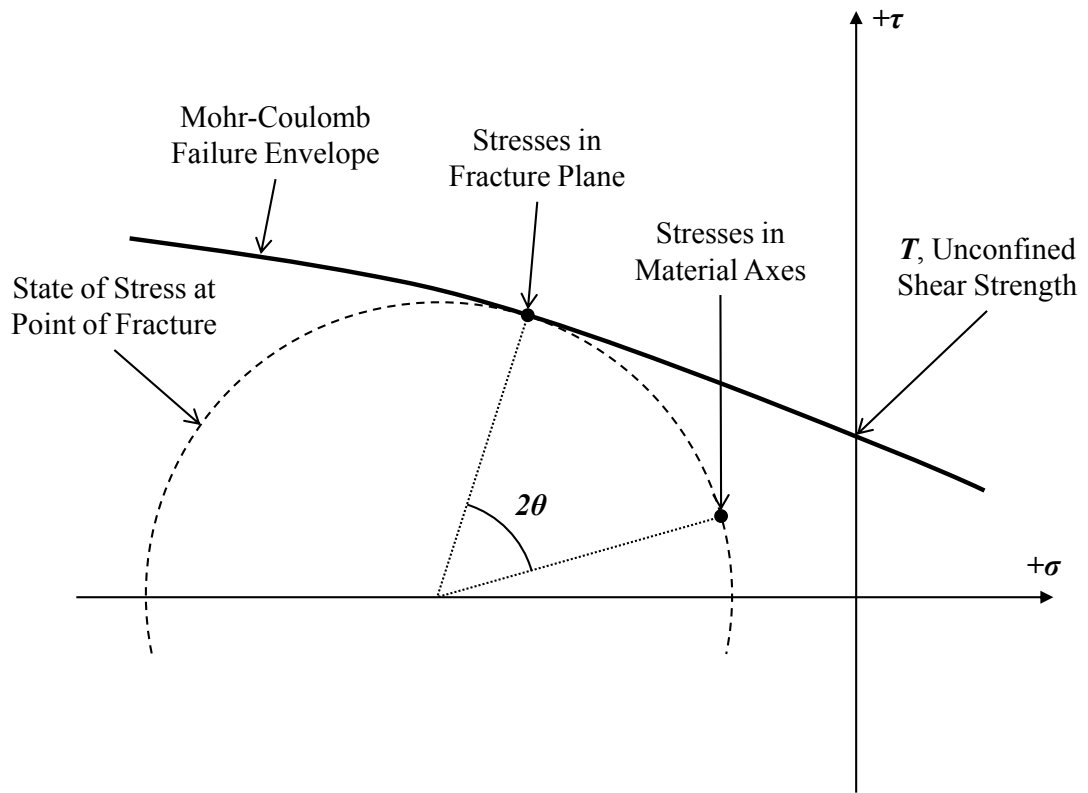


Figure 6.19 – Schematic of the development of a Mohr-Coulomb failure envelope

rotating an angle of  $2\theta$  counterclockwise from the stress components in the material axes. Because the fracture plane is expected to be the orientation of incipient failure, the Mohr-Coulomb envelope must pass through the point defining its stress components, but not pass through any other point; otherwise, failure would be expected in a different orientation. Thus, the Mohr-Coulomb envelope ideally is tangent to Mohr's circle at the point defining the stress components on the fracture plane (Chatterjee, 1997, p 240-242; Das, 2005, pp 205-209).

### 6.3.1 Calibrating the Mohr-Coulomb Envelope

It was noted in Section 6.1 that significant stress gradients on scales below the macroscopic level can confound proper usage of material strengths. Figures 6.20 and 6.21 show the transformed through-thickness shear and normal stress distributions, respectively. It is noted that stress gradients do exist. Using the methodology outlined in Section 6.1, these stress gradients were averaged over the thickness of the first ply and normalized to obtain stress components of the form  $\alpha = \sigma/\sigma_{app}$ . Because the parameters  $\mu$  and  $T$  in equation (6.12) are not known, the stresses on the fracture plane at the experimentally determined applied stress at failure ( $\sigma_{app} = 887$  MPa) were calculated, as discussed in Section 6.2.

These transformed shear stress data are shown as a function of the transformed normal stress in Figure 6.22. The values of  $\mu$  and  $T$  in equation (6.12) were calculated by performing a linear regression on the normal-shear data:

$$\tau_{\sigma'} = -.131\sigma_{\sigma'} + 589 \quad (6.14)$$

Because compression is assumed to be negative, the value of  $\mu$  is negative, unlike in equation (6.12). It is also noted that the value of  $T$  in equation (6.14) ( $T = 589$  MPa) is significantly larger than the value of unconfined shear strength calculated in Section

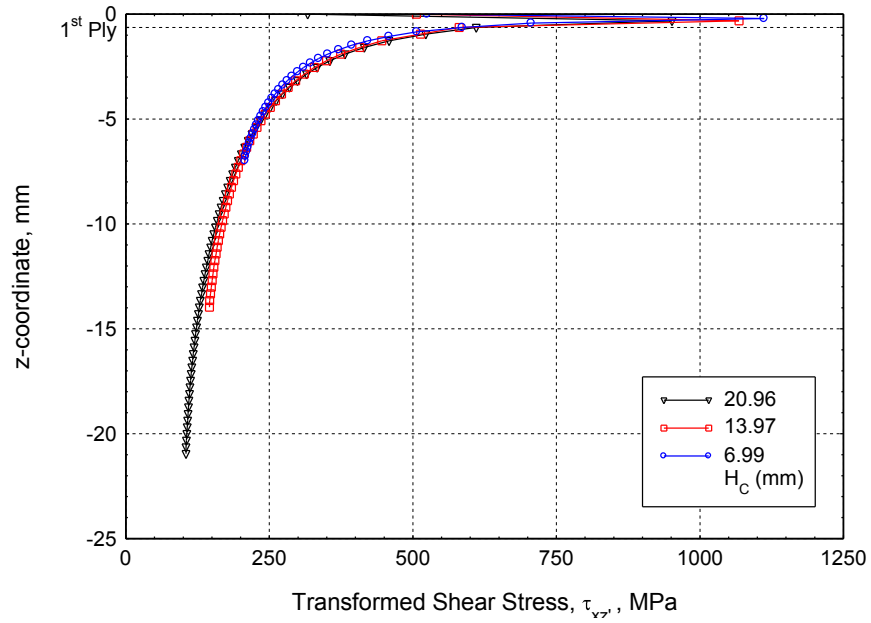


**Figure 6.20 – Transformed shear stress distribution (12.70-mm punch)**

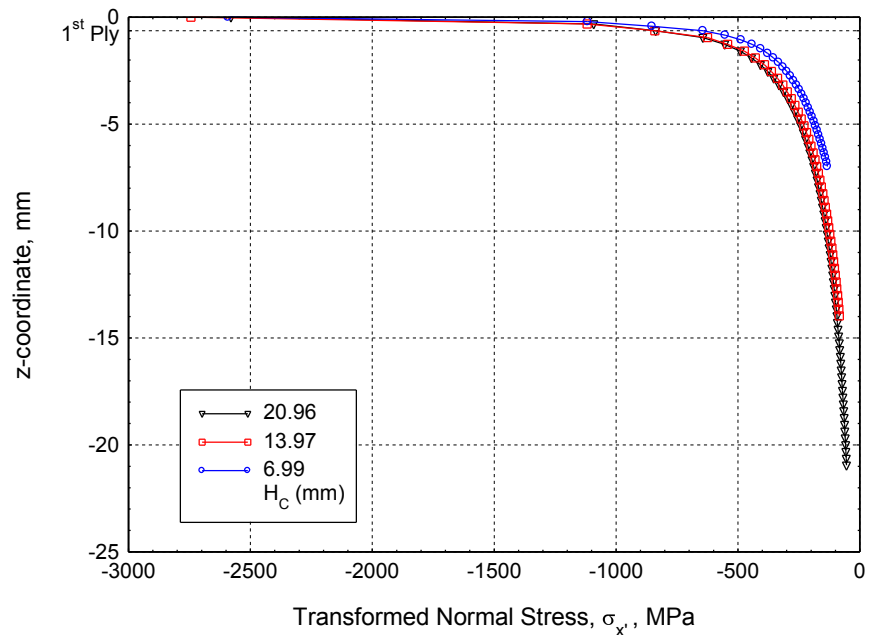


**Figure 6.21 – Transformed normal stress distribution (12.70-mm punch)**

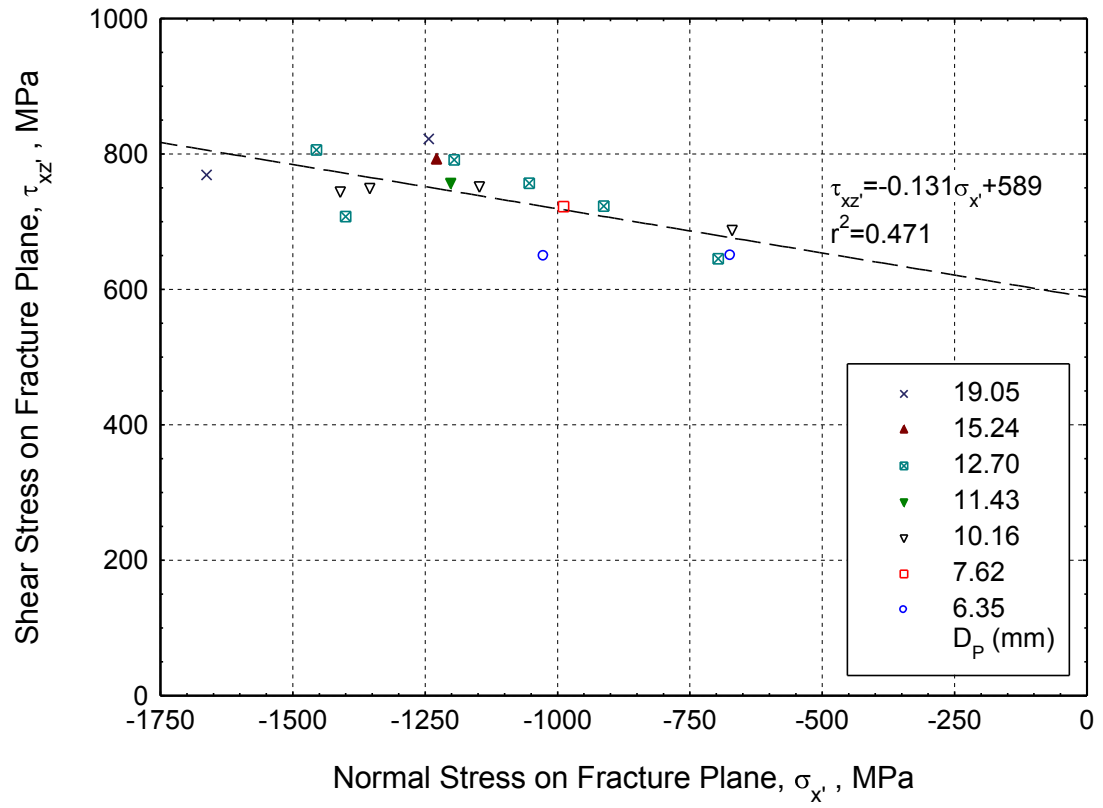


**Figure 6.22 – Calibration of the Mohr-Coulomb envelope**

6.1.1 ( $T = 270$  MPa). However, the strength calculated in Section 6.1.1 is for the material axes, and may not accurately represent the shear strength of the S-2/SC15 composite for diagonal fracturing of the fibers.

Equation (6.14) can be rewritten as a failure criterion for comparison with the other criteria presented in Section 6.2:

$$\frac{\tau_{z'}}{-0.131\sigma + 589} = f \quad (6.15)$$

The factors of safety  $F$  for the Mohr-Coulomb criterion are shown in Figures 6.23 and 6.24 as a function of punch diameter and specimen thickness, respectively. It is observed that almost all of the data points lie within the experimental standard deviation of unity. Figure 6.23 may appear to suggest that some trend exists with punch diameter, but recalling that the smallest punch diameter considered likely exhibits chamfering effects, the trend is less significant for the remaining data points. The data in Figure 6.24 also do not suggest a consistent trend with specimen thickness.

The Mohr-Coulomb criterion is observed to capture the apparent compressive strengthening behavior of confined compression specimens. It also accurately predicts the strength of the specimens. It should be noted that equations (6.14) and (6.15) were calibrated by assuming the experimentally measure average peak stress at failure ( $\sigma_{avg}$ ). Nonetheless, a Mohr-Coulomb form is able to accurately capture the expected stress interactions in a confined compression specimen. The maximum deviator stress criterion (Figures 6.17 and 6.18) also predicted constant failure behavior, though the magnitude of failure was inaccurate. Considering these two criteria together, it is concluded that a compressive strengthening interaction is responsible for the contradictory behavior of the experimental applied stress first noted in Section 3.2.

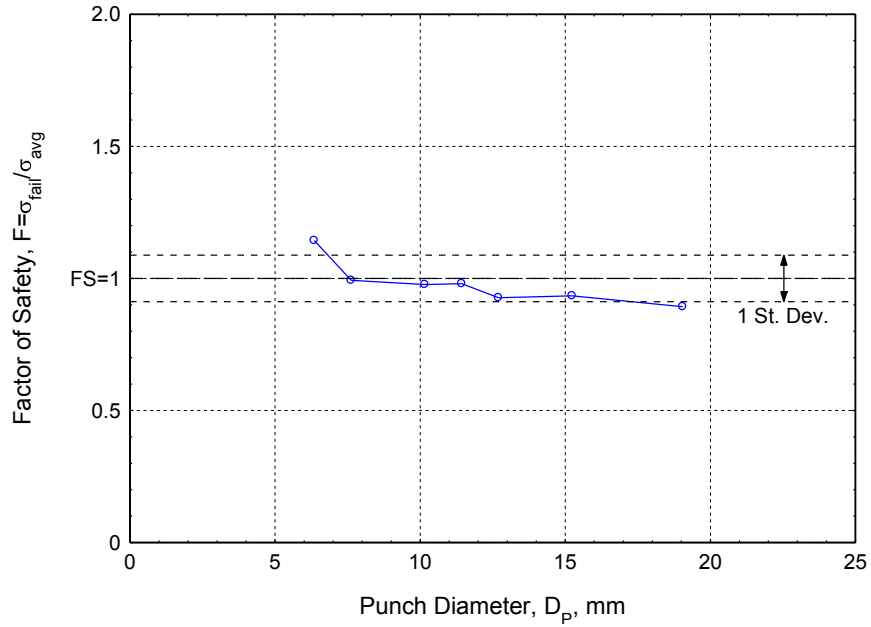


**Figure 6.23 – Mohr-Coulomb criterion as a function of  $D_P$  (6.99-mm sample)**

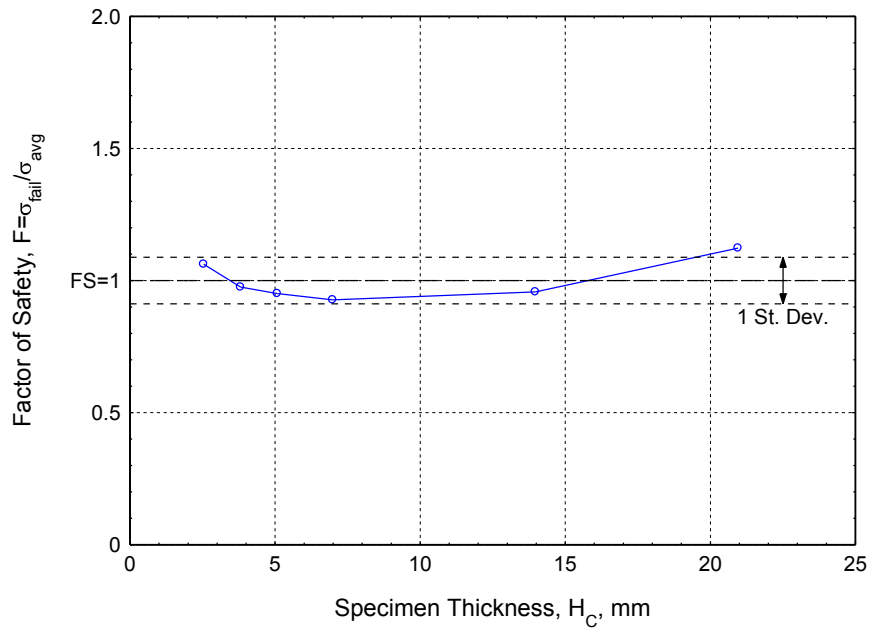


**Figure 6.24 – Mohr-Coulomb criterion as a function of  $H_C$  (12.70-mm punch)**

#### 6.4 Point of Failure Initiation

In Section 3.1 the question of determining the point of damage initiation was raised. The development of an appropriate failure criterion permits an analysis of initiation of damage at various locations on the specimen.

Knowing the stresses in the material axes from the finite element model (assuming  $\sigma_{app} = 887$  MPa), the radial and tangential components of those stresses with respect to the centerline of the punch can be determined. Assuming that the fracture plane is oriented at a constant angle around the punch periphery (see Section 3.1.1), the stresses on a hypothetical fracture plane at any radial and circumferential location can be found using the stress transformations in equations (3.8-3.10). By inputting the transformed stresses into equation (6.15) the proximity of each point to failure can be determined.

The results of this analysis are shown in Figures 6.25 and 6.26 for a thin and thick specimen, respectively. The values shown are the failure coefficients  $f$  for each point on the specimen. Thus values greater than unity are predicted to fail while values less than unity have not exceeded the failure criterion. Regions beyond the punch periphery are ignored since stresses in these regions are insignificant relative to the stress level required for failure. It is observed that failure initiates in the fiber direction ( $0^\circ/90^\circ$  orientation) at the punch periphery. However, the whole punch periphery is close to failure, and it is expected that the fracture propagates around the punch periphery in a brittle manner almost immediately after initiation. It is also noted that the center region of the thin specimen (Figure 6.25) is closer to failure than that of the thick specimen (Figure 6.26). This phenomenon may explain why multiple fractures were observed in thin experimental specimens, but not thick specimens. It is recalled from Figure 3.14 that the peak stresses on the fracture plane occur at the top

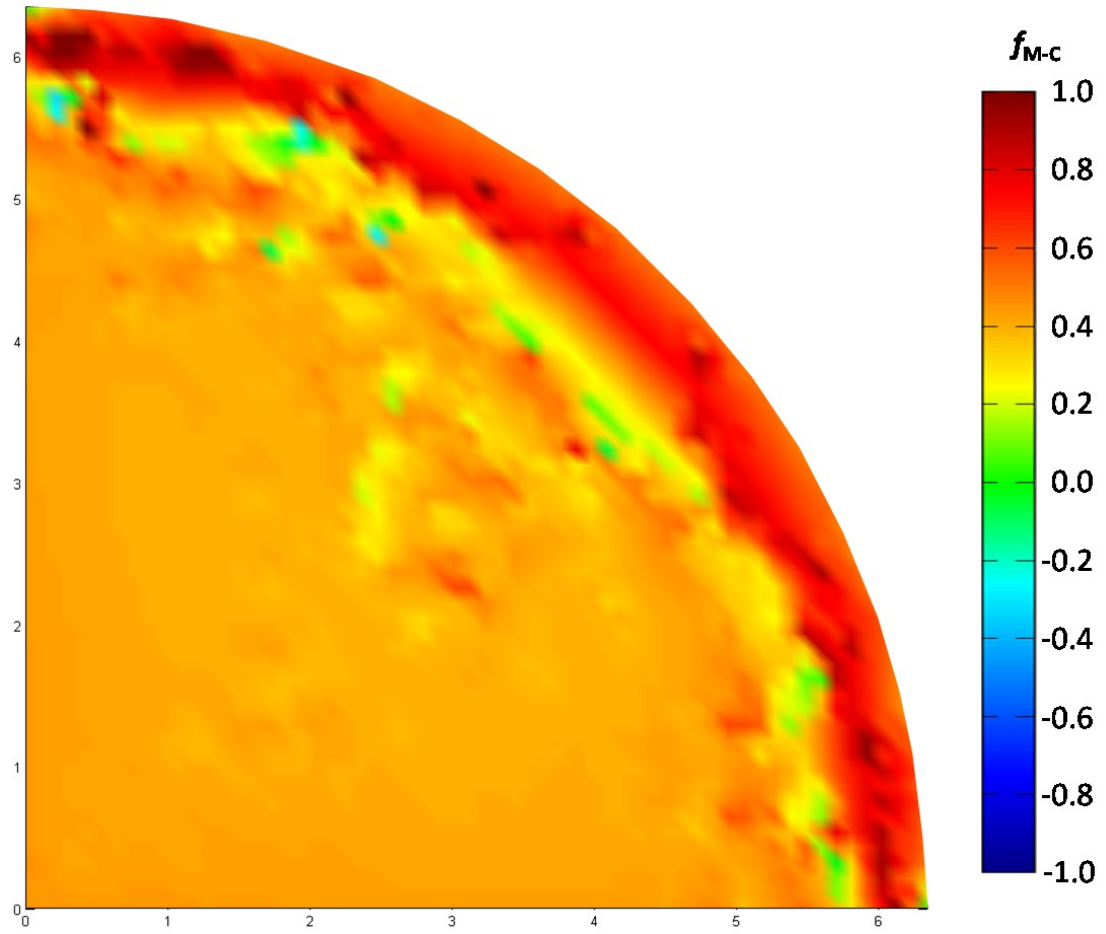


**Figure 6.25 – Damage propagation through a thin specimen (12.70-mm punch, 6.99-mm sample)**

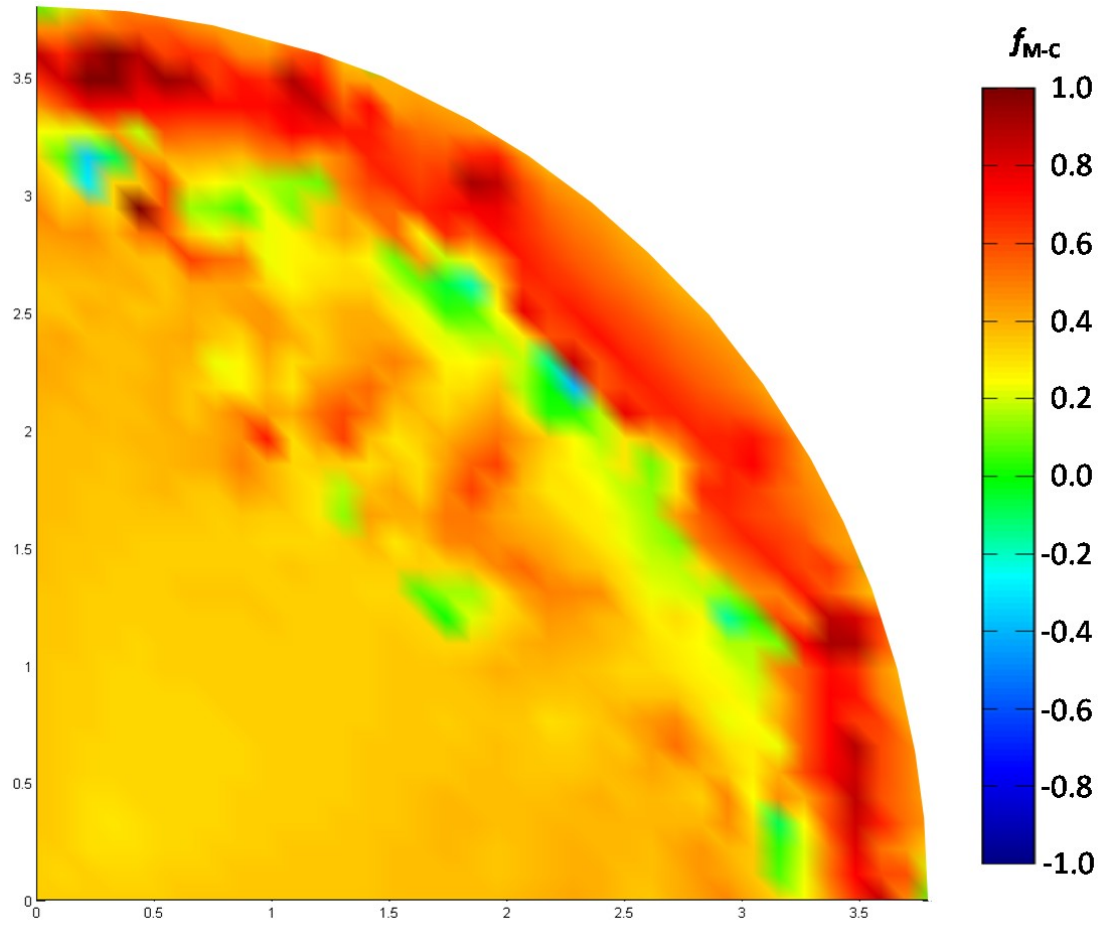


**Figure 6.26 – Damage propagation through a thick specimen (7.62-mm punch, 6.99-mm sample)**

of the specimen, suggesting failure initiates in the top ply and propagates through the thickness.

## **6.5 Scaling of the Applied Stress at Failure**

It was observed in Section 3.2 that the experimentally measured peak stress at damage initiation in confined compression specimens remains constant regardless of punch diameter or specimen thickness for the range of geometries considered. This suggested that the applied stress at damage initiation is a characteristic value of the S-2/SC15 composite material in confined compression. This result was initially viewed as contradictory when compared against the varying behavior of the internal stress distributions (Figure 6.1). However, it has been shown that a compression-shear stress interaction provides apparent specimen strengthening which generates the observed experimental behavior (Figures 6.23 and 6.24). With this conclusion, the applied stress at failure initiation can be found for any combination of specimen and punch.

However, it is important to determine the range of applicability of these results. The present study only considered a single material, an S-2/SC15 composite. While this result may be used to suggest similar behavior for other materials, especially materials that demonstrate a similar fracturing mode, such a scaling should not be assumed without additional verification. Likewise, only circular punches with significantly higher rigidity than the tested material were considered. Results cannot be applied to punches with different geometries or lower rigidities, which would cause significantly different stress distributions.

While a range of specimen and punch dimensions were tested (see Table 3.3), the range was not exhaustive. The conclusions presented may be valid as the

geometric ratio  $D_P/H_C \rightarrow 0$  (i.e. thick specimens and narrow punches), since the behavior of the stress distribution in such specimens is expected to be similar to the behavior observed in the present study. However, as  $D_P/H_C \rightarrow \infty$  (i.e. thin specimens and wide punches), the stress state exhibits a more uniform state of compression (see Figures 3.11 and 6.1). While hydrostatic stresses were observed in the specimens in the present study (see Section 6.2.4), there is a reasonable expectation that geometries exist for which the compressive stresses have a greater effect than the shear stresses. Xiao and Gillespie hypothesized that such an effect would occur and introduced a compressive failure cut-off in their interlaminar Mohr-Coulomb envelopes (2007). The development of such a cut-off is beyond the scope of the present study, which is focused on “thick-sectioned” composites (e.g.  $D_P/H_C < 1$ ). Therefore, the present results should only be considered safely applicable within the range tested (i.e.  $0 < D_P/H_C < 5$ ) and for the material used in testing and modeling.

## 6.6 Chapter Summary

Having examined the fracture mode and applied stress at failure of the confined compression specimens, developed a criterion for specimen sizing, and extracted a geometric similarity parameter, the present chapter sought a scaling expression for the applied stress at failure by considering the contradictory behavior of the experimental applied stress at failure (Section 3.2). The behavior of the internal stress distribution was investigated, showing stress concentrations at the punch periphery for thicker specimens but a uniform compressive stress for thinner specimens. To explain how different stress states could generate the same applied stress for failure, five common failure criteria were considered: maximum stress, Tsai-Hill, Tsai-Wu, hydrostatic crush, and maximum deviator stress. The deficiencies of

each criterion were presented, suggesting the need for a criterion which captured the apparent strengthening of the material due to compressive stress interactions.

Recalling the compression-shear stress interaction observed on the fracture plane in Chapter 3, a Mohr-Coulomb failure criterion was proposed and calibrated. This criterion accurately predicted failure within the experimental variability. It was concluded that the compression-shear interaction explained the existence of a characteristic applied stress at failure despite internal changes in the stress behavior.

## Chapter 7

### CONCLUSIONS

#### 7.1 Summary

The present study has examined the development of scaling parameters for a confined compression test. The key measure of the confined compression test is the applied stress at damage initiation, which is used as a measure of the crush strength of the material under ballistic penetration. While complete characterization of the crush strength necessitates experiments for a range of specimen thicknesses and punch diameters, a scaling parameter would negate the need for more than a few tests over a range of dimensions.

Only S-2 glass/SC15 epoxy composites were considered in the present study. The failure mode for this material was determined to be diagonal fracturing through the fiber and matrix within the punch periphery, creating an approximate “cone” of damaged material. The fracture angle ( $\theta$ ) was found to be constant regardless of specimen thickness. However, two regimes of specimen thickness were noted with potentially different behaviors: “thin” specimens in which fractures propagated through the entire specimen thickness and “thick” specimens in which fractures were wholly contained within the specimen. The applied stress at failure ( $\sigma_{app}$ ) was also found to be constant regardless of specimen geometry. However, an analysis of the force reactions in the specimen showed that the internal behavior is dominated by compression for thin specimens, but by shear for thick specimens. This

contradiction raised a central question of the present study: how does a stress distribution which varies with specimen geometry lead to failure initiation at a characteristic applied stress? A transformation of stresses into the fracture plane using a finite element model showed that a compression-shear stress interaction occurred along the fracture plane. It was noted that this observation may be a possible explanation for the behavior of the applied stress at failure.

It was recognized that the width of the specimen could have a significant effect on the stress distribution in the specimen. To ensure consistency in the generated results and provide a range of applicability for the scaling law, the minimum specimen width to ensure consistent behavior,  $L_{crit}$ , was calculated by finding the width of the stress distribution normal to the specimen support. This width was found to be a function of both the punch diameter and specimen thickness, and an empirical expression for the S-2/SC15 composite material was derived from an analytical form of the confined compression problem and validated with the numerical model of the experimental setup.

Having determined boundaries for specimen geometry, the analytical form was examined for scaling parameters. It was observed that all three stress components could be normalized by the applied stress. Knowing that the specimen stress distributions were constant for all  $L_C > L_{crit}$ , expressions of  $D_p/L_C$  and  $H_C/L_C$  in the analytical form were simplified to yield a single geometric parameter:  $D_p/H_C$ . Numerical modeling demonstrated consistent stress distributions when the ratio  $D_p/H_C$  was equal for two different specimens. However, the use of a punch chamfer was found to prevent accurate scaling of results unless the chamfer is insignificant relative

to the punch diameter. The development of a geometric scaling allowed for extrapolation of results between geometrically similar punch-specimen pairs.

The behavior of the applied stress at failure was considered again by first examining the behavior of the internal stress distribution. It was observed that stresses are concentrated at the punch periphery for thicker specimens but become more uniform for thinner specimens, as suggested by the internal force balance. Five common composite failure criteria were evaluated to capture the observed behavior of confined compression specimens: the maximum stress, Tsai-Hill, Tsai-Wu, hydrostatic crush, and maximum deviator stress criteria. While none of the criteria accurately captured the experimental behavior, their deficiencies suggested that a compressive stress interaction was important to the behavior. Recalling the compression-shear fracture behavior of the samples, a Mohr-Coulomb type failure was proposed as a potential failure criterion. Numerical calibration of the Mohr-Coulomb envelope produced a failure criterion that showed good agreement with the experimental results. The Mohr-Coulomb criterion suggested that fracture of the S-2/SC15 material under confined compression initiates in the upper ply at the punch periphery in the fiber directions.

It is concluded that two scaling laws exist for confined compression testing of S-2/SC15 composites. First, specimens that have equivalent values of the ratio  $D_p/H_C$  have equivalent stress distributions in scaled geometric space. Second, the applied stress at failure has a characteristic value regardless of specimen geometry.

However, there are limitations on the application of these results. Experimental and theoretical specimens should be larger than a circle with a diameter of  $L_{crit}$ . Experimental and numerical models only considered the range  $0 < D_p/H_C < 5$ .

Results should only be considered valid in this range, since the failure mode may change outside this range, especially for  $D_P/H_C \gg 5$ . Numerical and analytical modeling assumed that the composite was a monolithic material, neglecting any interactions on a scale smaller than the ply level. Comparisons using  $D_P/H_C$  may not be valid for extremely thin specimens, where interactions below the ply level could become important.

## 7.2 Directions for Future Work

Additional study is possible on the mechanics of the confined compression failure. The nature of the stress concentrations at the punch periphery (see Figures 6.2-6.7) is not well understood. For the present study, the through-thickness stress gradients were averaged using a single ply thickness as the characteristic depth. However, this method has limitations when geometric scaling is used to compare similar  $D_P/H_C$  ratios as discussed in Section 6.1. A more detailed analysis of the fracture mechanics was beyond the scope of the present study, but could be a direction for future research. The present study also considered only linear-elastic behavior. A future numerical study of the propagation of damage using a finite element code with failure analysis could validate the fracture behavior postulated in Section 6.4.

Determining the strength of a material under confined compression is only one phase of the Quasi-Static Penetration Method (Gama & Gillespie, 2008). Material behavior is also studied for specimens without full support over a range of support diameters. It remains to be determined what scaling laws and damage regimes exist for these specimens. The present work provides a systematic methodology for establishing scaling parameters and limits of application. However, testing specimens

without a full support introduces additional difficulties not encountered when considering the confined compression case.

A third geometric parameter must be considered: the support span diameter,  $D_s$ . Scaling from experimental results requires the development of a test matrix from which two parameters can be held constant while the remaining parameter varies. The range of experiments must be sufficiently large to accurately develop scaling parameters.

While the failure mode was essentially consistent for all the confined compression specimens considered, this is not the case when the support span is allowed to vary. In cases where the support diameter is similar to the punch diameter, a shear dominated failure would be expected. In cases where the support diameter is much larger than some function of the punch diameter and specimen thickness, a bending dominated failure would be expected. For intermediary cases a mixed bending-shear failure would be expected. Each failure mode will likely have a different scaling behavior. Additionally, expressions must be developed for the boundaries between the different modes.

There is also a potential for different damage regimes within a single load-displacement curve. While only the peak stress value at the end of the linear-elastic regime is important in confined compression testing, the complete load-displacement curve is used in the QS-PM analysis for specimens without full support. A representative curve is shown in Figure 7.1. Sectioning of specimens at different displacement levels suggests that the specimen undergoes a number of damage phases during penetration, which are illustrated in Figure 7.1. It may be necessary to partition the load-displacement curve based on these damage phases and then develop

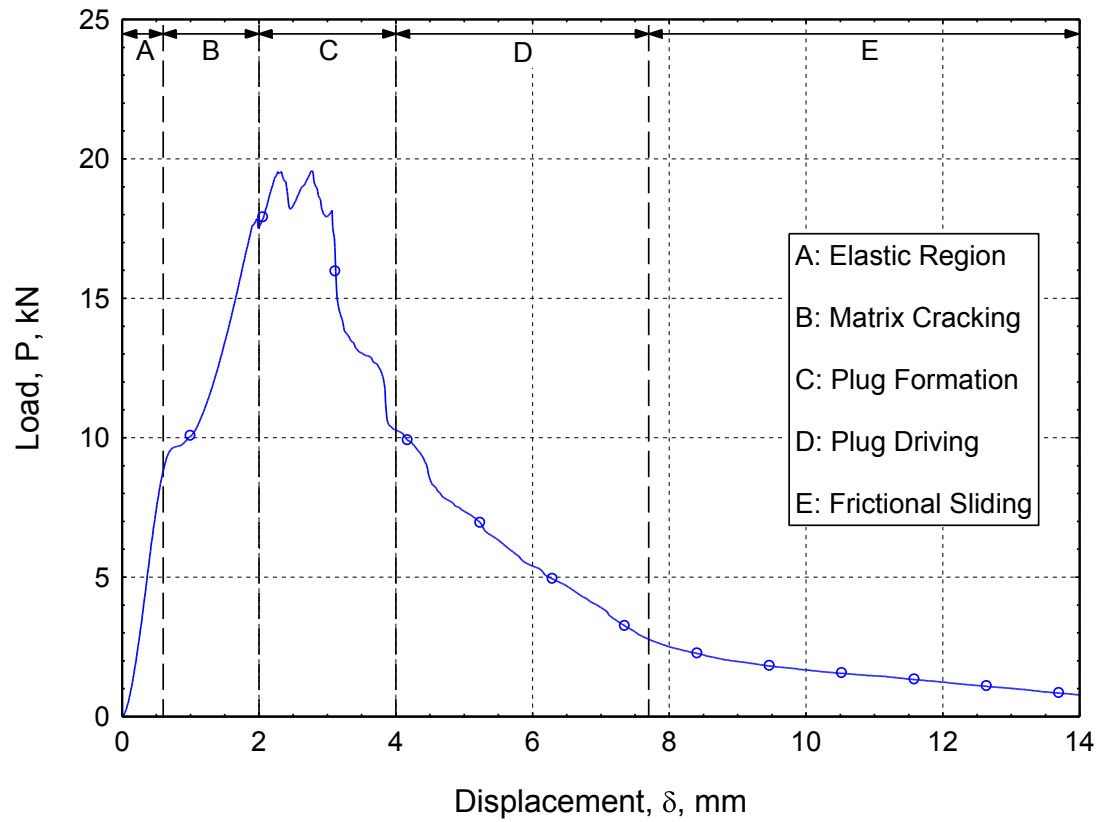


**Figure 7.1 – Representative load-displacement curve for a specimen without full support (7.62-mm punch, 7.11-mm sample, 15.24-mm span)**

parametric scaling laws for each portion of the curve. Approximating each partition with a basic mathematical form could permit comparison of data for development of scaling parameters from experimental results.

It is apparent that a final scaling law for the QS-PM will be significantly more complicated than the relationships derived in the present study for the confined compression test. However, a similar methodology can be employed. The experimental damage modes must be determined to identify regimes with the potential for unique scaling laws. Analytical solutions for plate-bending problems could be applied to identify potential scaling parameters. Numerical modeling would both validate the analytical forms and provide insights into the stresses within experimental specimens. Geometric limitations would also need to be established: a similar critical width phenomenon likely exists for specimens that aren't fully supported and would be a function of the support diameter as well as the punch diameter and specimen thickness. Comparing predictions from well-established failure criteria with the experimental results could suggest scalings for the applied stress. An additional set of parametric expressions for specimens without full support would permit further interpolation of results and exploration of the mechanics of the QS-PM.

## REFERENCES

- Abrate, S. (1991). Impact on laminated composite materials. *Applied Mechanics Review*, 44, 155-190.
- Abrate, S. (1994). Impact on laminated composites: Recent advances. *Applied Mechanics Review*, 47, 517-544.
- ASTM International. (2003). *D 2734: Standard test methods for void content of reinforced plastics*. West Conshohocken, PA: ASTM International.
- ASTM International. (2004). *D 6264: Standard test method for measuring damage resistance of fiber-reinforced polymer-matrix composite to concentrated quasi-static indentation force*. West Conshohocken, PA: ASTM International.
- Bartus, S.D. & Vaidya, U.K. (2007). A review: Impact damage of composite materials. *Journal of Advanced Materials*, 39(3), 3-21.
- Baucom, J.N. & Zikry, M.A. (2003). Evolution of failure mechanisms in 2D and 3D woven composite systems under quasi-static perforation. *Journal of Composite Materials*, 37, 1651-1674.
- Bless, S.J., Hartman, D.R., Okajima, K., & Hanchak, S.J. (1989). Ballistic penetration of S-2 glass laminates. Proceedings from the 21st International SAMPE Technical Conference.
- Boresi, A.P. & Schmidt, R.J. (2003). *Advanced mechanics of materials* (6<sup>th</sup> ed.). Hoboken, NJ: John Wiley & Sons, Inc.
- Caprino, G., Langella, A., & Lopresto, V. (2003). Indentation and penetration of carbon fiber reinforced plastic laminates. *Composites: Part B*, 34, 319-325.
- Chatterjee, S.N. (1997). A Coulomb-Mohr type criterion for matrix mode failure in lamina. In S.J. Hooper (Ed.), *Composite Materials: Testing and Design, 13<sup>th</sup> Volume, ASTM STP 1242* (pp 237-256). West Conshohocken, PA: American Society for Testing and Materials.

- Collings, T.A. (1974). Transverse compressive behavior of unidirectional carbon fiber reinforced plastics. *Composites*, 5, 108-116.
- Das, B.M. (2005). *Fundamentals of Geotechnical Engineering* (2<sup>nd</sup> ed.). Toronto, Ontario: Nelson.
- Gama, B.A., Binkley, A.W., Lim, A.S., & Gillespie Jr., J.W. (2006). A new experimental technique to characterize the fiber crush and fiber shear behavior of composites at quasi-static and high rates of strain. [Internal unpublished paper].
- Gama, B.A. & Gillespie Jr., J.W. (2008). Punch shear based penetration model of ballistic impact of thick-section composites. *Composite Structures*, 86, 356-369.
- Gellert, E.P., Cimpoeru, S.J., & Woodward, R.L. (2000). A study of the effect of target thickness on the ballistic perforation of glass-fiber-reinforced plastic composites. *International Journal of Impact Engineering*, 24, 445-456.
- Hibbeler, R.C. (2005). *Mechanics of materials* (6<sup>th</sup> ed.). Upper Saddle River, NJ: Pearson Prentice Hall.
- Hill, R. (1948). A theory of the yielding and plastic flow of anisotropic metals. *Proceedings of the Royal Society of London: Series A, Mathematical and Physical Sciences*, 193(1033), 281-297.
- Lee, S.W.R. & Sun, C.T. (1993). Dynamic penetration of graphite/epoxy laminates impacted by a blunt-ended projectile. *Composites Science and Technology*, 49, 369-380.
- Livermore Software Technology Corporation. (2007). *LS-DYNA keyword user's manual: Version 971* (Vol. 2). Livermore, CA: Livermore Software Technology Corporation
- Manzella, A.F., Gama, B.A., & Gillespie Jr., J.W. (2009). Penetration resistance of thick-section composites: Effect of projectile diameter and mass. *Proceedings from the 1<sup>st</sup> Joint ASC/CACSMMA Conference*.
- Milovic, D. (1992). *Stresses and displacements for shallow foundations*. New York, NY: Elsevier.
- Naik, N.K. & Doshi, A.V. (2008). Ballistic impact behavior of thick composites: parametric studies. *Composite Structures*, 82, 447-464.

- Naik, N.K., Shirao, P., & Reddy, B.C.K. (2005). Ballistic impact behavior of woven fabric composites: Parametric studies. *Materials Science and Engineering A*, 412, 104-116.
- Nemes, J.A., Eskandari, H., & Rakitch, L. (1998). Effect of laminate parameters on penetration of graphite/epoxy composites. *International Journal of Impact Engineering*, 21(1-2), 97-112.
- Oguni, K., Tan, C.Y., & Ravichandran, G. (2000). Failure mode transition in unidirectional E-glass/vinylester composite under multiaxial compression. *Journal of Composite Materials*, 34, 2081-2097.
- Potter D., Gupta V., Chen X., & Tian J. (2005). Mechanisms-based failure laws for AS4/3502 graphite/epoxy laminates under in-plane biaxial compression. *Composites Science and Technology*, 65, 2105-2117.
- Rosen, B.W. (1965). Mechanics of composite strengthening. In *Fiber Composite Materials* (pp. 37-75). Metals Park, OH: American Society for Metals.
- Sun, C.T. & Potti, S.V. (1996). A simple model to predict residual velocities of thick composite laminates subjected to high velocity impact. *International Journal of Impact Engineering*, 18(3), 339-353.
- Swanson, S.R. (1993). Scaling of impact damage in fiber composites from laboratory specimens to structures. *Composite Structures*, 25, 249-255.
- Tsai, S.W. & Wu, E.M. (1971). A general theory of strength for anisotropic materials. *Journal of Composite Materials*, 5, 58-80.
- Vinson, J.R. & Sierakowski, R.L. (2002). *The behavior of structures composed of composite materials* (2<sup>nd</sup> ed.). Boston, MA: Kluwer Academic Publishers.
- White, F.M. (2003). *Fluid mechanics* (5<sup>th</sup> ed.). New York, NY: Mc Graw-Hill.
- Whitney, J.M. & Nuismer, R.J. (1974). Stress fracture criteria for laminated composite containing stress concentrations. *Journal of Composite Materials*, 8, 253-265.
- Wood, D.M. (1984). Circular load on elastic layer. *International Journal for Numerical and Analytical Methods in Geomechanics*, 8, 503-509.
- Woodward, R.L., Egglestone, G.T., Baxter, B.J., & Challis, K. (1994). Resistance to penetration and compression of fiber-reinforced composite materials. *Composites Engineering*, 4(3), 329-341.

- Xiao, J.R., Gama, B.A., & Gillespie Jr., J.W. (2007). Progressive damage and delamination in plain weave S-2 glass/SC-15 composites under quasi-static punch-shear loading. *Composite Structures*, 78, 182-196.
- Xiao, J.R. & Gillespie Jr., J.W. (2007). Failure criterion for composite laminates under interlaminar shear and compression. *Journal of Composite Materials*, 41, 1295-1309.
- Yen, C.F., Cheeseman, B.A., Hoppel, C.P.R., Gama, B.A., & Gillespie Jr., J.W. (2005). Modeling of the compressive failure of plain weave composites. Proceedings from the *ASC/ASTM-D30 Joint 19<sup>th</sup> Annual Technical Conference*.
- Zhou, G., Lloyd, J.C., & McGuirk, J.J. (2001). Experimental evaluation of geometric factors affecting damage mechanisms in carbon/epoxy plates. *Composites: Part A*, 32, 71-84.